

A High Resolution Capacitance-Based Lateral Position Microsensor

by

Douglas Edward Adams

B.S. in Mechanical Engineering
University of Cincinnati, 1994

Submitted to the Department of Mechanical Engineering
in partial fulfillment of the requirements for the degree of

Master of Science in Mechanical Engineering


at the

MASSACHUSETTS INSTITUTE OF TECHNOLOGY

February 1997

© Massachusetts Institute of Technology 1997. All rights reserved.

Author
Department of Mechanical Engineering
January 17, 1997

Certified by. 
Kamal Youcef-Toumi
Associate Professor
Thesis Supervisor

Accepted by
Ain A. Sonin
Chairman, Department Committee on Graduate Students

MASSACHUSETTS INSTITUTE
OF TECHNOLOGY

APR 16 1997

ENG

A High Resolution Capacitance-Based Lateral Position Microsensor

by

Douglas Edward Adams

Submitted to the Department of Mechanical Engineering
on January 17, 1997, in partial fulfillment of the
requirements for the degree of
Master of Science in Mechanical Engineering

Abstract

A high resolution, capacitance-based, one-dimensional, lateral position microsensor (HCLPM) has been conceptualized, designed, and fabricated. Although the notion of a capacitance-based lateral position sensor is not new, the HCLPM was configured to enhance the resolution and accuracy of the position measurement. Innovative ideas in the sensor design include a partial contact configuration, encapsulating shielding arrangement, and a fully differential and direction sensitive design. The goal of the project is to attain a sensing resolution of $10nm$ over a long range. After studying the existing sensor designs, the theory of electrostatics was used to design and analyze the HCLPM. The technologies of microfabrication were leveraged to build the high resolution, high precision sensor structure. Tests to verify sensor performance are currently being devised and will be carried out in the experimental phase of this research.

Thesis Supervisor: Kamal Youcef-Toumi
Title: Associate Professor

Acknowledgments

I would like to thank Professor Youcef-Toumi for his patience, contributions, and enthusiasm over the past two years. His energy level has inspired me to continue to work hard, and my fascination for engineering has grown stronger because of him. I also thank the Daewoo Corporation for their generous support of this research during the past two years. My appreciation also goes out to the administrative and technical staff at the Microsystems Technology Laboratory at MIT. Without the help of Joe Walsh, Paul Tierney, Pat Burkhart, Kurt Broderick and Vicki Diadiuk, this research would not have been possible. Also, I thank the Massachusetts Institute of Technology for allowing me to attend school here. Thank you for letting me participate in a truly exceptional learning experience during the last three years.

Finally, I thank my mother and father, who have supported me in every way possible. They have sacrificed a lot to give me everything I ever needed or wanted. Their most important contribution has been their constant love and understanding. Mom and dad, thank you for everything. I dedicate this thesis to you.

To my parents:

How could a blade of grass

Repay the warmth from the spring sun?

(Meng Chio 751-814)

Contents

1	Introduction	15
1.1	Summary of concepts for capacitance-based position sensors	16
1.1.1	Vertical or proximity sensors	16
1.1.2	Lateral position sensors	17
1.1.3	Summary of the existing designs	19
1.1.4	Limitations and benefits of existing designs	22
1.1.5	Innovative aspects of the improved design	27
1.2	Motivations for a lateral position microsensor	29
1.2.1	High density memory storage	30
1.2.2	Microelectromechanical devices and related applications	31
1.3	General overview of thesis	32
2	Theory	33
2.1	Mutual capacitance - a theoretical framework	33
2.2	Simplifying assumptions and intermediate calculations	35
2.2.1	Low frequencies and small structures	35
2.2.2	Selecting a dielectric medium	36
2.2.3	Properties of the electrode material	37
2.2.4	Electric field distribution near structural edges	39
2.2.5	Idealized system dimensions	41
2.3	Calculation of mutual capacitance	42
2.3.1	Example using the parallel-plate assumptions	42
2.3.2	Example of a more accurate capacitance calculation	44

2.3.3	Extending the spatial solution domain	48
2.3.4	Effects of finite width dimension	50
2.3.5	Dependence of capacitance on geometry	51
2.4	Variations in the ideal static capacitance calculation	52
2.4.1	The sensing problem for moving electrodes	53
2.4.2	Sensitivity to vertical motions	54
2.4.3	Sensitivity to tilting motions	55
2.4.4	Sensitivity to changes in lateral position	57
2.4.5	Linear output for lateral changes in position	61
2.4.6	Dielectric Media	62
2.4.7	Environmental drift	64
2.4.8	Differential compensation and modal "noise"	70
2.5	Summary of the theory	71
3	Design	73
3.1	Objectives of the sensor design	73
3.2	Design strategy	75
3.2.1	Selecting the operating gap	76
3.2.2	Design sensitivity	77
3.2.3	Electrode configuration - periodicity	77
3.2.4	Electrode configuration - structure	80
3.2.5	Electrode configuration - phasing	83
3.2.6	Electrode and interconnect spacing	84
3.2.7	Electrode pattern	86
3.3	Hybrid sensor design	91
3.3.1	Minimizing stray and parasitic capacitances	91
3.3.2	The hybrid interface	94
3.3.3	Stray immune measurements	95
3.3.4	Circuit for capacitance measurement	96
3.4	Summary of the design	97

4	Fabrication	100
4.1	Selecting a fabrication method	100
4.1.1	Cleaning operations	101
4.1.2	Lithographic technique	102
4.1.3	Photomask generation and pattern yield	102
4.1.4	Photoresist technology and the illumination source	103
4.1.5	Practical resolution limits	105
4.1.6	Electron beam deposition	107
4.1.7	Baking operations	108
4.1.8	Wet and dry etching operations	109
4.1.9	Inspection procedures	111
4.1.10	Cost limitations on the process	112
4.2	Overview of the fabrication process	112
4.2.1	Step 1: Mask generation and PFR preparation	113
4.2.2	Step 2: Glass pattern	117
4.2.3	Step 3: Aluminum pattern	123
4.2.4	Step 4: Silicon dioxide pattern	127
4.3	Summary of fabrication	129
5	Conclusions and Recommendations	133
A	Matlab scripts	135
A.1	rectube.m	135
A.2	numlap.m	137
A.3	tiltsol.m	139
A.4	allsens.m	140
B	PFR code	142
B.1	cap-sense.fl	142
B.1.1	more-bindings.fl	143
B.1.2	pyretch.fl	144

B.1.3	more-utils.fl	145
B.1.4	dea_masks.fl	149
B.1.5	ebeamal.fl	149
B.1.6	ebmcrau.fl	150
B.1.7	ebmsio2.fl	150
B.1.8	etch-metal.fl	151
B.1.9	gen-trl-photo.fl	151
B.1.10	gen-trl-photo10a.fl	153
B.1.11	generic-ebeam-dep1.fl	155
B.1.12	generic-ebeam-dep2.fl	156
B.1.13	metstr.fl	157
B.1.14	rie-sio2.fl	157
B.1.15	spin-on-res.fl	158
B.1.16	trl-mexp-ph.fl	158
B.1.17	trl-photo.fl	159
B.1.18	trl-piranha.fl	160

List of Figures

1-1	Concept for a capacitance-based proximity sensor	17
1-2	Concept for a capacitance-based lateral position sensor	18
1-3	Three-dimensional vibration detector of Heerens	20
1-4	Feedback Position Sensor for Linear Electrostatic Motor by Miller . .	21
1-5	Averaging technique to eliminate fabrication defects in driven and sensing electrode patterns	24
1-6	Illustration showing a particular shielding and guarding arrangement	25
1-7	Vertical mode couples with lateral mode	27
1-8	Tilting mode couples with lateral mode	27
1-9	Innovative concepts for high resolution capacitance-based lateral position microsensor (HCLPM)	28
1-10	Relationship between high resolution capacitance-based lateral position microsensor (HCLPM) and existing devices	29
1-11	Magnetic media in the high density memory storage system	30
1-12	Hierarchy of functions in a high density memory storage system . . .	31
2-1	System used to demonstrate the procedure for solving the capacitance problem	34
2-2	Boundary conditions for perfect conductors	38
2-3	Illustration of cavity and fringing field at the perimeter	39
2-4	Illustration of cavity and fringing field at the perimeter for a small gap	40
2-5	System in which the field along the perimeter does affect the solution	42

2-6	Electric field distribution in a rectangular tube for a capacitance calculation using parallel-plate assumptions	43
2-7	Rectangular conducting tube to illustrate a more complicated capacitance calculation	45
2-8	Potential distribution inside a rectangular conducting tube with $a = 1.3b$.	46
2-9	Potential distribution inside a rectangular conducting tube with $a = 10b$.	47
2-10	Electric Field Vector Map Inside a Rectangular Conducting Tube with $a = 1.3b$	48
2-11	Electric field vector map inside a rectangular conducting tube with $a = 10b$	49
2-12	Region of the bottom electrode in the rectangular conducting tube used in the capacitance calculation	50
2-13	Normalized capacitance as a function of the aspect ratio $\frac{b}{a}$	51
2-14	Periodic replication and extension of the rectangular tube	51
2-15	Full solution for the 1000 point grid, periodically extended cavity	52
2-16	Close-Up View of the Active and Non-Active Regions of the Extended Cavity	53
2-17	Close-Up View of the Electric Field in the Active and Non-Active Regions of the Extended Cavity	54
2-18	Electrode configuration undergoing a change in gap	55
2-19	Electrode configuration undergoing a tilting motion	56
2-20	Capacitance between a pair of tilting electrodes for varying angles	57
2-21	Sensitivity of an electrode configuration to tilting motions	58
2-22	Electrode configuration undergoing a lateral motion	59
2-23	Ratio of the sensitivities for the vertical and lateral sensing modes	60
2-24	Ratio of the sensitivities for the tilting and lateral sensing modes	61
2-25	In-plane electrode rotation during a lateral motion	62
2-26	Illustration of the piecewise linear output oscillation for lateral changes in position	63

2-27	Illustration of the change in area due to an in-plane rotation during a lateral motion	64
2-28	Illustration of the piecewise linear output oscillation for lateral changes in position with constant in-plane rotation	65
2-29	Steady drift in dielectric strength during a lateral change in position .	66
2-30	Set of spatially-phased electrodes used to decouple the position measurement from the drift component	66
2-31	Capacitance profiles of 0° and 180° spatially-phased electrodes for changes in position with and without a drift component	67
2-32	Algebraically combined capacitance profiles of 0° and 180° spatially-phased electrodes for changes in position with a drift component . . .	68
2-33	Compensation of drift in measurement at 0° spatial electrode through the use of multiple phase measurements	69
2-34	Set of spatially-phased electrodes used to attenuate the variation in gap across the sensor	70
3-1	Diagram showing motion of the driven electrode element traveling over the sensing electrode element	76
3-2	Diagram showing motion of the upper electrode relative to the lower electrode with width of approach w	78
3-3	Single electrode with width of approach w	78
3-4	Multiple electrodes which distribute the total width of approach w . .	79
3-5	Capacitance profile for the single and multiple electrode configurations	80
3-6	Three plane sensor electrode structure	80
3-7	Platten sensor electrode structure (Miller)	81
3-8	Preferred sensor electrode structure	82
3-9	Positioning of the spatially phased groupings of electrodes in the HCLPM	84
3-10	Spacing for isolation between electrodes and interconnects in the preferred sensor electrode structure	85

3-11	Illustration of the exponential decay in electric field around the perimeter of electrode edges in the preferred electrode structure	85
3-12	Example of the exponential spacing calculation for a small region of the preferred sensor electrode structure	86
3-13	Layout of electrodes on the sensing element	88
3-14	Magnified view of the lateral sensing array and interconnect structure	89
3-15	Magnified view of the insulating gaps and guard electrode between the sensing electrodes	90
3-16	Magnified view of the monitor sensing electrodes	91
3-17	Overlay of the driven pattern on top of the sensing pattern - magnified view	92
3-18	Illustration of common stray capacitances to external surfaces	92
3-19	Guard used to isolate the individual electrodes and interconnects in the high resolution position sensor design	93
3-20	Buffering of input and output signals to avoid large parasitic capacitances at the leads	93
3-21	Hybrid interface op-amp network for the sensing array of electrodes .	94
3-22	Inherently immune measurement of capacitance C_{1-2} with low input impedance current detector	95
3-23	Stray immune measurement of capacitance C_{1-2} with auto-balancing circuit design from Leip	96
3-24	Auto-balancing, stray immune capacitance detection circuit by Leip .	98
3-25	Simulation of the four phase lateral position sensing output for $M_{ref} = 10$ and $C_{ref} = 5pF$	99
4-1	Example of iterative process needed to resolve photomask patterns . .	103
4-2	Illustration of dissimilar yields in the HCLPM process and an integrated circuit process	104
4-3	Photo step in a positive resist lithographic process	105

4-4	Two different interconnect aspect ratios to illustrate the difference in minimum feature size	106
4-5	Two different types of interconnect structures, serial and parallel, with different yield requirements	107
4-6	Continuation of pattern transfer with chemical etching operation . . .	109
4-7	Isotropic and anisotropic post-etch profiles for wet chemical etching processes	110
4-8	Cross-sectional diagram of the finished driven element	112
4-9	Mask layout for the SE (sensing electrode) photomask pattern	115
4-10	Mask layout for the SP (sensing passivation holes) photomask	116
4-11	Overlaid mask layout for five photomask patterns	117
4-12	Completed SE chrome photomask pattern and plate	118
4-13	Completed RE chrome photomask pattern and plate	119
4-14	Process Flow Representation (PFR) fundamental structure for the HCLPM microfabrication process	120
4-15	Glass bushing pattern after the completion of Step 2 in the process .	121
4-16	Procedure for patterning the glass layer	122
4-17	Procedure for patterning the aluminum layer	124
4-18	Modulated resist sidewalls due to the high reflectivity of an aluminum layer	125
4-19	PYREX wafer with SE aluminum electrode pattern	126
4-20	SEM image of consecutive electrodes in the sensing electrode pattern	127
4-21	Split-screen SEM showing low and high magnification image of the electrode structure	128
4-22	SEM image showing relative size of human hair diameter ($50\mu m$), interconnect width ($7\mu m$), and electrode width ($200\mu m$)	129
4-23	SEM image of interconnect "T" and human hair	130
4-24	Diagram showing long, thin interconnect pathways	130
4-25	SEM image of contact pad in SE pattern	131
4-26	Alignment marks for SP layer relative to SE layer	131

4-27	Procedure for patterning silicon dioxide layer	132
5-1	Hybrid experimental sensing configuration on circuit board with copper interconnects	134

List of Tables

1.1	Limitations and benefits of representative group of capacitance-based lateral position sensors	23
1.2	Characteristics of operating modes in capacitance-based sensing . . .	28
2.1	Boundary conditions and properties of perfect conductors	38
2.2	Sensitivity ratios for operating modes in capacitance-based sensing . .	59
2.3	Dielectric electric field breakdown strengths	62
2.4	Summary of theory for capacitance-based lateral position sensor design	72
3.1	Key dimensions in the electrode and interconnect structures in the driven and sensing arrays of the HCLPM	87
4.1	Photomask layer names, associations, and specifications	114

Chapter 1

Introduction

This research has focused on the design and fabrication of an inexpensive capacitance-based sensor for resolving changes in lateral position that approach 10 nm. In addition, the sensor was designed to operate with a high slew rate and a long measurement range. Although the work presented here describes a lateral one-dimensional position sensor, a modest extension of this design can accommodate a second dimension.

The project began with a review of the state-of-the-art in capacitance-based position sensors, and then went on to identify the inherent performance limitations of the existing sensor designs. Next, the theory of electrostatics was used to study both the fundamental behavior of capacitance-based position sensors and the basic operation of some of the existing sensor designs. These analysis results were then used to design the prototype sensor. Finally, integrated circuit fabrication technologies were leveraged to build a prototype sensor. At the time that this thesis was written, the experimental phase of the research was being planned.

As each phase in the research is described in the thesis, intuitive arguments are used to clarify the theory. Since the most innovative features of the High resolution Capacitance-based Lateral Position Microsensor (HCLPM) are also the most intriguing, they are underscored at every opportunity. The introduction gives a brief description of capacitance-based position sensors, presents the existing designs for several basic lateral position sensors, summarizes the inherent performance limitations of the existing designs and lists the innovative design features that enable the

HCLPM to out perform the existing designs.

1.1 Summary of concepts for capacitance-based position sensors

There are two types of capacitance-based position sensors: vertical and lateral. In vertical, or proximity, sensors, the gap between two electrodes varies while the overlapping area of the electrodes remains fixed. In lateral position sensors, the area of overlap varies while the gap remains fixed. Although the operational mode of displacement is different in these two sensors, both use a change in capacitance to measure the associated motion. These devices have been implemented in applications as diverse as photomask alignment and thin-film thickness measurements. [1, 14]

But the benefit of great diversity in capacitance-based sensing also inevitably introduces an inherent coupling in position measurements, which may obscure the measurement that is of the most interest. By developing a better understanding of each operating mode, or sensed degree of freedom, techniques can be devised to decouple and sort additive measurements.

1.1.1 Vertical or proximity sensors

The first operating mode of capacitance-based position sensors is the proximity, or vertical, mode. The basic proximity sensor measures the distance between two closely spaced planes. In capacitance-based proximity sensors, the conducting probe is driven by a voltage or current source and the target surface is electrically grounded. Furthermore, the planes of charge are usually assumed to be parallel and properly shielded.

¹ As the gap between the probe and the target changes, the measured charge accumulation at the probe changes, thus indicating the proximity of the target surface to the probe (Figure 1-1).

The important characteristic of the proximity sensor is its high sensitivity: it

¹Shielding and guarding techniques will be described in Chapters 2 and 3

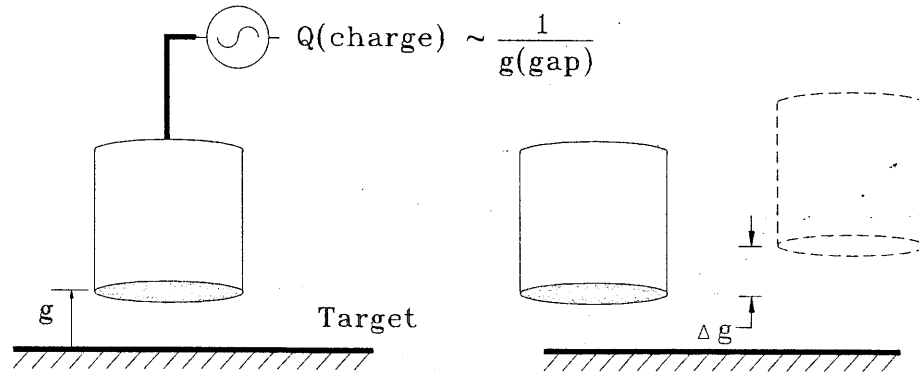


Figure 1-1: Concept for a capacitance-based proximity sensor

varies as the inverse square of the gap. In general, the capacitance of a proximity sensor is largest when the gap between the probe and target is the smallest. This is why high resolution proximity sensors typically operate with a small gap - a small gap translates into a large, more easily detected change in capacitance.

The main disadvantage of capacitance-based proximity sensors is their small operating range. Once the initial operating gap is chosen, the displacement range is limited to a small percentage of the initial gap. Linear measurements are possible only within this small range of displacement. The disadvantage is even more apparent as the operating gap is decreased to achieve a higher sensitivity. This "give and take" dilemma is common in all sensor designs, where higher performance in one area is accompanied by poorer performance in a second area. For most of the existing capacitance-based lateral position sensor designs, high sensitivities result in short measurement ranges. One of the goals in this research was to simultaneously increase both the range and sensitivity of the HCLPM by shrinking the size of the sensing elements and the operating gap. This goal is discussed further in Section 1.1.5 and Chapter 3.

1.1.2 Lateral position sensors

The second operating mode of capacitance-based position sensors is the lateral mode of displacement. Lateral position sensors are used to measure the change in position

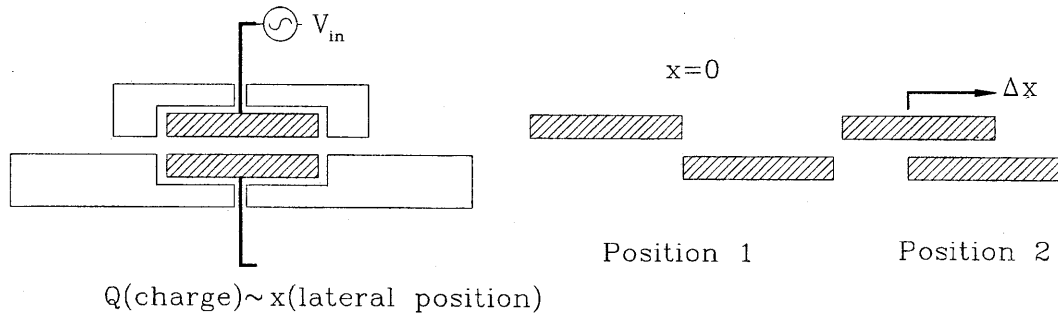


Figure 1-2: Concept for a capacitance-based lateral position sensor

of an element that moves parallel and relative to a fixed ruler. For capacitance-based lateral position sensors, the moving element is usually a voltage driven electrode and the fixed ruler is a current or voltage sensing electrode. The concept is illustrated in Figure 1-2. As the driven element moves relative to the fixed element, the capacitance changes as a function of the position. A converter of some kind is then used to interpret the output charge, Q , as a measure of the change in position, Δx .

The important operating characteristics of this sensor are measurement accuracy, sensitivity, linearity, range, resolution, and precision. Most of these qualities are determined in large part by the sensor fabrication method. For instance, the measurement accuracy can be only as good as the accuracy of the ruler, or measurement scale. Since the ruler accuracy is determined by the accuracy with which the ruler is constructed, the fabrication method must be chosen carefully. In contrast, the sensitivity is more dependent on the operating conditions of the sensor than on the method of construction. The highest sensitivities are attained when the operating gap is small. A comparison of the two different sensing modes shows that the vertical sensitivity is larger than the lateral sensitivity. This mismatch in sensitivities creates a condition known as the coupled-measurement problem. A more detailed description of the problem is given in Section 1.1.4. It is also important to note that the sensitivity of a capacitance-based sensor has two components: the sensitivity to the measurand (position) and the sensitivity to environmental fluctuations. These latter effects can be attenuated by making multiple measurements with reference capacitors.

A fundamental theoretical result shows that the linearity, sensitivity, resolution and precision all improve as the gap in Figure 1-2 between the driven and sensing electrodes decreases. This was the primary goal of the HCLPM design: design a lateral position sensor with an integrated gap, which is small, well defined, and constant during operation. This topic is revisited in Section 1.1.5 and Chapter 3.

1.1.3 Summary of the existing designs

A few researchers have implemented the concept in Figure 1-2 to achieve position measurement resolutions on the order of $0.1 - 1000nm$. Possible applications for these sensors have included: vibration measurements [16], photomask alignment [1], feedback position sensing for electrostatic linear motors [27] and thin-film profile characterization [14].

Each sensor design in these applications is similar to the other designs in three major respects: first, a change in capacitance indicates a change in lateral position; second, electrical guarding and shielding are used to shape the electrical field between the two electrodes; and third, an electrical signal detector of some kind is used to convert the change in charge into a position measurement. The major differences in the designs are governed by, whether a gap change or an area change produces the change in capacitance, whether the sensor is built for long range or short range measurements, whether a control system or a constrained design is used to maintain a constant gap, and whether conventional machining or microfabrication is used to build the sensor. The designs of Heerens and Miller will be used to illustrate these general design characteristics (refer to Items 1 and 2 in the list below).

1. Common design characteristics

- A change in position produces a change in capacitance, ΔC .
- A shielding enclosure and guarding electrodes are used to shape the electric field lines.
- An electrical signal detector is used to convert the charge into an associated change in position.

2. Individual design characteristics

- A change in area, A , gap, g , or dielectric constant, ϵ , is linked to the change in position, Δx .
- The sensor is designed for long range or short range travel.
- A feedback position control system simulates a constant gap or the sensor is restrained by design to maintain a constant vertical position and orientation.
- Conventional machining or microfabrication is used to build the sensor.

Three-dimensional vibration detector prototype by Heerens

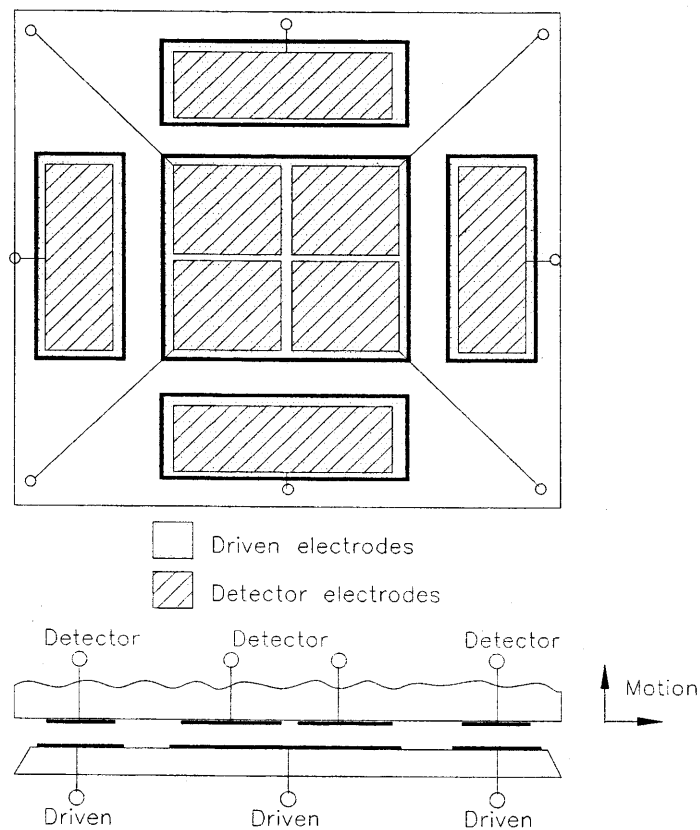


Figure 1-3: Three-dimensional vibration detector of Heerens

One existing lateral position sensor design is shown in Figure 1-3; it shows the configuration and operating concept of the Heerens three-dimensional vibration detector

prototype. [16] This sensor is capable of resolving $0.1nm$ changes in position over a range of $10 - 100\mu m$. Two electrodes carriers, one with electrically driven electrodes and the other with detector electrodes, are positioned across from one another to form several variable capacitors. As the two sets of electrodes move relative to one another, the charge detectors indicate the vertical and lateral amplitudes of displacement to within $0.1nm$. Note that this sensor uses a grouping of proximity and lateral position sensors to measure three-dimensional changes in position and orientation.

The key operating characteristics of the Heerens sensor are a small measurement range, a high resolution and a change in the overlapping area between electrode pairs. Some of these characteristics create performance limitations in a high resolution sensor. Section 1.1.4 summarizes these limitations.

Feedback position sensor for linear motor by Miller

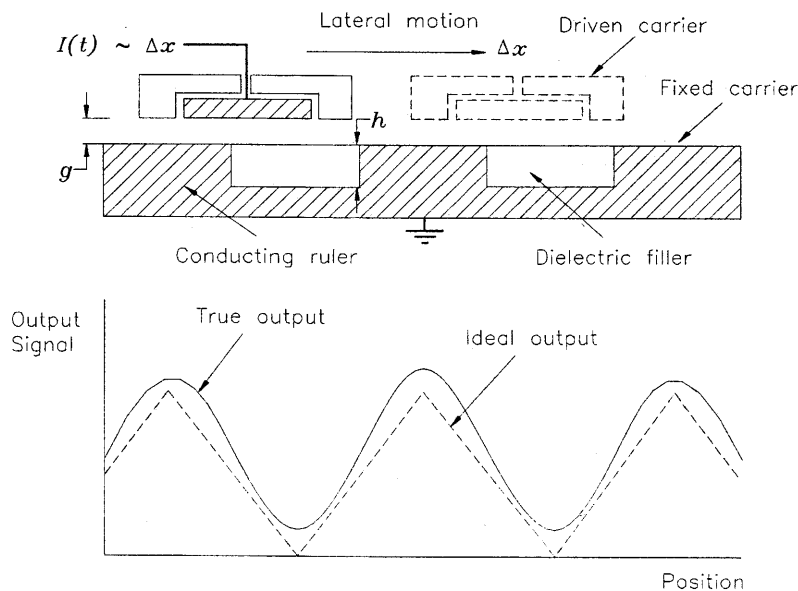


Figure 1-4: Feedback Position Sensor for Linear Electrostatic Motor by Miller

A second example of a lateral position sensor is shown in Figure 1-4. Miller first introduced this sensor design as a feedback sensor in a patent on two-dimensional linear electrostatic motors. [27] Although the resolution of the sensor was not given

in the patent, it seems likely that the resolution is approximately $0.1 - 1\mu m$.² As the driven electrode carrier scans the grounded fixed ruler, alternating pits of dielectric material modulate the mutual capacitance between the two surfaces. A maximum capacitance, and hence a maximum current, occurs when the driven element is directly above a square peak in the grounded plane. A minimum signal is generated when the driven element is directly above the pit of dielectric filler.

The Miller design uses a combination of changing gaps and overlapping areas to vary the capacitance between the two electrode carriers, generates a nonlinear (first order) periodic output signal over a long measurement range, uses feedback control to maintain a constant gap and forms the electrodes and interconnects with printed circuit board manufacturing methods. One major benefit of this design is the interconnect structure: it offers a significant reduction in the parasitic capacitance by placing the electrodes and leads within the surface of a circuit board. In spite of this advantage and others, the Miller design has several characteristics that curb the level of sensor performance (refer to Table 1.1).

1.1.4 Limitations and benefits of existing designs

The existing capacitance-based lateral position sensors have significant limitations on measurement resolution, accuracy, precision and range. These limitations are imposed by one or more of the following sensor design and manufacturing choices: the fabrication method, the shielding and guarding arrangement, a suitable gap control technique, a method to eliminate environmental disturbances and the capacitance detection circuitry. Although there are drawbacks to the existing designs, there are also several benefits. Table 1.1 lists the limitations and benefits of three state-of-the-art capacitance-based lateral position sensors. The references for each design are given in the table.

The design process for the HCLPM was guided by an understanding of performance characteristics. The next four sections give a more detailed account of what

²The length of each spatial period is $36\mu m$, so an interpolation factor of 100 yields an approximate resolution of $0.3\mu m$

Design	Limits	Benefits
Heerens [16]	Relatively crude method of construction, short range, poor gap control	11nm resolution, well placed guards and shields, differential measurement for compensation
Miller [27]	Nonlinear output characteristic, excessive fringing fields, complicated feedback gap compensation, 0.1 μ m resolution	Low interconnect parasitic capacitance, long range
SYLVAC [36]	Poorly placed guards, large operating gap, 1 μ m resolution	Sophisticated interconnect structure, long range

Table 1.1: Limitations and benefits of representative group of capacitance-based lateral position sensors

these characteristics are and how they affected the HCLPM design process.

Fabrication method

It is intuitively clear that highly accurate and precise sensor elements must be manufactured with highly accurate and precise processes. Conventionally machined sensors are often limited by the coarse precision of the machine tool or the machining operation. In contrast, microfabrication and other micromachining operations regularly produce structural components in high resolution, high precision and high accuracy sensors. Furthermore, integrated circuitry can be tailor made for sensors of this type and placed within the same monolithic package. An advantage of certain kinds of integrated circuitry is that the parasitic capacitances between the electrical leads and pads is reduced substantially.

The sensors of Heerens and Miller (Section 1.1.3) were both made with some type of microfabrication process; however, Miller used only a limited amount of circuit board techniques and Heerens used only a primitive form of photolithography. The Miller design has a major limitation in that circuit boards have an extremely non-uniform profile, which is caused by bending of the board and surface roughness. These limitations make it impossible to fashion electrode patterns with adequate spatial resolutions.

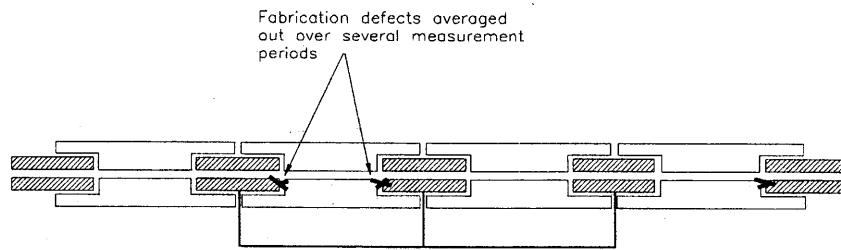


Figure 1-5: Averaging technique to eliminate fabrication defects in driven and sensing electrode patterns

Fortunately, performance is only partially limited by the fabrication method. For example, the long-range accuracy of a ruler will be poor unless the manufacturing process produces uniform period lengths; however, a clever design can partially compensate for these non-uniformities. Multiple measurements in certain spatial configurations are made to reduce these errors. The method is illustrated in Figure 1-5. In effect, the error is attenuated, or averaged out of the total measurement over many periods. Even if microfabrication is used to build the sensor, successive period lengths in grating-type structures vary statistically in photolithographic processes because statistics govern the behavior of such processes³. This same technique is used to compensate for environmental sensor drift.

Environmental disturbances

Changes in the local temperature, humidity and pressure will contaminate the capacitance measurement from a system like the one shown in Figure 1-2. Many of the existing sensors make differential measurements or use a reference capacitor to compensate for the effects of environmental drift. [20, 17, 21, 34, 28] Section 2.4.7 discusses the compensation techniques used in the HCLPM.

³MIT course number 6.781 lecture notes, *Submicron- and Nanometer-Structures Technology*, Professor Henry I. Smith, 1995

Shielding and guarding configurations

Shields and guards are used in capacitance-based sensors to isolate the sensing element from external capacitive coupling. The idea is to prevent time-varying electric fields from inducing charge on the sensing electrode through a "stray" capacitance. This stray capacitance adds to the sensed capacitance, thereby contaminating the measurement. Optimum shielding is characterized by a complete enclosure, which is impermeable to the external electric field (see Figure 1-6). Capacitance-based lateral

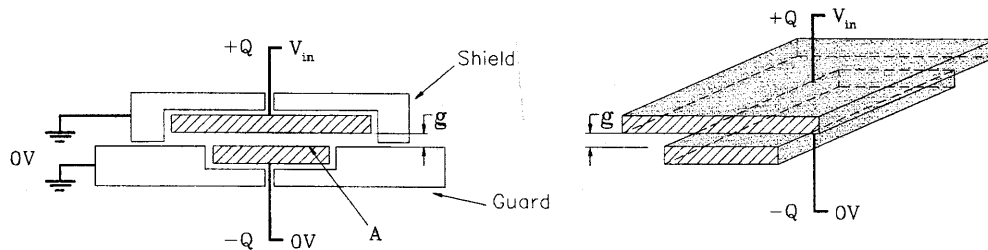


Figure 1-6: Illustration showing a particular shielding and guarding arrangement

position sensors typically operate over small ranges, so the shielding enclosure can be easily constructed as in the Heerens three-dimensional vibration detector (Figure 1-3). However, there is a problem with designing an electrical interface to a moving sensor if it travels along an extended measurement range.

The most effective way to avoid this problem is to use a small operating gap. This configuration traps the electric field within the space between the driven electrode surface and the sensing electrode surface (see Figure 1-2). It is also important to use a changing area, A , and not a changing gap, g , to modulate the capacitance. As shown in Figure 1-4, the Miller design uses a changing gap, which generates an inherently nonlinear output signal. The source of this nonlinearity is the fringing effect at the side walls of the dielectric filler. A more linear profile could be obtained if the electric field lines were constrained to be straight from the top surface to the bottom surface by eliminating the side walls.

Detection circuitry

Many of the existing sensor designs use sophisticated detection circuitry to minimize the effects of both stray and parasitic capacitances. Huang [32] gives an excellent review of the research in this area that has occurred within the last two decades. The most common technique uses impedance bridges and is discussed by Jones and Richards.[20] Switched capacitor filters with analog circuitry have also been shown to produce high resolution capacitance measurements. [12]

Coupled-measurement problems

One challenge in designing a high-resolution lateral position sensor is to reduce the effect of extraneous operating modes (degrees of freedom) on the measurement mode of operation. This includes, but is not limited to, an adequate level of vibration isolation. Contemporary sensor designs use sophisticated techniques in feedback control to maintain a constant and uniform gap.

The mismatch in sensitivity, which was illuded to in Section 1.1.2, makes it very difficult to measure changes in lateral position on the order of $10nm$ when there are variations in the gap that muddle the measurement. The source of difficulty is the relatively high sensitivity of the vertical sensing mode as compared to the lateral sensing mode.

Figures 1-7 and 1-8 illustrate the problem. Lateral position measurements are prefaced by the assumption that the motion is entirely in the lateral direction. In one possible measurement senario, the output of the sensor due to the change in the gap may be on the same order as the output due to the lateral change in position (Figure 1-7). Since the assumption of a purely lateral motion is violated in this case, the measurement is contaminated by the coupled vertical motion. In a second senario, the output due to the rotation of the driven element may be on the same order as the output due to the lateral change in position (Figure 1-8). This coupled tilting motion also contaminates the lateral position measurement. Both of these senarios must be avoided when making high resolution lateral position measurements. The HCLPM is

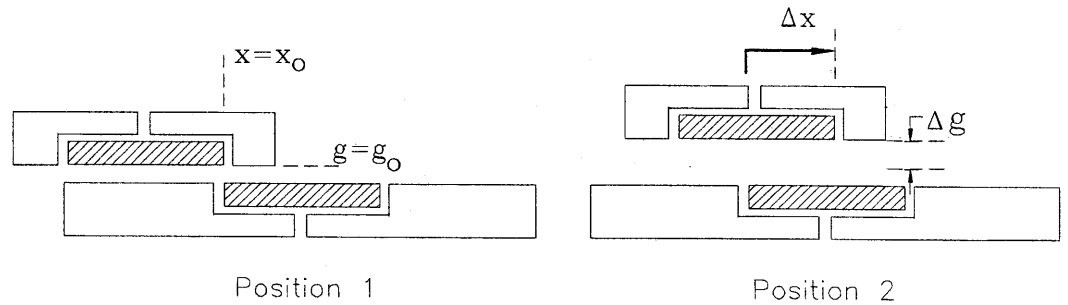


Figure 1-7: Vertical mode couples with lateral mode

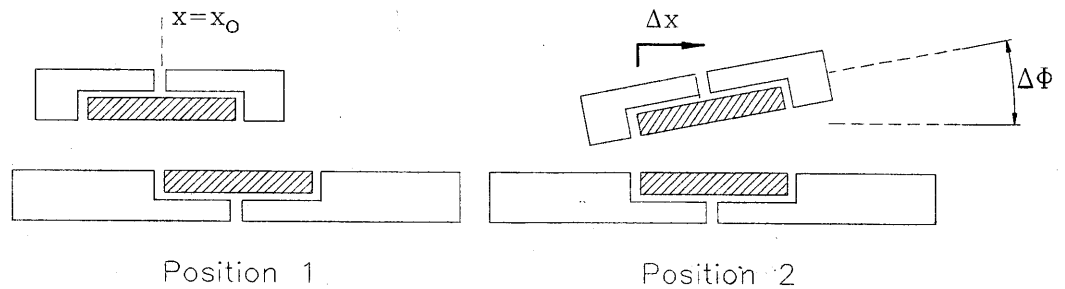


Figure 1-8: Tilting mode couples with lateral mode

designed to compensate for these sources of error.

1.1.5 Innovative aspects of the improved design

The HCLPM improves upon the existing sensor designs in several respects (refer to Figure 1-9). First, a partial contact design is used to maintain an open-loop constant gap during operation, instead of the more sophisticated closed-loop scheme that was used in many of the previous designs. Second, a full differential spatial electrode configuration is used to minimize the statistical errors sustained during microfabrication (i.e. variations in the period, profile defects, etching variations). Third, the electrode surfaces are enclosed as much as possible within a microfabricated

Mode	Description	Sensitivity Variation $\frac{\partial C}{\partial \alpha}$
Proximity	Varying gap with fixed lateral position	$\frac{1}{g^2}, \alpha = g$
Lateral	Varying lateral position with constant gap	$\frac{1}{g}, \alpha = x$

Table 1.2: Characteristics of operating modes in capacitance-based sensing

shielding layer to minimize any stray capacitance. A list of the innovative aspects of the HCLPM design is given below.

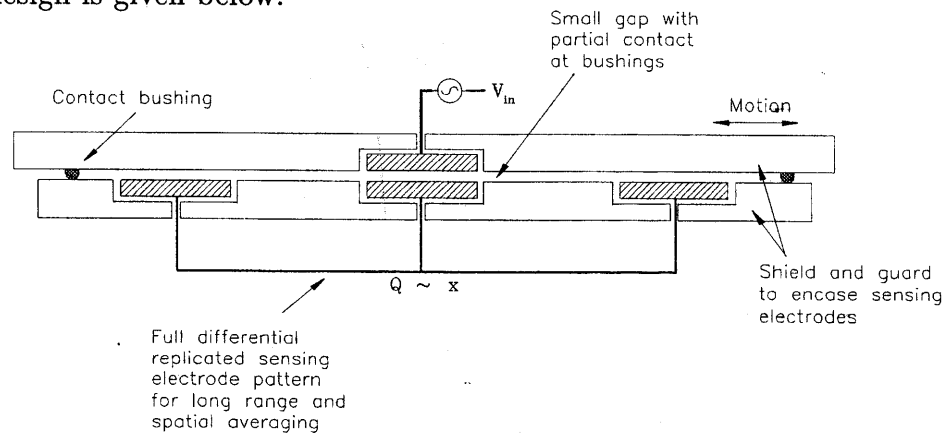


Figure 1-9: Innovative concepts for high resolution capacitance-based lateral position microsensors (HCLPM)

1. Partial contact operation for open-loop gap control,
2. Full differential spatial electrode configuration to minimize the effect of errors sustained during fabrication and created by environmental drifts,
3. Integrated shielding enclosure for minimizing parasitic and stray capacitances.

Each item in the list above raises the performance level of the HCLPM. Item 1 has the following benefits: minimizes the coupled-measurement problems by restraining those motions that are not being measured; easily maintains a small operating gap for higher sensitivity, longer range and higher resolution measurements; and traps

the electric field within the space between the two electrode surfaces to enhance the parallel plate behavior for better linearity. Item 2 enables the HCLPM to sense direction as well as position, doubles the sensitivity, and compensates for errors in the fabrication process by averaging over many sensing periods. Lastly, Item 3 isolates the sensing electrodes from the additive effects of external conductors and mutual capacitances, and improves the linearity of the sensor characteristic by straightening the local fringing fields. These concepts are illustrated in Figure 1-9. The relationship between the HCLPM and the existing sensor designs is shown in Figure 1-10.

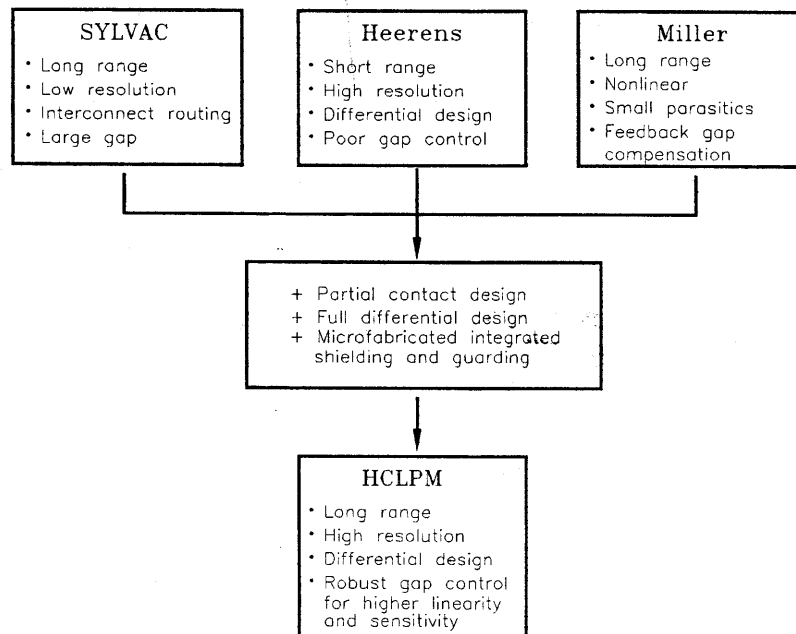


Figure 1-10: Relationship between high resolution capacitance-based lateral position microsensor (HCLPM) and existing devices

1.2 Motivations for a lateral position microsensor

An inexpensive high resolution lateral position sensor would be indispensable in many applications. In the laboratory, it would offer researchers a high performance alter-

native to optical-based interferometer systems. The HP Interferometer is a typical example of an optical distance measuring sensor. The minimum cost of this unit is \$4200.00 with measurement resolutions on the order of $10nm$. However, alignment is often difficult and time consuming. The HCLPM would eliminate the expensive and time intensive alignment procedures that are associated with optical systems. In the data storage industry, it could also be used in a high density data storage system to locate individual bits of information in the storage medium. Finally, it could enhance many microelectromechanical systems by providing the engineer with greater design flexibility.

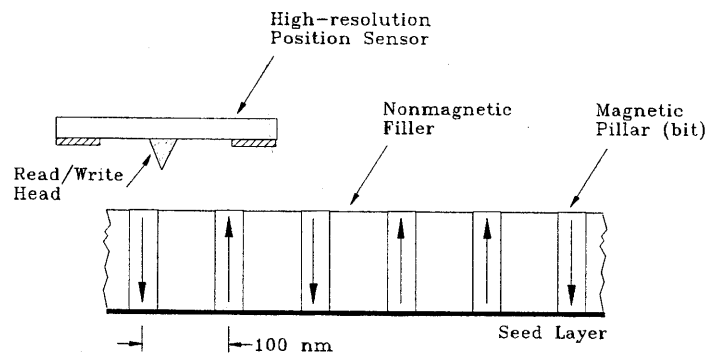


Figure 1-11: Magnetic media in the high density memory storage system

1.2.1 High density memory storage

The long-term goal of the Mechatronics Research Laboratory (MRL) is to design, build, and test a High Density Memory Storage (HDMS) system. The storage media in these systems are dense arrays of magnetic pillars, which carry positive (up) or negative (down) magnetic fields. Since the individual bits of information in the media are separated by only $100nm$, submicron tracking techniques are essential (Figure 1-11).

With this resolution requirement in mind, the MRL nanoprecision research team has focused on three enabling technologies for the HDMS device: actuation, sensing, and data storage (see Figure 1-12). The HCLPM can be modified to meet the sensing

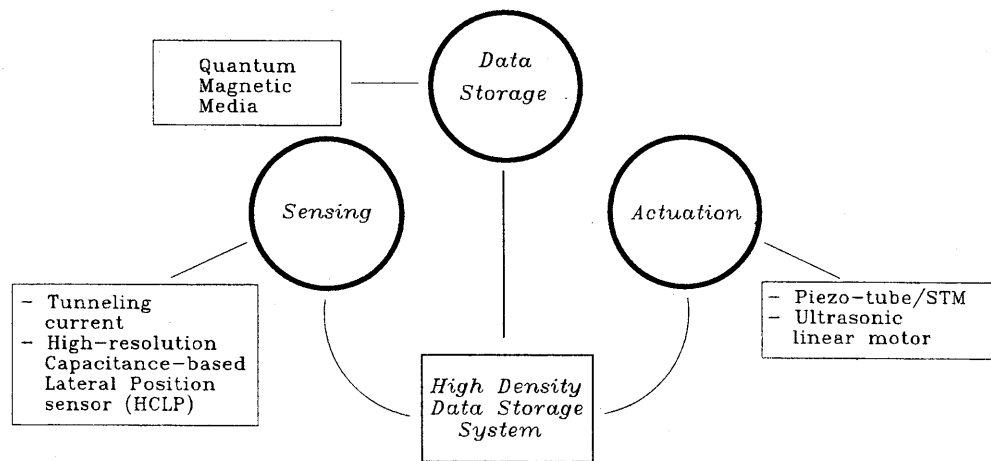


Figure 1-12: Hierarchy of functions in a high density memory storage system

needs in the HMDS system.

Former students have already demonstrated nanometer positioning resolution with an ultrasonic linear motor and a piezotube actuator. [5] Tens-of-angstroms sensing resolution was also achieved with a tunneling current probe. [3] The research herein revisited the topic of high resolution sensing in an effort to boost measurement repeatability and stability with capacitance-based sensing. Other MRL researchers are attempting to build a complete HMDS system by integrating the actuation, sensing, and memory storage technologies.

1.2.2 Microelectromechanical devices and related applications

There are opportunities to use this sensor in other applications as well. For instance, capacitance-based sensing is the key measurement technique in microelectromechanical systems (MEMS). Pressure sensors, acceleration sensors, and gyroscopes have all been micromachined and equipped with capacitance sensors to measure minute changes in position. [24, 31, 4] Furthermore, most of these devices use proximity sensing in which the separation between two surfaces varies with a physical input. MEMS designs gain new flexibility for larger ranges of motion with the HCLPM.

For example, the angular rate gyroscope has recently been miniaturized by combining bulk and surface micromachining processes [35, 22]. In these sensors, an input

angular velocity produces a measurable deflection output. Capacitance-based proximity sensors are commonly used for these gyros in comb-drive configurations. An alternative to the comb-drive is the HCLPM. An advantage of the new design is the relative ease with which metal is uniformly deposited and patterned as compared to the process for bulk micromachining of the comb-drive fingers.

1.3 General overview of thesis

The remaining chapters of the thesis present an overview of the pertinent electrostatic theory, use the theory to analyze existing sensor designs and to develop a concept for an improved design, devise a microfabrication process to build the sensor, and describe the results of the extensive fabrication process.

Chapter 2

Theory

Maxwell was the first to invoke the theory of electromagnetism to define the mutual capacitance between two bodies that carry charge. In his historical treatise [26], he not only defined the meaning of capacitance, but also gave the first precise description of the guard ring, which was introduced by Lord Kelvin in 1867. Since then many researchers have applied the definition of capacitance to track changes in physical variables like pressure [24, 9], concentration [18], and moisture content in materials [2].

The most important aspect of electromagnetic theory in this research project is the link between electrode configuration and mutual capacitance. In fact, the geometry of a set of charged surfaces completely determines the capacitance between those surfaces. The HCLPM design process is principally based on this relationship between configuration and capacitance, and aims to optimize the performance of the sensor by rearranging the electrode configuration. Chapter 2 describes the first step in the optimization process: a general understanding of capacitance, a method to calculate it, and the factors which enhance and distort it.

2.1 Mutual capacitance - a theoretical framework

The mutual capacitance is a ratio between the induced charge on one body due to the presence of a second body, and the potential difference between the two bodies

(electrodes):

$$C_{1-2} = \frac{Q_{1-2}}{V_{1-2}} \quad (2.1)$$

The crucial property of the electrodes, 1 and 2, in Equation (2.1) is the ability to carry a charge. The calculation of the capacitance, C_{1-2} , is termed the capacitance problem.¹ There are three steps in the calculation:

1. Calculate the electric field distribution in the surrounding medium;
2. Calculate the charge distributions on the two bodies;
3. Evaluate the capacitance with Equation (2.1).

The goal in the capacitance problem is analytical in nature: solve for the unique capacitance in a fixed configuration of charged bodies. This problem is slightly different than the sensing problem, in which a varying charge is created by the combination of a variable capacitance and a potential difference. In this case, the charge is the key parameter. Section 2.4.1 discusses this subtle difference in terminology.

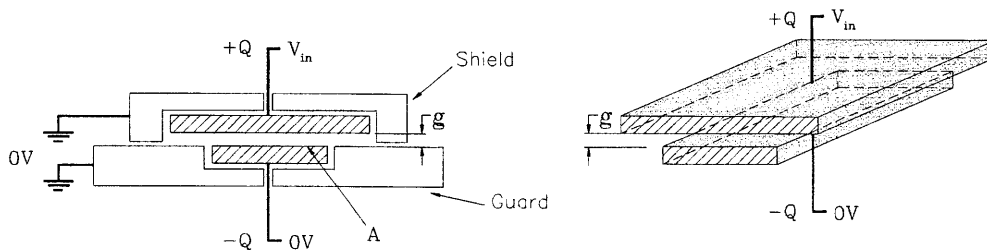


Figure 2-1: System used to demonstrate the procedure for solving the capacitance problem

Steps 1 through 3 in the calculation are only tractable if special assumptions are made. The starting point is the full set of Maxwell's equations, after which restrictions on the frequency range, electrode material and geometry, and the surrounding medium

¹In what follows, the more general term *capacitance* is substituted for *mutual capacitance*.

produce an estimate of the capacitance. Section 2.2 summarizes the restrictions and intermediate calculations in the problem. The simple electrode geometry in Figure 2-1 is used to demonstrate the solution procedure.

2.2 Simplifying assumptions and intermediate calculations

The complete theory of electromagnetism is dense and unmanageable in many applications. Fortunately, Maxwell's equations can be simplified by limiting the frequency of the input and output signals, selecting a medium with simple constitutive laws, specifying the materials and the appropriate boundary conditions and idealizing the dimensions of the system. The full set of electromagnetic equations describe the interaction, or coupling, between the electric and magnetic domains.

$$\nabla \times \mathbf{E} = -\frac{\partial \mathbf{B}}{\partial t} \quad (2.2)$$

$$\nabla \times \mathbf{H} = \mathbf{J} + \frac{\partial \mathbf{D}}{\partial t} \quad (2.3)$$

$$\nabla \cdot \mathbf{B} = 0 \quad (2.4)$$

$$\nabla \cdot \mathbf{D} = \rho_v \quad (2.5)$$

The output field vectors in Equations (2.2) through (2.5) are defined as follows: \mathbf{E} is the electric field strength ($\frac{V}{m}$), \mathbf{D} is the electric field density ($\frac{C}{m^2}$), \mathbf{H} is the magnetic field strength ($\frac{A}{m}$), and \mathbf{B} is the magnetic flux density ($\frac{W}{m^2} = tesla$). The input sources are the charge density, $\rho_v(\frac{C}{m^3})$, and the current density, $\mathbf{J}(\frac{A}{m^2})$. In the sections that follow, the relevant assumptions will be used to simplify these equations.

2.2.1 Low frequencies and small structures

If either the frequency of excitation, ω , is small or the length of the surface of charge, L , is small in relation to the wavelength of the excitation frequency, then the electric field equations are decoupled from the magnetic field equations. In this case, only

the electric field and its two governing equations are needed to solve the capacitance problem.

$$\nabla \times \mathbf{E} = \mathbf{0} \quad (2.6)$$

$$\nabla \cdot \mathbf{D} = \rho_v \quad (2.7)$$

These two equations are the subject of electrostatic field theory, which accounts only for the zeroth order behavior of the electric field. If the frequency or the length of the structure becomes too large, electrostatic theory is abandoned and electroquasistatics is used to account for the first, second and higher order effects. The HCLPM is designed using electrostatics; a comparison of the first and second order terms shows that the second order spatial effects are negligible. [33] One advantage of MEMS and other microfabricated devices is their small size. This characteristic lessens the full dynamic modelling effort to a more manageable quasistatic or static effort.

2.2.2 Selecting a dielectric medium

In most problems either the electric field or the potential function is calculated or known beforehand and is then used to find the charge density in Equation (2.7). Prior to this step, the relationship between \mathbf{D} and \mathbf{E} is selected. This requires an assumption of the type of medium in which the electric field exists.

The constitutive law that relates the electric field to the field density involves the dielectric strength of the medium in the problem. In the case of Figure 2-1 the medium is air, so the dielectric strength is approximately equal to the permittivity of free space, ϵ_o . Since air is an isotropic, non-dispersive electromagnetic medium, the two field vectors are related to one another through the permittivity:

$$\mathbf{D} = \epsilon_o \mathbf{E} \quad (2.8)$$

Although the relationship in Equation (2.8) makes it possible to solve the problem at an instant in time, ϵ_o is typically a function of temperature, humidity, and frequency;

therefore, as these parameters change in the environment, ϵ_o changes as well, and thus the form of Equation (2.8) changes. This change is the topic of Section 2.4.7, which discusses output drift, its link to the environment, and one method of compensation.

After having established the constitutive law, Equations (2.6) and (2.7) are usually expressed in a combined form, which is based on the mathematical definition of a potential function for a vector field, $\mathbf{E} = -\nabla\phi$. The modified equation uses the property in vector calculus that $\nabla \times \nabla\phi = \mathbf{0}$.

$$\nabla \cdot \epsilon_o(-\nabla\phi) = \rho_v \tag{2.9}$$

Equation (2.9) is termed the Poisson equation. In the event that there is no charge in the solution volume, the equation reduces to the Laplace equation:

$$\nabla^2\phi = 0 \tag{2.10}$$

This equation is widely applicable to media like air that cannot store appreciable amounts of charge.

2.2.3 Properties of the electrode material

Having already defined the medium in which the electric field propagates, the material properties of the electrodes on which the electric charge is stored must also be defined. In Figure 2-1 and throughout this research project, conducting materials have been selected because there is little or no lossy capacitance in conductors. In other words the charge on a conductor is held at the surface, where there is more than enough charge without needing to penetrate the surface. This is in contrast to semiconductors like silicon and germanium, which have exceptionally deep charge centers with large capacitances that extend into the electrode material.

The properties and boundary conditions at the conductor surface stem from the large supply of free electrons in a metallically bonded structure (see Figure 2-2). The first condition is that the electric field is zero inside a perfect conductor. Since there

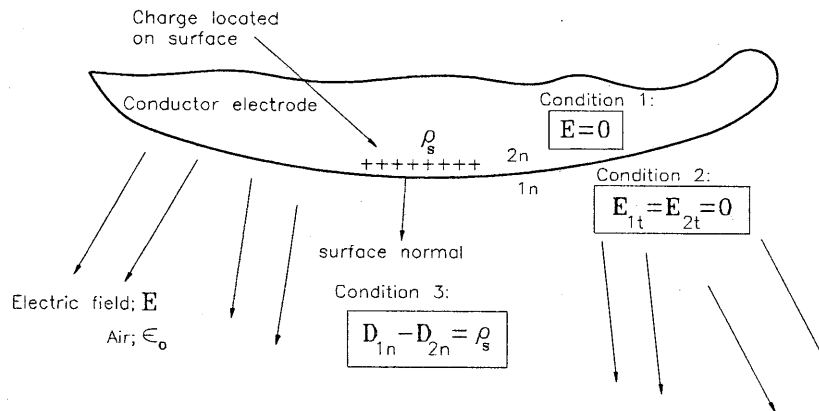


Figure 2-2: Boundary conditions for perfect conductors

are no charges inside the conductor, there can be no electric field there either. Second, the electric field in the surface plane is zero; i.e. the electric field is normal to the surface of a conductor. If there were a nonzero tangential electric field, then there would be a corresponding current along the surface of the conductor with no resistance. An infinite current is not possible; therefore, the second boundary condition must be true. The third boundary condition deals with the discontinuity in the perpendicular electric field across the surface of a conductor. From Equation (2.7) the divergence of the field density can be interpreted as the flux per unit area of the normal component of \mathbf{D} over a small section in the surface (Figure 2-2). This interpretation implies an equality between the flux and the charge density per unit area. The boundary conditions are summarized in Table 2.1.

Number	Condition
1	$\mathbf{E} = \mathbf{0}$ inside a conductor
2	$\mathbf{E}_{1t} = \mathbf{E}_{2t} = \mathbf{0}$
3	$D_{1n} - D_{2n} = \rho_s$

Table 2.1: Boundary conditions and properties of perfect conductors

Note that these conditions are only true for *perfect* conductors. If the conductor has a finite conductivity, then the tangential electric field at the boundary between the medium, material 1, and the conductor, material 2, is continuous but is not equal to

zero: $E_{1t} = E_{2t}$. The restriction in Condition 1 is also modified slightly for imperfect conductors: $E = 0$ inside the bulk of an imperfect conductor but not within the skin depth. Aluminum, copper, gold and silver can all be considered perfect conductors because their skin depths are very near zero. [33]

2.2.4 Electric field distribution near structural edges

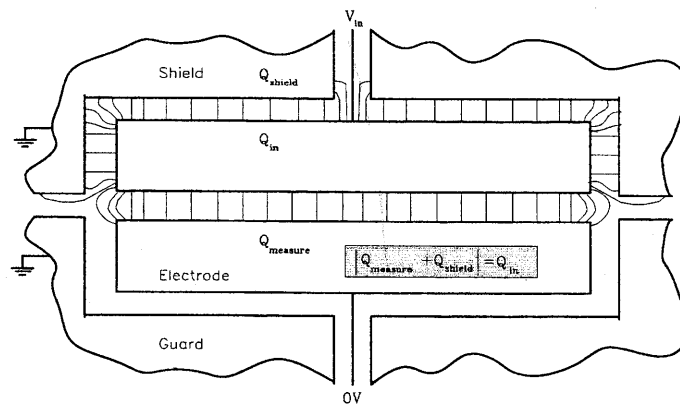


Figure 2-3: Illustration of cavity and fringing field at the perimeter

Figure (2-3) is a magnified view of the cavity formed between the two electrodes and the shield and guard in Figure (2-1). The conditions in Table 2.1 have been used to generate the electric field lines within the cavity. There are four characteristics to note in the figure [29, 33]:

1. The electric field in the bulk of the region between the two electrodes is uniform and parallel;
2. The regions at the perimeter of the electrode plates are linked by non-parallel fringing electric fields, which are synonymous with a non-uniform distribution of the surface charges;
3. There are no field lines linking the surfaces of equal potential, so there are neither induced charges nor mutual capacitances between those surfaces.

4. The total charge is conserved: $Q_{in} = |Q_{measure} + Q_{shield} + Q_{other}|$; or when the shield is a strict enclosure, $Q_{in} = |Q_{measure} + Q_{shield}|$.

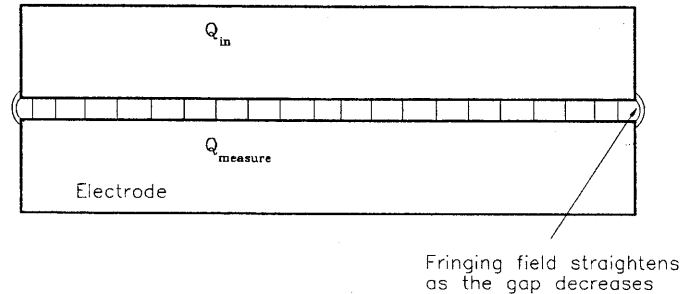


Figure 2-4: Illustration of cavity and fringing field at the perimeter for a small gap

By adjusting the configuration of the sensor electrodes, each of these characteristics can be adjusted to optimize the design for performance. For example, Section 2.2.5 makes use of Item 1 by decreasing the gap between the two electrodes. As the gap becomes smaller, the center regions of the electrodes become much closer to one another in relation to the distance between their perimeter parts. Since the electric flux is uniform at the center, the uniformity tends to spread from the center to the perimeter of the electrodes. A more uniform electric flux creates a more uniform charge distribution, which is more easily and accurately modelled (see Figure (2-4)). The simplified, parallel-plate model leads to accurate values for the capacitance that are calculable from the design.

The other characteristics are equally important for optimizing the sensor design. Item 2 is derived from conditions 2 and 3 in Table 2.1. Condition 2 creates perpendicular field lines at the surface of the electrodes, while condition 3 translates the non-uniform electric field into a non-uniform surface charge density. By maintaining a uniform electric field at the edge of the sensing electrode, the charge distribution is more uniform and the capacitance calculation is more accurate for the design. Item 3 is an extension of the definition of capacitance, Equation (2.1): there can be no charge induced between two surfaces at the same potential; thus, there can be no capacitance between them. Finally, Item 4 in the list simply states that all conductors

to which there is a clear path from the charged conductor, and at which the potential is different than the charged conductor, will carry part of the induced charge. In other words, there is a surplus of capacitors in the immediate surroundings of most systems with charged surfaces. Even the floor, walls, and ceiling of a room act as electrodes in small, yet measurable capacitors. A high resolution capacitance sensor must reject these strays with intelligently designed shielding and guard configurations. Section 3.3.1 discusses the stray rejection mechanism in the HCLPM design.

2.2.5 Idealized system dimensions

The Laplace equation (Equation (2.10)) defines a three-dimensional model of the electric potential inside a charge-free region. In many applications, the full three-dimensional model can be simplified to a two-dimensional model by assuming that the potential is invariant in the third dimension. For example, in Figure 2-1 the electric potential is found in the region surrounded by the upper and lower electrodes and the guard and shield. The complete solution describes the potential along the entire length of that cavity. Since the depth dimension into the page is much larger than the thickness and width dimensions, the depth dimension can be idealized as infinite compared to the planar dimensions. In this way the Laplace equation is simplified to a two-dimensional equation in the plane. Once the solution is found, it is replicated along the axis into the page of Figure 2-1 to obtain the full solution.

Other assumptions can also be made to simplify certain problems. For instance, it is reasonable to assume that the field inside the region between the upper electrode and the smaller lower electrode in Figure 2-1 is independent of the field at the perimeter of the solution cavity. By working under this assumption, the Laplace equation is only solved in the region between the two electrodes where the electric field is uniform and parallel. The guard at the edges of the small lower electrode promotes a uniform electric field in those regions (refer to Section 2.2.4). In other words the guard electrode is used to satisfy the parallel-plate assumption, which makes the problem easier to solve. Note that in the case where one electrode is larger than the second electrode, the electrode with the least surface area determines the amount of induced

charge, and hence the capacitance, between the two surfaces.

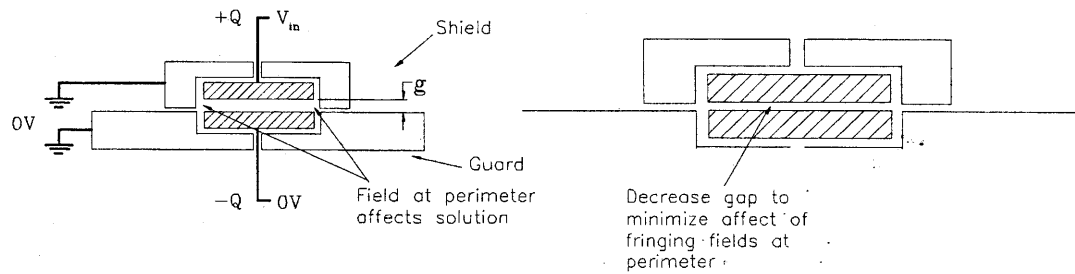


Figure 2-5: System in which the field along the perimeter does affect the solution

There are problems in which the field around the perimeter of the two electrodes does affect the solution. A typical example of this is shown in Figure 2-5. The fringing fields at the perimeter near the guard and shield distort the electric field between the two electrodes. This alters the charge distributions on the electrodes, which in turn alters the capacitance. Section 2.2.4 and Figure 2-4 showed that a decrease in the gap between electrodes lessens the affect of the fringing electric field on the capacitance calculation.

2.3 Calculation of mutual capacitance

There are two types of capacitance: mutual and self capacitance. Mutual capacitance is defined by Equation (2.1). It measures the amount of induced charge between two electrodes at different potentials. Self-capacitance is also a term that is often used. It is the ratio between the total charge across a conductor to the potential of that conductor. This research project focuses on the mutual capacitance problem. One surface, the voltage-driven electrode, induces a charge on a second surface, the charge-sensing electrode, by way of the mutual capacitance between the two surfaces.

2.3.1 Example using the parallel-plate assumptions

The procedure for calculating the mutual capacitance between two conductors is given in Section 2.1. Step 1 is to calculate the electric field in the cavity between the con-

ductors. The simplifying assumptions in Sections 2.2.1 through 2.2.5 make this easy. Under those assumptions the electric field is uniform and parallel throughout the region above the lower electrode. Section 2.2.5 also demonstrated that the configuration of electrodes, shields, and guards in Figure 2-1 satisfies these parallel-plate assumptions. The magnitude of the electric field, \mathbf{E} , within the cavity above the lower electrode is

$$E = \frac{V_{in}}{g} \tag{2.11}$$

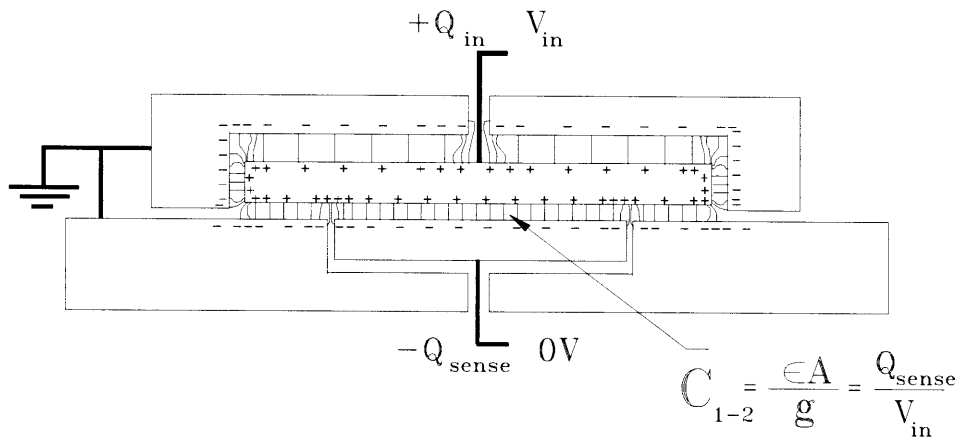


Figure 2-6: Electric field distribution in a rectangular tube for a capacitance calculation using parallel-plate assumptions

Since the electric field points into the lower electrode, the sign of the induced charge is negative. Figure 2-6 illustrates the shape of the electric field throughout the entire cavity and the distribution of the charge on each surface. Note the accumulation of charge at the corners; the electric field density is the highest in these regions. Also note that each of the surrounding electrodes shares part of the charge that is induced by the driven electrode (Item 4 in Section 2.2.4).

Step 2 is to calculate the induced charge on the bottom electrode. From Condition 3 in Table 2.1,

$$\epsilon_o E = \rho_s \tag{2.12}$$

An integration over the entire rectangular electrode yields,

$$Q = -\frac{\epsilon_o A}{g} V_{in} \quad (2.13)$$

The final step is to calculate the capacitance in Equation (2.1):

$$C_{1-2} = -\frac{\epsilon_o A}{g} \quad (2.14)$$

Note that the capacitance is negative in this case because the induced charge on the sensing electrode is negative (Equation (2.13)). The negative sign is usually omitted because the voltage difference between the top and bottom electrodes determines the sign of C_{1-2} . Equation (2.14) is the most commonly used formula for capacitance; however, it is only by design that most capacitance sensors operate with this value of capacitance.

2.3.2 Example of a more accurate capacitance calculation

As an example of a slightly more complicated calculation, consider the system in Figure 2-7. The system is assumed to be isolated from any external charges or surfaces. A voltage V_{in} is applied to the upper electrode, and the bottom electrode is grounded. Since all of the electric flux terminates on the bottom electrode, it must have a charge $-Q_{in}$ distributed across its surface. The goal is to find the shape of the charge distribution and to calculate the capacitance between the upper electrode and a small portion of the bottom electrode.

Shen and Kong use the method of separation of variables to solve for the potential inside the cavity. The solution for the potential, Φ , is an infinite series in x and y :

$$\Phi[x, y] = \frac{4V_{in}}{\pi} \sum_{n=\text{odd}}^{\infty} \frac{\sin(\frac{n\pi x}{a}) \sinh(\frac{n\pi y}{a})}{n \sinh(\frac{n\pi b}{a})} \quad (2.15)$$

At $y = b$ the sum converges to V_{in} ; at $y = 0$ it is zero. The solution for the entire cavity is shown in Figure 2-8, where the vertical axis represents the potential.

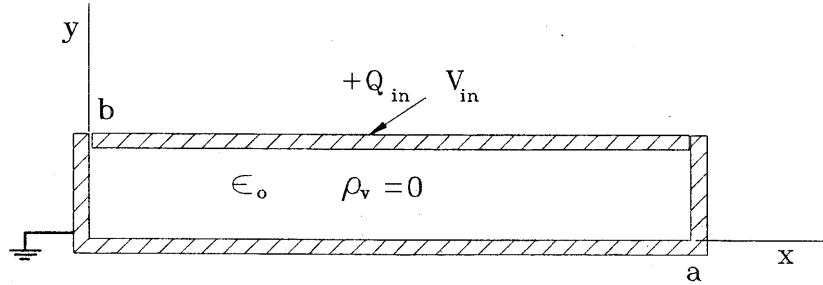


Figure 2-7: Rectangular conducting tube to illustrate a more complicated capacitance calculation

A separate Matlab script was used to compute each of the analytical and numerical solutions in this thesis. The script used to generate Figures 2-8 through 2-11 was *rectube.m*, Section A.1.

With $a = 20$ and $b = 15$ (normalized length units) the curvature of the potential at the corners diffuses into the center of the cavity. As the length grows to five or six times the height, the side walls no longer affect the potential distribution in the center (Figure 2-9). This is the configuration in which the parallel-plate assumption is accurate.

The clearest indicator of parallel-plate behavior is a uniform, parallel electric field. Figures 2-10 and 2-11 show the two dimensional electric fields for the potential distributions in Figures 2-8 and 2-9, respectively. The vector map is skewed near the bottom electrode for $a = 1.3b$ because the sidewalls are relatively close to the center of the cavity. In contrast the tube configuration with $a = 10b$ has a parallel vector map, which extends from the bottom electrode to the input electrode. The design goal in most capacitance-based sensors is to create a uniform potential distribution, as this is the first step toward a highly linear output.

Step 1 in the capacitance calculation is to calculate the electric field: this is simply the gradient of the potential function in Equation (2.15). Step 2 is the charge calculation for the particular area on the electrode. Figure 2-12 shows the region of the grounded electrode on which the induced charge is found. The charge calculation

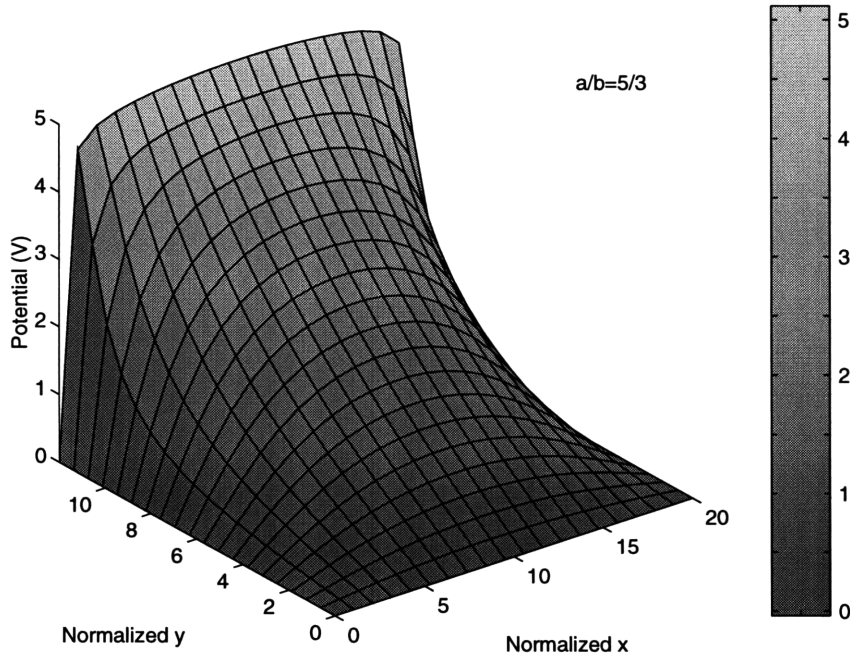


Figure 2-8: Potential distribution inside a rectangular conducting tube with $a = 1.3b$.

is done in two stages. First, the discontinuity in the perpendicular electric field density is used to find the surface charge density (Condition 3 in Table 2.1) :

$$\Delta D_y = (\epsilon_o E_1 - \epsilon_o E_2)|_{y=0} \quad (2.16)$$

$$= -\epsilon_o \frac{4V_{in}}{a} \sum_{n=\text{odd}} \frac{\sin(\frac{n\pi x}{a}) \cosh(\frac{n\pi y}{a})}{\sinh(\frac{n\pi b}{a})} |_{y=0} \quad (2.17)$$

$$= -\epsilon_o \frac{4V_{in}}{a} \sum_{n=\text{odd}} \frac{\sin(\frac{n\pi x}{a})}{\sinh(\frac{n\pi b}{a})} \quad (2.18)$$

Second, the total charge is the integral of the distribution in Equation (2.18) taken over the surface in Figure 2-12 from $x = \frac{a}{10}$ to $x = \frac{9a}{10}$:

$$Q_{1_2} = \int_{\text{bottom electrode}} \rho_s dS \quad (2.19)$$

$$= -\frac{4V_{in}w}{\pi} \sum_{n=\text{odd}} \frac{\cos \frac{n\pi}{10} - \cos \frac{9n\pi}{10}}{n \sinh(\frac{n\pi b}{a})} \quad (2.20)$$

Step 3 is the final step, the charge calculation. The ratio between the induced

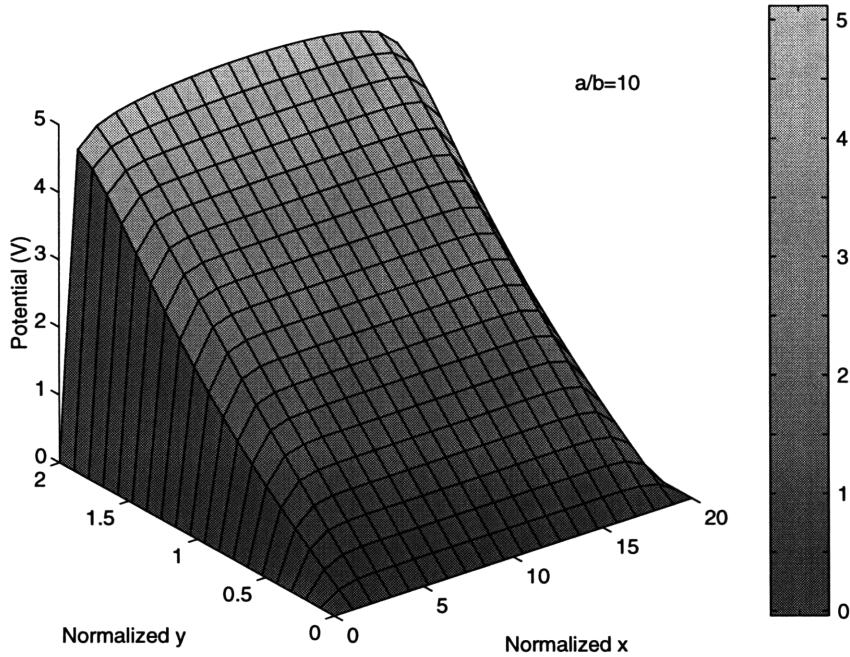


Figure 2-9: Potential distribution inside a rectangular conducting tube with $a = 10b$.

charge and the potential difference is,

$$C_{12} = -\frac{4w}{\pi} \sum_{n=\text{odd}} \frac{\cos \frac{n\pi}{10} - \cos \frac{9n\pi}{10}}{n \sinh\left(\frac{n\pi b}{a}\right)} \quad (2.21)$$

A plot of the normalized capacitance per unit width (measured into the page) is shown in Figure 2-13 for varying $\frac{b}{a}$. Note that the theoretical capacitance rapidly converges to the parallel-plate capacitance as a becomes larger. For $a = 20b$ the two values are within one part in a thousand of one another. If the region from $x = \frac{a}{5}$ to $x = \frac{4a}{5}$ is used instead to compute the mutual capacitance, the agreement improves exponentially to within one part per million (1 ppm).

Other researchers have formulated rigorous proofs of this exponential dependence. For instance, Heerens showed that the edge effects in a capacitance sensor decrease exponentially with the ratio $\frac{a}{b}$. [15] The design objective is to eliminate edge effects by using small gaps, b , with relatively large electrodes, a . Chapter 3 uses this principle to design the HCLPM.

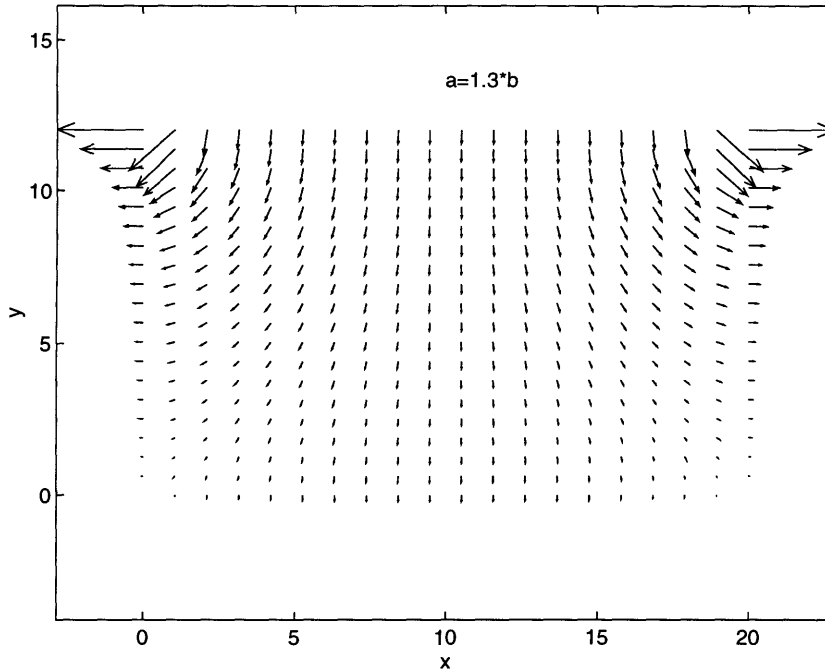


Figure 2-10: Electric Field Vector Map Inside a Rectangular Conducting Tube with $a = 1.3b$.

2.3.3 Extending the spatial solution domain

A simple periodic replication of the electrode configuration in Section 2.3.2 is shown in Figure 2-14. The practical reasons for extending the domain include the ability to use spatial averaging and an increase in the measurement range. The averaging technique was introduced in Section 1.1.4, Figure 1-5 as a means to minimize the errors in the output that are due to minute structural flaws. Multiple measurements are taken at many different points along the face of the sensor, and then are averaged to obscure the defects in the sensor. In a high resolution position sensor, these defects should be filtered from the measurement.

The increase in measurement range that accompanies the extension is key to designing a long range position sensor. As the length of the ruler, or scale, increases, the range also increases. Spatial averaging and an increase in the measurement range are built into the HCLPM design.

Analytical techniques are intuitively important in capacitance sensor design, but when the cavity geometry becomes more complex, numerical techniques are used

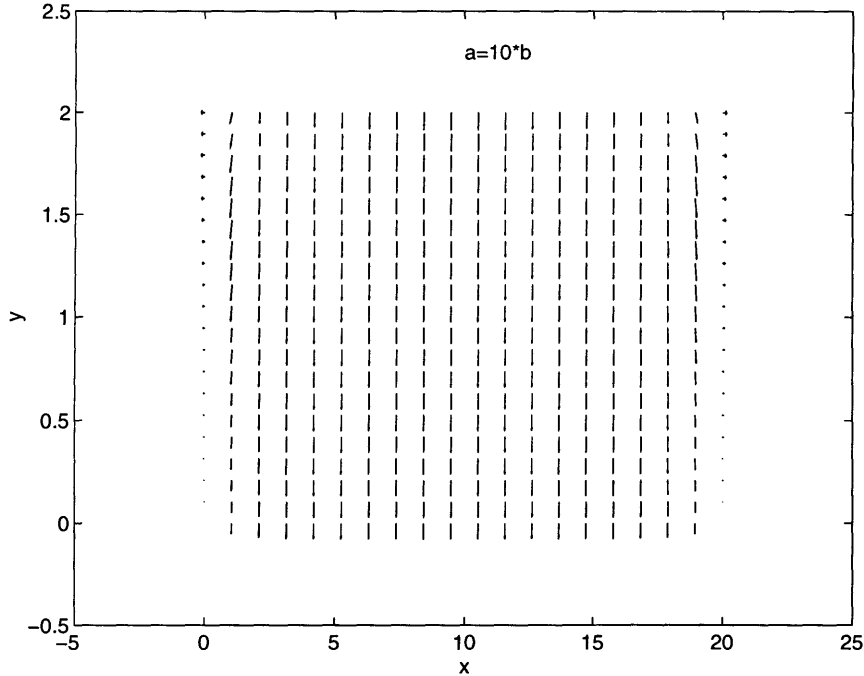


Figure 2-11: Electric field vector map inside a rectangular conducting tube with $a = 10b$.

instead. The extended cavity in Figure 2-14 is precisely the kind of domain which is suited to numerical analysis. The finite difference approximation to the Laplace equation can be written for each grid point (i, j) within the volume as follows [23]:

$$-4u_{i,j} + u_{i-1,j} + u_{i,j-1} + u_{i+1,j} + u_{i,j+1} = 0 \quad (2.22)$$

The interpretation of Equation (2.22) is simple: the potential, $u_{i,j}$, at every point is just the average potential of the four neighboring points. Figure 2-15 is the numerical solution for the full 1000 point grid (refer to Section A.2 for the Matlab script). A close-up of two so called "active" and "non-active" sensing regions is shown in Figure 2-16. The non-active region is from $x = 4$ to $x = 8$, and produces very little induced charge distribution on the bottom electrode, hence the name non-active region. The active sensing region is from $x = 8$ to $x = 12$, and has a relatively large induced charge Q , hence the name active region. Optimum electrode configurations produce distinct regions, where the electric field is either small (non-active) or large (active). A capacitance calculation shows that Q is approximately $C_{1-2}V_{in}$, where C_{1-2} is the

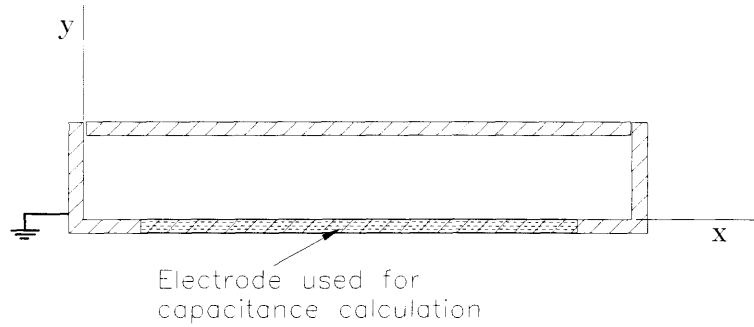


Figure 2-12: Region of the bottom electrode in the rectangular conducting tube used in the capacitance calculation

parallel-plate capacitance in Equation (2.14). This justifies the argument in Section 2.3.2 that the electrode edges have little effect on the bulk region of the capacitor when the length is much larger than the height of the cavity (i.e. $\frac{a}{b} \gg 1$).

The electric field vector map is shown in Figure 2-17. It also clearly indicates that the field is uniform and parallel in the bulk of the active region. This is further evidence that the parallel-plate capacitance, C_{1-2} , between the upper electrode and the active region in the bottom electrode is a reasonable approximation of the true capacitance.

2.3.4 Effects of finite width dimension

The solutions in the previous sections assumed that the width, w , was much larger than the length and the gap. When this assumption is not true, the three-dimensional field inside the cavity is distorted near the edges, and the actual capacitance is larger than the calculated value in the two-dimensional solution. In most capacitance-based lateral position sensors, the width is much larger than either the gap or the length; therefore, the fringing fields in the third-dimension are small and the two-dimensional approximation is accurate enough.

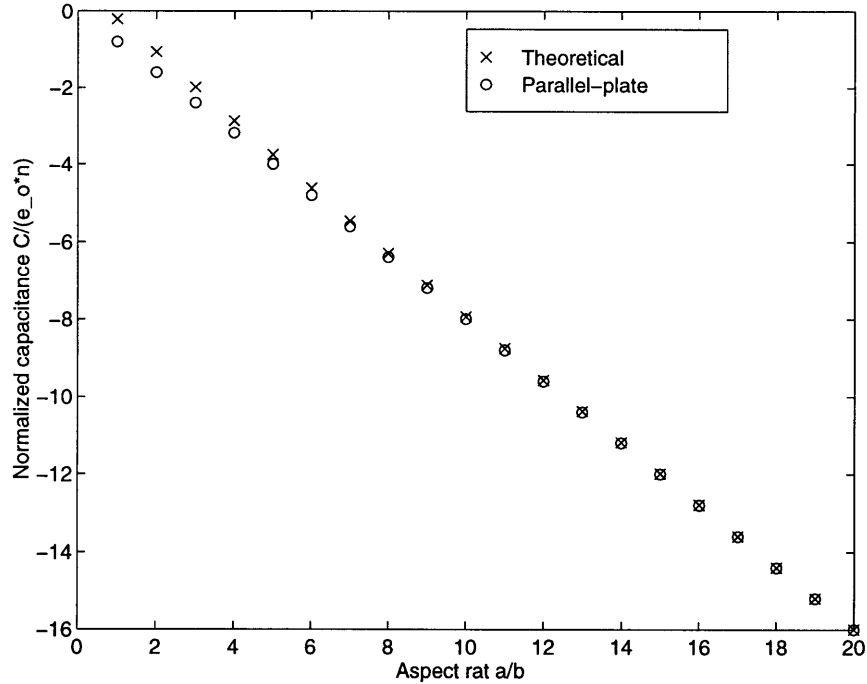


Figure 2-13: Normalized capacitance as a function of the aspect ratio $\frac{b}{a}$

2.3.5 Dependence of capacitance on geometry

It is clear from the formulae in the previous sections that C is independent of the field strength or the amount of charge on the conductors. Furthermore, geometry completely determines the capacitance in any configuration of electrodes. When CGS units are used instead of SI units, this fact is explicit in the formula for capacitance (Equation (2.14)): the units of C_{1-2} are cm . Even though the surface distribution of charge may be different for varying voltage or current inputs, the capacitance does

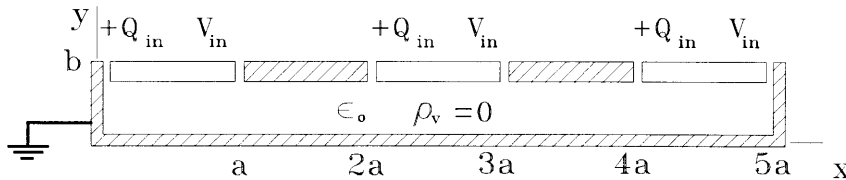


Figure 2-14: Periodic replication and extension of the rectangular tube

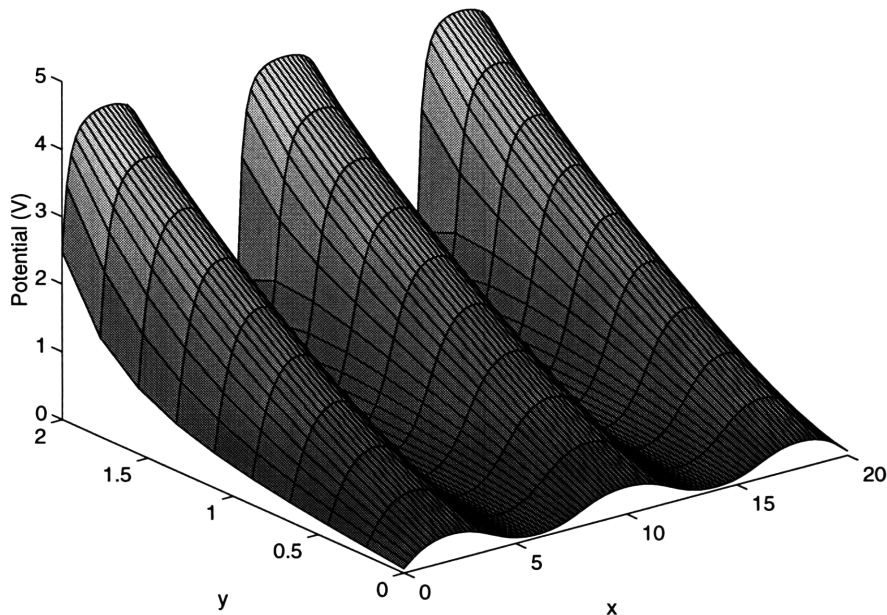


Figure 2-15: Full solution for the 1000 point grid, periodically extended cavity

not change.

The proof of geometrical dependence is taken from the form of Maxwell's equations. Since Equations (2.2) through (2.5) are linear with respect to the field and current sources, the induced charge is proportional to the voltage difference. The only remaining parameter in the problem is the geometry; therefore, it must determine the capacitance. [33]

2.4 Variations in the ideal static capacitance calculation

There are several elements in a capacitance sensor that complicate the formulae in Equations (2.14) and (2.21). Among them are dielectric films, changes in environmental constants, and moving electrodes. Each of these elements can be found in capacitance-based sensors that measure film thicknesses, changes in temperature or pressure, and changes in position. The remaining sections in this chapter summarize the theory of capacitance-based lateral position sensors.

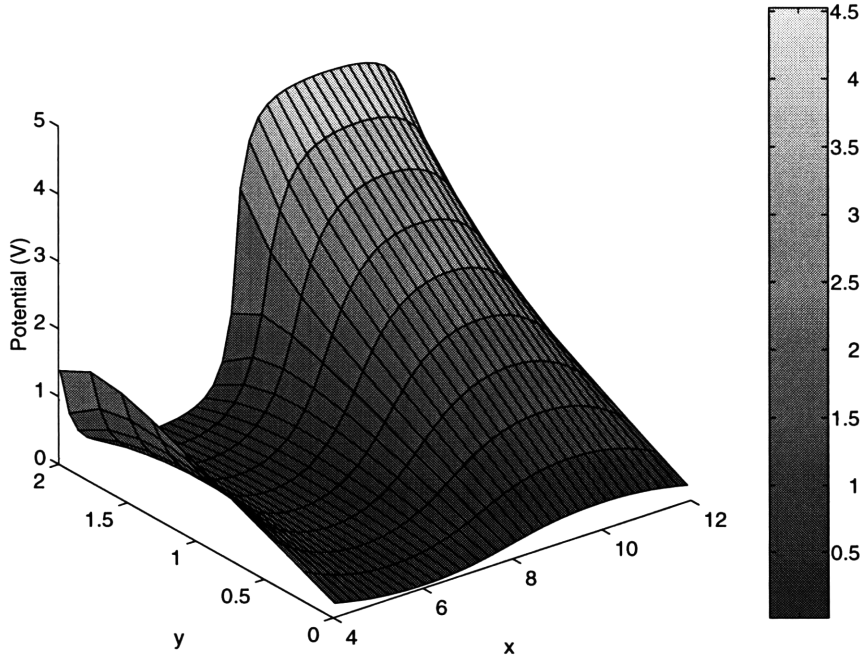


Figure 2-16: Close-Up View of the Active and Non-Active Regions of the Extended Cavity

2.4.1 The sensing problem for moving electrodes

The concepts for the two types of capacitance position sensors, proximity and lateral, were reviewed in Sections 1.1.1 and 1.1.2. The fundamental idea is to associate the change in position with a corresponding change in induced charge or voltage. As two electrodes, which are linked by a mutual capacitance, undergo a change in relative position, the induced charge, or voltage, on the sensing electrode changes. The amount of change is related to the capacitance and the potential difference between the driven and sensing electrodes. Note that the sensing problem begins with the charge and ends with the position measurement. This is different from the capacitance problem, which used the geometry and boundary conditions to compute the capacitance. In this research the capacitance problem is solved to design the sensor, and the sensing problem is solved to operate the sensor.

This research has focused primarily on the lateral changes in position and the associated changes in capacitance. Although the proximity sensor was not a critical element in this research, the sensitivity mismatch between the vertical and lateral

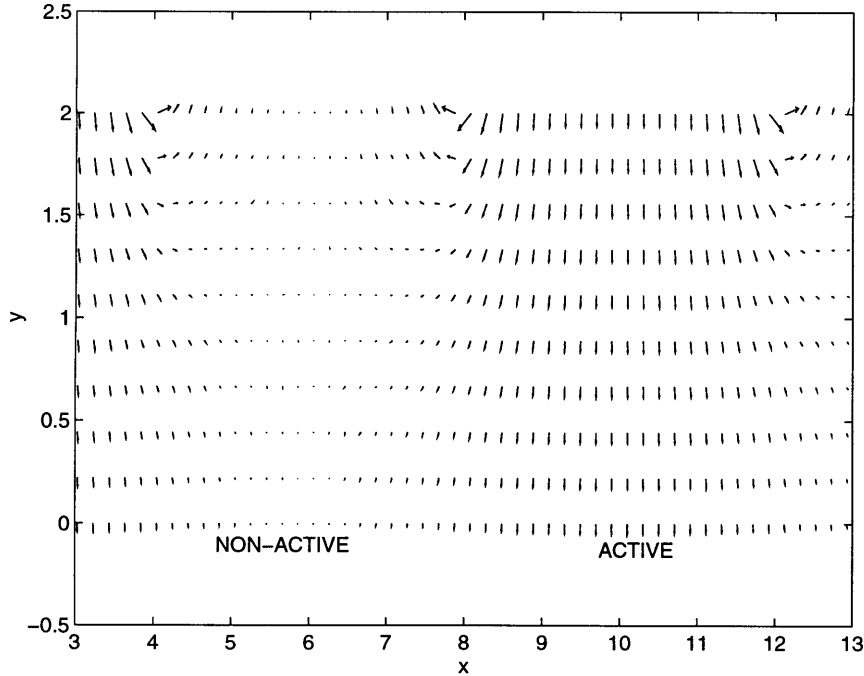


Figure 2-17: Close-Up View of the Electric Field in the Active and Non-Active Regions of the Extended Cavity

sensing modes was critical because it threatened to distort the lateral measurement. Sensitivities of the capacitance sensor to each type of motion are summarized below in Sections 2.4.2 through 2.4.4.

2.4.2 Sensitivity to vertical motions

Sensitivity is defined as the change in the output due to the change in the input. In a capacitance-based position sensor, the input is the change in position and the output is a filtered capacitance. Although the filtering process affects the sensitivity, the ultimate resolution of the sensor is governed by the position-to-capacitance conversion.

Consider the electrode configuration in Figure 2-18. Two parallel-plates, separated by a uniform gap, g , undergo a change in relative position, Δg . The sensitivity, S_v , to the vertical motion is,

$$S_v = \left| \frac{\partial C}{\partial g} \right| = \frac{\epsilon_o A}{g^2} \quad (2.23)$$

Note that the operating sensitivity is set by the initial size of the gap; a factor of

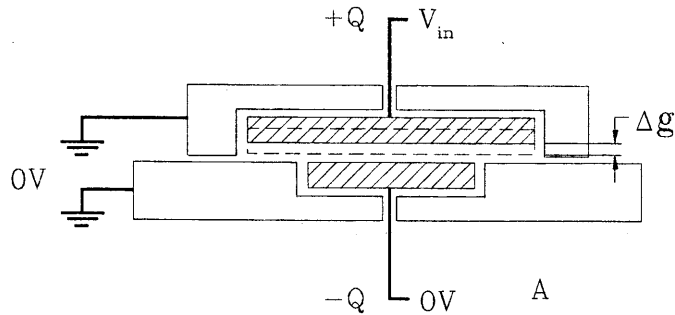


Figure 2-18: Electrode configuration undergoing a change in gap

two decrease in the gap produces a factor of four increase in the sensitivity. Typical operating gaps of 0.1 to 0.5 mm for standard sized probes with $A = 1\text{cm}^2$ give sensitivities on the order of 8.8 to $0.4 \frac{\text{pF}}{\text{mm}}$.

The sensitivity calculation in Equation (2.23) does not account for the changes in the electric field profile as the gap changes. Recall from Section 2.3.2 that both the potential distribution within the cavity and the charge distribution on the electrodes are altered if the $\frac{a}{b}$ aspect ratio is changed. Also recall that in the center of the electrodes, the parallel-plate assumption holds and the field is uniform and parallel throughout the region between the electrodes. Guard electrodes are used to enforce this condition in the proximity sensor.

2.4.3 Sensitivity to tilting motions

The tilting, or rocking, motion can be thought of as a non-uniform gap change across the length of the electrode. Figure 2-19 depicts the tilting mode as a differential gap change, Δg , at opposite ends of the upper electrode. The angular motion $\Delta\phi$ bends the potential distribution and the electric field, which in turn distorts the parallel-plate capacitance (Equation (2.14)). In a first order approximation for small $\Delta\phi$, the electric field remains uniform and parallel; an integration over the bottom electrode

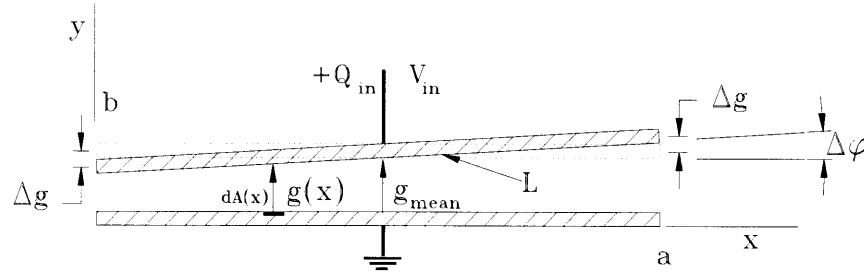


Figure 2-19: Electrode configuration undergoing a tilting motion

yields the capacitance:

$$C_{1-2} = \epsilon_o \int_0^L \frac{w dx}{g(x)} = \epsilon_o \int_{electrode} \frac{w dx}{\Delta\phi x + g_{mean} - \frac{L}{2}\Delta\phi} = \frac{\epsilon_o w}{\Delta\phi} \ln\left(\frac{g_{mean} + \frac{L}{2} \sin \Delta\phi}{g_{mean} - \frac{L}{2} \sin \Delta\phi}\right) \quad (2.24)$$

where g_{mean} is the uniform gap at which the capacitance is C_{mean} with no tilt. Figure 2-20 shows the capacitance variation for tilt angles from -5° to $+5^\circ$ (Matlab script is given in Section A.3). Note that to constrain the percentage variation from the mean capacitance to within 1 ppm (parts per million), the tilt must be kept lower than 0.1° rotation.

The sensitivity of the capacitance to the tilting mode is,

$$S_t = \left| \frac{\partial C}{\partial \phi} \right| = \epsilon_o w \left[\frac{\frac{\phi L g_{mean} \cos \phi}{g_{mean}^2 - \frac{L^2}{4} \sin^2 \phi} - \ln\left(\frac{g_{mean} + \frac{L}{2} \sin \phi}{g_{mean} - \frac{L}{2} \sin \phi}\right)}{\phi^2} \right] \quad (2.25)$$

$$S_t \approx \frac{\epsilon_o w L^3}{6 g_{mean}^3} \phi \quad (2.26)$$

Figure 2-21 is a plot of Equation (2.25) and the linear least squares small angle approximation, Equation (2.26). For a mean capacitance of $0.12 pF$, the sensitivity to tilt is $2 \frac{pF}{deg}$. Since the sensitivity to the proximity mode is large, and the tilting motion is just a differential version of the proximity motion, the sensitivity to the tilting mode is also large. As a result, the angle must be maintained to within 0.01° to sustain a 1 ppm resolution measurement. The HCLPM is designed to meet this requirement.

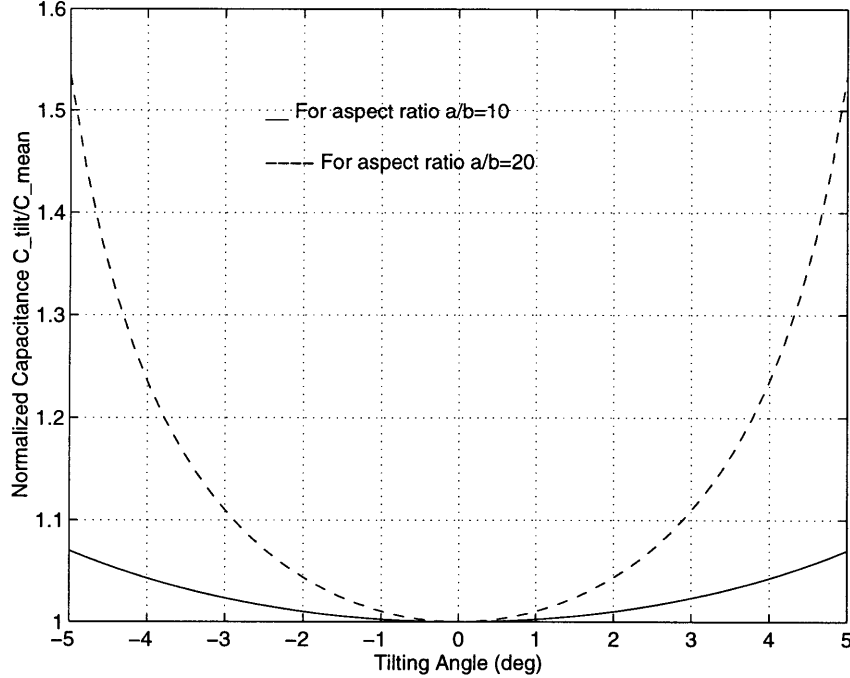


Figure 2-20: Capacitance between a pair of tilting electrodes for varying angles

2.4.4 Sensitivity to changes in lateral position

The subject of this research is lateral position sensing. An example of one-dimensional lateral relative motion of a periodic electrode configuration is shown in Figure 2-22. As the upper driven electrode array moves Δx relative to the lower sensing electrode, the effective area of overlap between the two face-to-face parallel electrodes changes. This variation in area appears as a variation in the measured capacitance. The sensitivity of this configuration to lateral changes in position is,

$$S_l = \left| \frac{\partial C}{\partial x} \right| = \frac{\epsilon_o w}{g} \quad (2.27)$$

A sensitivity comparison between the lateral mode and the other modes of displacement reveals the challenge in the sensing problem. If a sensor is only somewhat sensitive to the lateral mode, but extremely sensitive to the other modes, then it is difficult to resolve small increments in lateral position; the other modes dominate the sensor output response. The design must either constrain the unwanted motions or boost the lateral sensitivity, while lowering the other sensitivities. This point is

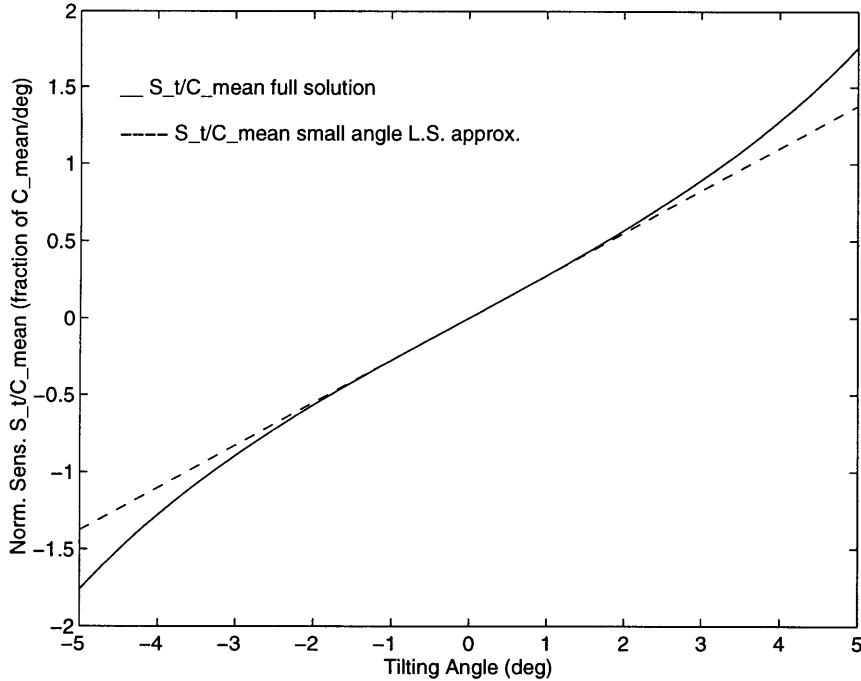


Figure 2-21: Sensitivity of an electrode configuration to tilting motions

discussed further in Chapter 3.

Sensitivity ratios for the different modes are given below in Table 2.2. The largest discrepancy is between the vertical and lateral sensitivities. S_v varies with $\frac{1}{g^2}$, whereas S_l varies with $\frac{1}{g}$; consequently, the vertical sensitivity is higher than the lateral sensitivity. The L in the numerator provides a mechanism for reducing the ratio; a decrease in the length of the electrode will reduce the vertical sensitivity enough to make high resolution lateral measurements possible. Similar comments hold for the ratio of the tilting and lateral sensitivities. High resolution lateral position sensors should exploit the design characteristics that improve sensitivity: small operating gap, large width, small length, and small tilting angle. However, the design must also strike a balance between higher lateral sensitivities and the accompanying higher cross-sensitivities. The general rules are listed in Table 2.2.

Figures 2-23 and 2-24 show the plots of the ratios in Table 2.2 for varying mean gap (script is given in Section A.4). Both plots also show how the electrode length affects the relevant sensitivity ratios. As L becomes smaller, the vertical and tilting sensitivities approach the relatively lower lateral sensitivity. It is also clear from the

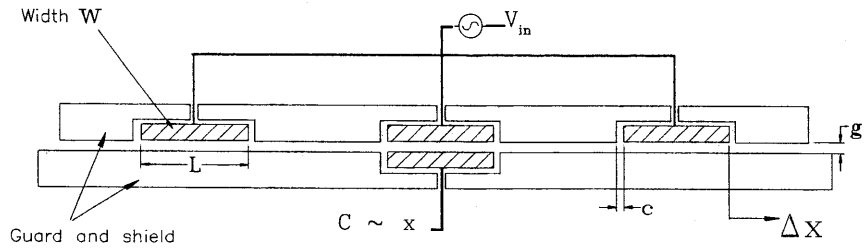


Figure 2-22: Electrode configuration undergoing a lateral motion

Sensitivity Ratio	Value	General Comments
$\frac{S_v}{S_t}$	$\frac{L}{g}$	Decrease in g increases the sensitivity difference; decrease in L (electrode size) decreases the difference.
$\frac{S_t}{LS_t}$	$\frac{L^2\phi}{6g_{mean}^2}$	Decrease in g increases the sensitivity difference; decrease in ϕ (tilt) or L (electrode size) decreases the difference.
$\frac{S_r}{wS_t}$	$\frac{1}{4}$	Ratio is constant for small ϕ and large $\frac{w}{L}$.

Table 2.2: Sensitivity ratios for operating modes in capacitance-based sensing

ratios that the discrepancy between the larger vertical and tilting sensitivities grows as the operating gap decreases. The HCLPM design is founded on these concepts and general rules.

Sensitivity to in-plane rotations

The tilting mode was characterized in Section 2.4.3 as a differential gap change across the length of the electrode. This type of motion is also commonly referred to as out-of-plane rotation. In-plane rotations like the one shown in Figure 2-25 can also take place during a change in lateral position. The upper electrode moves laterally at a

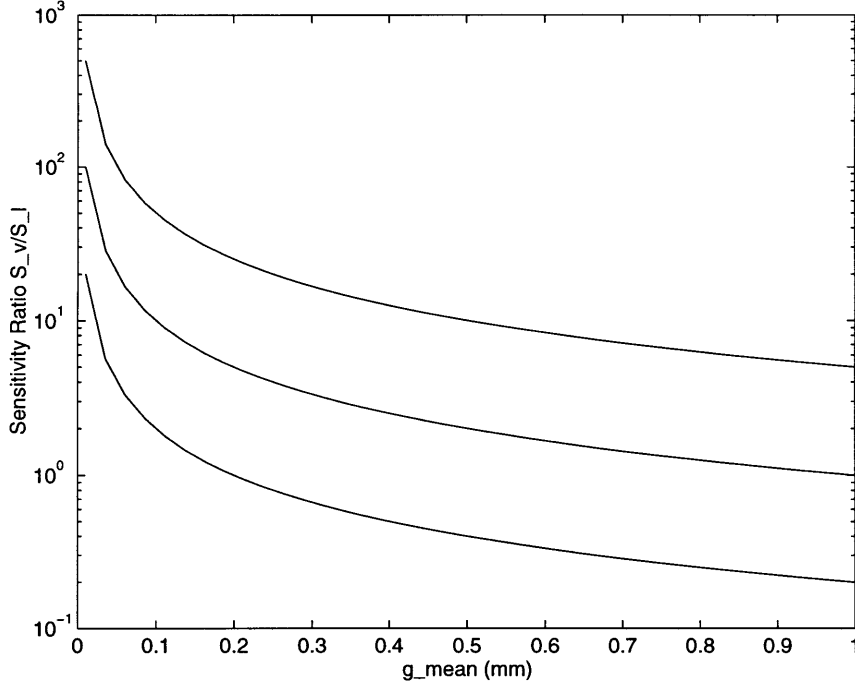


Figure 2-23: Ratio of the sensitivities for the vertical and lateral sensing modes

fixed angle ϕ relative to the lower electrode. As the electrode configuration passes through the point of maximum overlapping area, a small portion of the area along the outer edge of the upper electrode is lost. In effect the area of overlap in the parallel-plate capacitance calculation is reduced from $A = wL$ to $A' = A - A_{loss} = A - \frac{1}{4}\phi w^2$. The total maximum capacitance is,

$$C_{1-2} = \frac{\epsilon_o(\phi w)(w)}{4g} \quad (2.28)$$

The reduction in area reduces the amplitude of the capacitance change in a long range lateral position sensor. Section 2.4.5 discusses this point further.

The sensitivity ratio between the in-plane rotation and the lateral sensing modes is listed in Table 2.2. Note that the width dimension has been used to normalize the in-plane rotation sensitivity. Although the lateral sensitivity is larger by a factor of 4, the tilting mode is large enough to cloud a high resolution measurement. The HCLPM is designed to minimize in-plane rotations as much as possible.

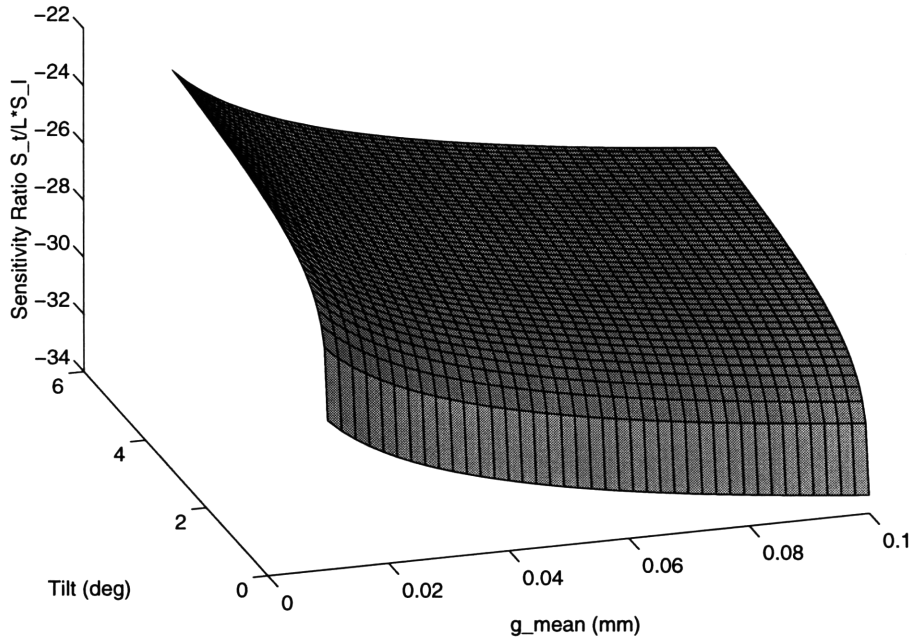


Figure 2-24: Ratio of the sensitivities for the tilting and lateral sensing modes

2.4.5 Linear output for lateral changes in position

The relationship between lateral position and capacitance is linear if the fringing fields around the edges are minimized. Recall that Section 2.2.4 used high aspect ratio electrode configurations to suppress fringing fields. For length-to-gap ratios of 20 or more, the fringing fields were shown to be negligible. Under the assumption of high aspect ratios, the capacitance simply oscillates between the maximum and minimum values, $\frac{\epsilon_0 L w}{g}$ and $0F$, respectively. Figure 2-26 is a normalized illustration of the ideal capacitance at the sensing electrode in Figure 2-22 as the lateral position of the driven electrode array changes. This is the optimum response with no relative in-plane angle between the two electrodes.

Figure 2-27 illustrates the reduction in overlapping area that occurs when there is in-plane rotation, ϕ . By tracing the path of the upper electrode, the minimum area is found to increase and the maximum area is found to decrease. The capacitance profile in this case is shown in Figure 2-28 for three different in-plane rotation angles. The solid line indicates the profile for zero rotation. The presence of any in-plane rotation simply attenuates the modulation amplitude of the profile.

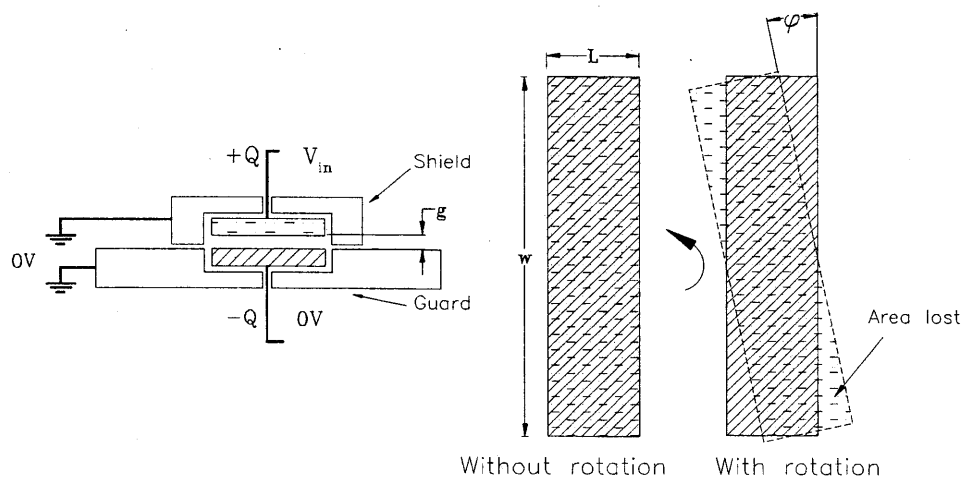


Figure 2-25: In-plane electrode rotation during a lateral motion

2.4.6 Dielectric Media

The dielectric media in a capacitance sensor determines the ease with which charge is transferred from one electrode to the other electrode. One possible difficulty with these materials is dielectric breakdown: the flow of current through a dielectric material for large voltage drops. Breakdown occurs when free electrons are liberated from the bulk material by a high electric field strength, only to collide with the lattice structure. The breakdown strength of several insulators is given below in Table 2.3. Note that this data is for electrostatic fields. When operating frequencies are high, the dielectric strength is significantly reduced. Air is the most often used dielectric because its properties are usually well known.

Material	Relative Permittivity	Breakdown E Field ($10^6 \frac{V}{m}$)
Air	1.0	3
Oil	2.3	15
Paper	1.5-4.0	15
Polystyrene	2.7	20
Glass	6.0	30
Mica	6.0	200

Table 2.3: Dielectric electric field breakdown strengths

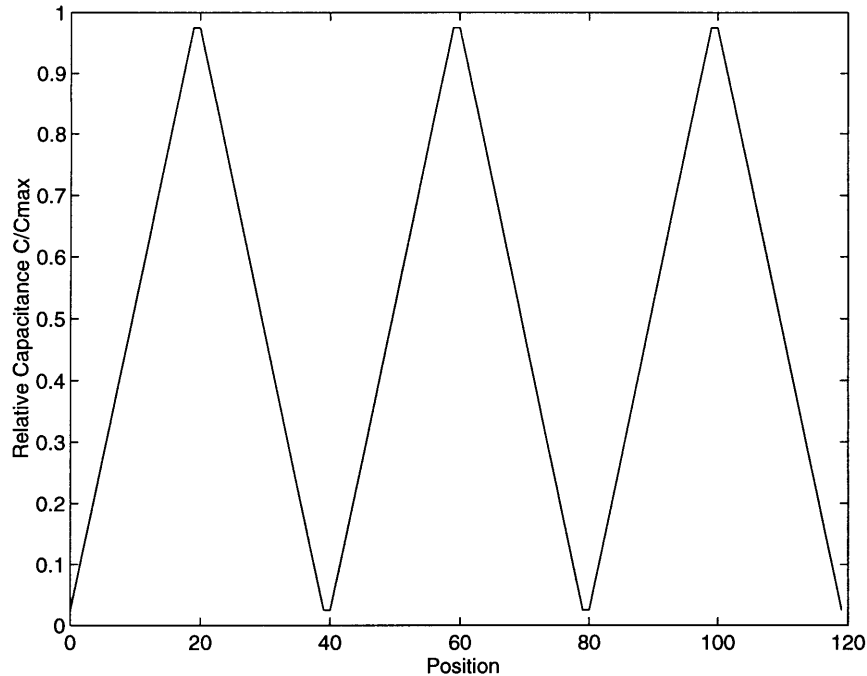


Figure 2-26: Illustration of the piecewise linear output oscillation for lateral changes in position

The values in Table 2.3 are only for the most general class of systems. One notable exception is the lightning rod effect. Section 2.2.4 demonstrated that the electric field distribution near sharp corners or edges is more dense. The substantial increase in the electric field at these locations may be large enough to lower the threshold of dielectric breakdown; this is known as the lightning rod effect. Field strengths should be kept low relative to the size of the electrodes and the operating gap in order to avoid breakdown.

Dielectric imperfection is also a possible drawback of these materials. There are no perfect dielectrics; thus, there are always losses within the intervening media between capacitor electrodes. These losses translate into a current-voltage phase shift other than 90° . In sensing schemes which use the current to sense changes in capacitance, detection becomes very difficult if the phase shift differs greatly from 90° . If current is the measured variable, then the dielectric material must be of the highest quality to avoid large phase shifts.

A third effect of dielectric thin films is the slight increase in capacitance that

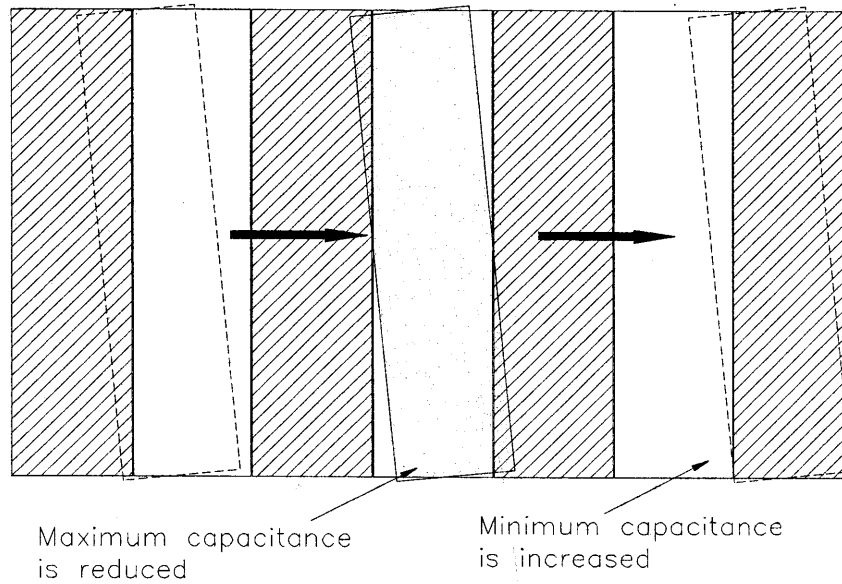


Figure 2-27: Illustration of the change in area due to an in-plane rotation during a lateral motion

occurs. Passivation layers simply create two capacitances in series; the equivalent parallel-plate capacitance is,

$$C_{1-2} = \frac{\epsilon_0 A}{\frac{h}{\epsilon_r} + g} \quad (2.29)$$

where h is the thickness of the layer and ϵ_r is the relative permittivity of the layer. Since ϵ_r is greater than one, the capacitance is larger with the passivation layer than without it. This does not create a problem unless water vapor condenses around sharp asperities in the passivation surface. The condensed moisture is charged and discharged, which distorts both the electric field and the capacitance measurement of the sensor.

2.4.7 Environmental drift

Variations in the environmental temperature, pressure or humidity can severely distort the capacitance estimate of a lateral position sensor. Temperature coefficients for air of $7 \times 10^{-4} \frac{\text{parts}}{^\circ\text{C}}$, humidity coefficients of 7×10^{-5} parts, and pressure coefficients of

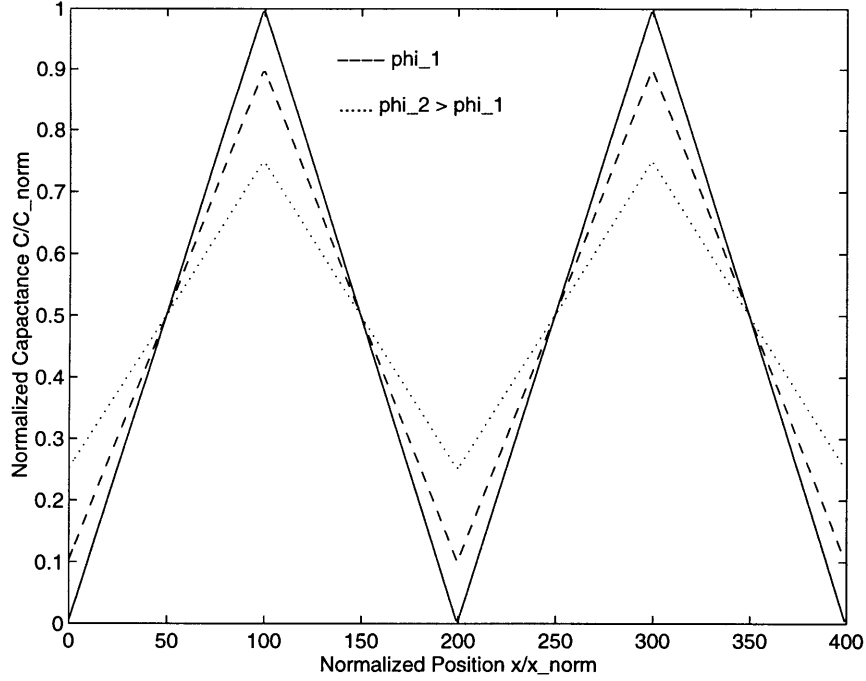


Figure 2-28: Illustration of the piecewise linear output oscillation for lateral changes in position with constant in-plane rotation

$2 \times 10^{-4} \frac{\text{parts}}{\text{atm}}$ are commonly encountered in sensor applications.[20] These coefficients represent the susceptibility of the sensor to variations in the temperature, humidity, and pressure, respectively. One manifestation of drift is a slowly varying dielectric constant. In this case the capacitance measurement is composed of two parts: the capacitance, C_m , at position x due to the mean dielectric strength, and the capacitance, C_d , due to the drift in dielectric strength. The total measured capacitance for the lateral position sensor is given by C_x :

$$C_x = \frac{(\epsilon_o + \Delta\epsilon_o)A(x)}{g} \quad (2.30)$$

$$= \left(\frac{\epsilon_o}{g}\right)A(x) + \left(\frac{\Delta\epsilon_o}{g}\right)A(x) \quad (2.31)$$

$$= C_m + C_d = C_m(1 + \eta) \quad (2.32)$$

$\Delta\epsilon_o$ symbolizes the fluctuation in dielectric strength. As the lateral relative position of the two electrodes changes in moving from state 1 to state 2, the thermody-

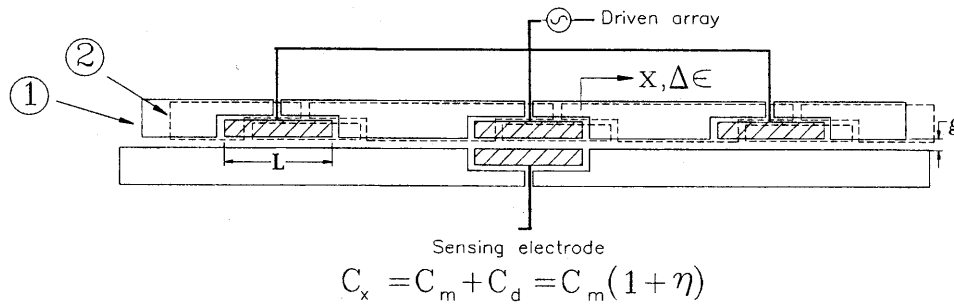


Figure 2-29: Steady drift in dielectric strength during a lateral change in position
 namic state is also free to change (see Figure 2-29). Since the permittivity varies along with the thermodynamic state, the capacitance is contaminated with drift. The ideal measurement would contain only C_m , the part of the capacitance due to the position.

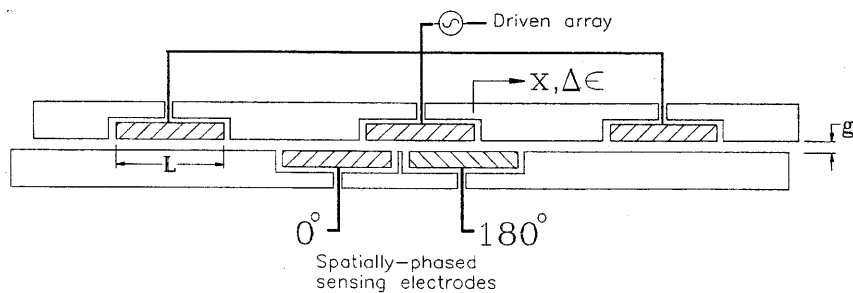


Figure 2-30: Set of spatially-phased electrodes used to decouple the position measurement from the drift component

A single measurement of C_x , by itself, does not contain enough information to decouple the combined capacitance due to both the mean permittivity and the fluctuation in permittivity. Multiple measurements in certain spatial configurations provide the additional information that is needed to sort the two measurements. In particular, consider the system in Figure 2-30 with 0° and 180° spatially positioned electrodes. The normalized capacitance profiles for both of these electrodes are shown in Figure 2-31 over a two period change in position for a ten percent linear change

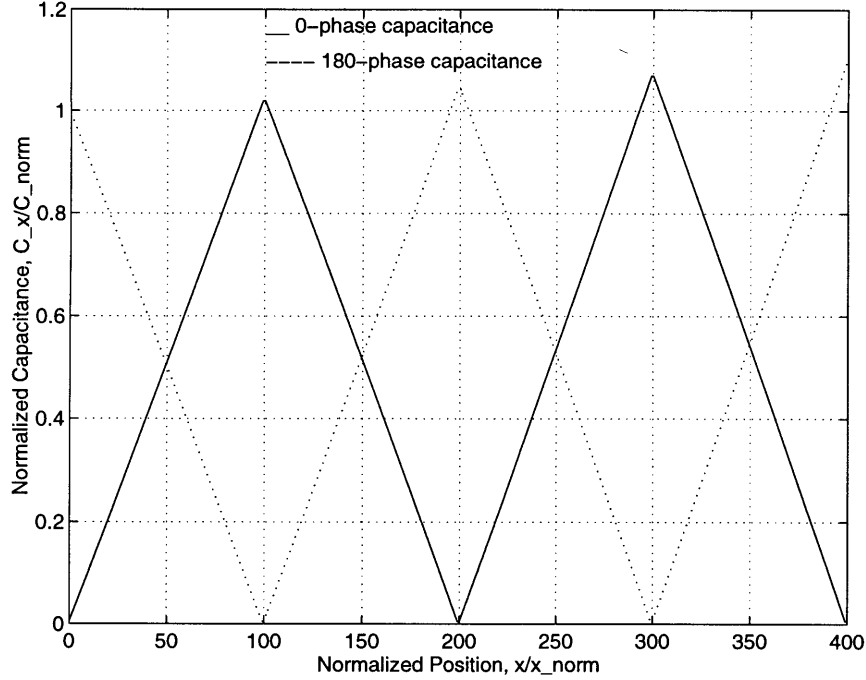


Figure 2-31: Capacitance profiles of 0° and 180° spatially-phased electrodes for changes in position with and without a drift component

in the permittivity. Note that each of the profiles has a component of drift which stretches the graph upward in the direction of the permittivity fluctuation. The goal is to combine the two profiles in a way that preserves the position information, yet suppresses the drift.

In order to treat the problem analytically, the discussion is limited to the piecewise continuous region in the profile from $\frac{x}{x_{norm}} = 0$ to $\frac{x}{x_{norm}} = 100$. For this range of x , the expressions for the normalized capacitance at the two electrodes are:

$$C_0(x) = C_{m0}(1 + \eta) = \frac{\epsilon_o}{g}wx(1 + \eta) \quad (2.33)$$

$$C_{180}(x) = C_{m180}(1 + \eta) = \frac{\epsilon_o}{g}w(L - x)(1 + \eta) \quad (2.34)$$

The first step in the drift compensation technique is to add and subtract the two

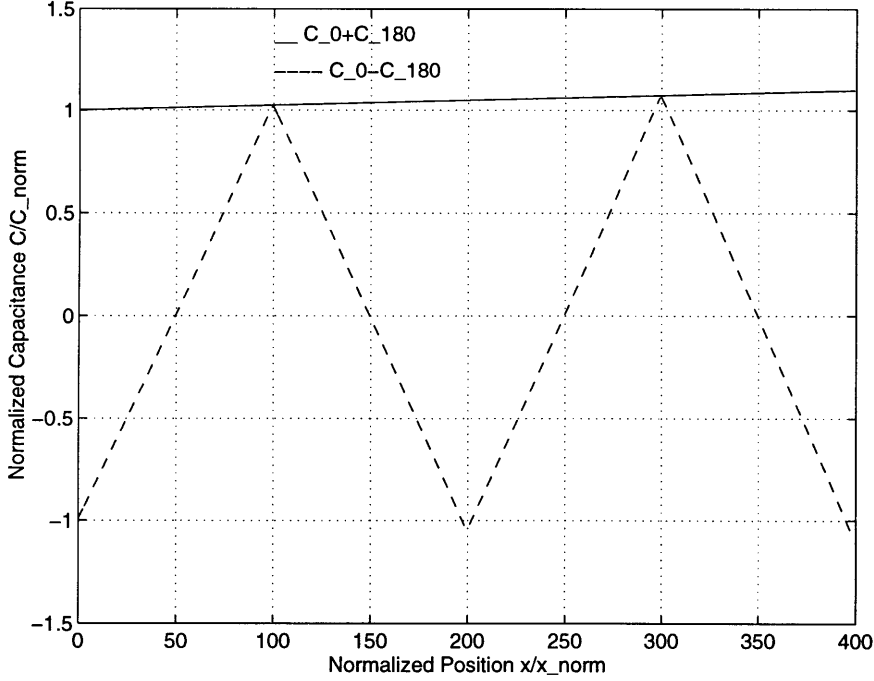


Figure 2-32: Algebraically combined capacitance profiles of 0° and 180° spatially-phased electrodes for changes in position with a drift component

phase responses in Equations (2.33) and (2.34). Basic algebra gives,

$$C_0(x) + C_{180}(x) = \frac{\epsilon_o w L}{g} (1 + \eta) \quad (2.35)$$

$$C_0(x) - C_{180}(x) = \frac{\epsilon_o w}{g} (1 + \eta) (2x - L) \quad (2.36)$$

Note that equation 2.36 filters the common noise inputs to the two different sets of electrodes. This will be used in Section 3.2.5 to attenuate the HCLPM's response to vertical, tilting, and in-plane rotational modes of displacement. The normalized expressions are obtained by dividing both of these quantities by $\frac{\epsilon_o w L}{g}$:

$$(C_0(x) + C_{180}(x))_{norm} = (1 + \eta) \quad (2.37)$$

$$(C_0(x) - C_{180}(x))_{norm} = (1 + \eta) \left(2 \frac{x}{L} - 1\right) \quad (2.38)$$

Figure 2-32 shows the normalized profiles from Equations (2.37) and (2.38) in extended form. The compensation technique relies on the form of Equation (2.37).

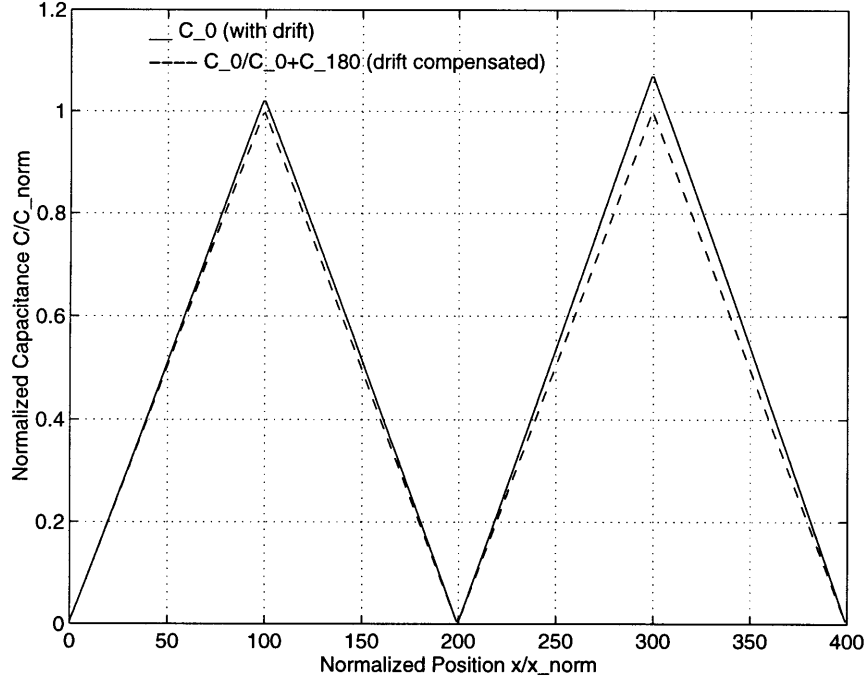


Figure 2-33: Compensation of drift in measurement at 0° spatial electrode through the use of multiple phase measurements

In this normalized expression, the amount of drift, η , is easily obtained. Furthermore, by dividing the contaminated measurement by the sum of the two spatially phased measurements, the component of drift disappears. Equation (2.39) demonstrates the technique and Figure 2-33 illustrates the decontaminated results.

$$\frac{C_0(x)}{C_0(x) + C_{180}(x)} = \frac{\epsilon_o}{g}wx = C_{m0} \quad (2.39)$$

The method in Equation (2.39) is only applicable for electrode configurations that generate differential capacitance profiles (i.e. 180° separation between the two profiles). Once the configuration is chosen, any "common mode", or disturbance, that affects both of the capacitance measurements can be rejected with this technique. Although a linear variation in permittivity was used in Figure 2-31 to describe the phenomena of drift, the compensation technique can also be applied to nonlinear variations, in which η is a function of position. The compensation technique for nonlinear drifts works in the following way: each period in the sampled response is processed by Equation (2.39) as if the nonlinear variation were actually a piecewise

continuous, linear subset of variations. In effect, the drift, η , is simply eliminated after each sample.

2.4.8 Differential compensation and modal "noise"

The compensation technique in Section 2.4.7, whereby the 0° and 180° spatially phased electrode groupings were combined to eliminate environmental drift, is a form of differential compensation. Other sources of "noise", which include modal noise, can also be attenuated with this technique. Recall from Section 2.4.4 that the position measurement can be dominated by changes, either translational or rotational, in the other modes of displacement when those changes are substantial. Differential compensation is a filtering mechanism, which extracts the lateral position measurement from an additive measurement with modal noise.

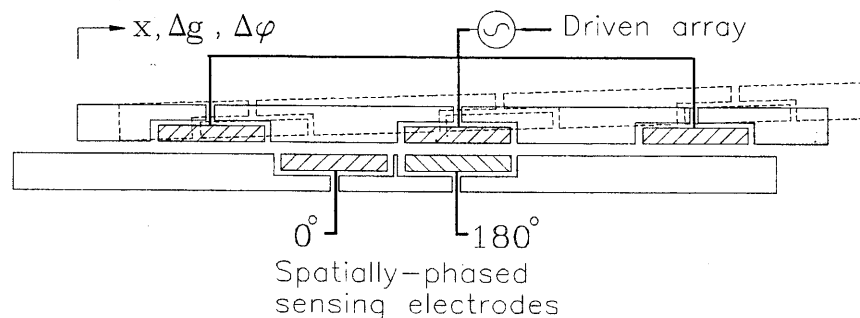


Figure 2-34: Set of spatially-phased electrodes used to attenuate the variation in gap across the sensor

Consider the system in Figure 2-34. In the starting position the 0° phase capacitance is zero and the 180° phase capacitance is a maximum. In the final position the driven array has moved laterally, experienced a change in gap, and undergone a slight tilt. The two different capacitance functions take into account all of these changes:

$$C_0(x) = \frac{\epsilon_o}{g_0(x)} wx \quad (2.40)$$

$$C_{180}(x) = \frac{\epsilon_o}{g_{180}(x)} w(L - x) \quad (2.41)$$

If the 0° and 180° phase electrodes are close together, then $g_0(x) \approx g_{180}(x)$. This assumption is used in Section 3.2.5 to design the differential electrode configuration for the HCLPM.

Before proceeding to filter the measurement with differential compensation, Equations (2.40) and (2.41) need to be re-written in a more amenable form. If the mean operating gap is g and the variation in gap is Δg , then the equations become,

$$C_0(x) = \frac{\epsilon_o}{g + \Delta g} wx \quad (2.42)$$

$$C_{180}(x) = \frac{\epsilon_o}{g + \Delta g} w(L - x) \quad (2.43)$$

Differential compensation is achieved by dividing these expressions by their sum :

$$\frac{C_0(x)}{(C_0(x) + C_{180}(x))} = \frac{x}{L} \quad (2.44)$$

$$\frac{C_{180}(x)}{(C_0(x) + C_{180}(x))} = 1 - \frac{x}{L} \quad (2.45)$$

Equations (2.44), (2.45), and (2.39) show that differential compensation can be used to remove the effects of modal noise and environmental drift.

2.5 Summary of the theory

The main topics in this chapter are listed in Table 2.4. All of these ideas helped to design the HCLPM in Chapter 3. The challenge in going from the theory to the design was to strike a balance between the sensor performance requirements and the limitations of the fabrication process. The last two chapters in the thesis give a detailed account of the design phase and the fabrication process.

Area of theory	General comments
Simplifying approximations	Low frequencies or small structures lead to the Laplace equation.
Near-ideal conductors	Boundary conditions help to visualize the volumetric potential and to define the electric field at the conductor surface.
Electric field map	Shape the field to simplify and linearize the capacitance calculation by minimizing fringing; use to visualize surface charge distributions; emphasizes the principle of total charge conservation and the need for shielding.
Idealized dimensions	Simplifies three-dimensional problems to two-dimensional problems; limits fringing at edges and enhances the properties in the bulk volume by optimizing $\frac{a}{b}$ aspect ratio.
Mutual capacitance calculation	Design for parallel-plate behavior.
Extension of solution domain	Distributed measurements are more accurate with spatial averaging.
Geometry and configuration	Use the complete dependence of C_{1-2} on geometry to design the sensor.
Sensitivity mismatch	Introduces modal coupling, which must be minimized to achieve high resolution measurements.
Dielectric media	Prevent dielectric breakdown by operating with a reasonable gap.
Environmental drift	Drifts in the output capacitance can be attenuated with the compensation technique.

Table 2.4: Summary of theory for capacitance-based lateral position sensor design

Chapter 3

Design

Chapters 1 and 2 presented a few innovative ideas for a High resolution Capacitance-based Lateral Position Microsensor (HCLPM), and introduced the theory of capacitance-based sensing. All that remains is the sensor design, configured for high resolution changes in position over a long range with a linear output and a rapid response. Together, the choice of operating gap, electrode configuration, and sensor package determine the linearity, sensitivity, accuracy, and repeatability of the sensor response. The way in which these critical design choices were made is discussed in this chapter.

3.1 Objectives of the sensor design

Capacitance-based sensors are easier to calibrate and use when the output is linear, as shown in Figure 2-26. Furthermore, Section 2.2 demonstrated that parallel-plate behavior in capacitance sensors is tantamount to output linearity. The goal then is to satisfy the parallel-plate assumptions as closely as possible by decreasing the operating gap. Not only does the linearity of the response improve in this case, but the sensitivity (Section 2.4) and disturbance rejection of the sensor are also enhanced. Higher sensitivities lead directly to higher resolvable changes in position. However, sensitivity mismatch between the lateral sensing mode and the other three modes (vertical, tilting, and in-plane rotation) can make it difficult to distinguish between the various modes (Table 2.2). By carefully controlling the operating gap, the mea-

surement can be filtered so that only the lateral change in position is reflected by the output.

Measurement distortion is also an area of concern. Most high resolution capacitance devices use a conducting enclosure to minimize stray and parasitic coupling fields, because these fields distort the parallel-plate field. In the HCLPM, the sensing electrodes are encased in a planar arrangement of thin conducting layers. This planar enclosure is a disturbance rejection mechanism, which is impenetrable to external fields. High resolution measurements must be free of distortion if they are to indicate small changes in position.

Accuracy and repeatability are most dependent on the fabrication process. Even if the design is completely accurate theoretically, the accuracy of the sensor is only as accurate as the fabrication sequence that is used to make the sensor. For instance, lithography is used to create arrays of lines, or gratings, with extremely high accuracies from period to period across the entire surface of the array. However, since lithography is governed by microscopic statistical behavior, the accuracy is constrained by a distribution function; i.e. the period length is not one-hundred percent accurate. The HCLPM is composed of extended arrays of electrodes that measure the change in lateral position at each electrode. Spatially phased arrays are also used to minimize the effects of manufacturing flaws via spatial averaging.

Environmental drifts in the humidity, temperature, and pressure can also contaminate the capacitance measurement. The proper choice of sensor materials is the best way to minimize the effects of these variations. On-line compensation techniques, such as the method in Section 2.4.7, can also be used to attenuate the drift in the response. The following design objectives summarize the concepts in this section:

- Maintain a small and constant gap to achieve higher sensitivity to the lateral direction of travel, while minimizing the cross sensitivity to other modes of displacement;
- Minimize the drift and other errors brought about by minute flaws in the fabrication process by implementing a multi-phase, extended sensing array;

- Incorporate a shielding enclosure to isolate the sensor from external stray and parasitic electromagnetic fields;
- Select materials with low environmental coefficients and use on-line compensation techniques to attenuate environmental drift.

3.2 Design strategy

The design strategy for the HCLPM use a two step approach: enforce the physical constraints that are associated with capacitance-based sensing, and then achieve the proposed performance objectives. In the first stage of the design, the operating gap was set small enough to sustain a high sensitivity, but large enough to fall short of the breakdown limit in the sensing capacitor. Second, a particular planar configuration of electrodes was chosen, and the relative positions of the interconnects and electrodes were established. Third, the sensing array was constructed to provide high resolution position measurements. In the fourth stage of the design strategy, electrodes were added to the sensor to monitor the other five modes of displacement. The final stage, experimental verification, is currently being planned. It will focus on readying the sensor for experimental testing by assembling a hybrid circuit that is immune to stray capacitances. Each of these design stages are discussed below.

Throughout the discussion, references are made to the sensing and driven electrode elements. These are the two patterns of conductors between which the measurement capacitances are taken. Figure 3-1 illustrates the operation of the two part HCLPM sensor. The Δx position change causes changes in the capacitances between the two arrays of electrodes on the driven and sensing elements. The "driven" array is electrically driven by a voltage V_{in} , and the sensing electrodes are connected to a charge detection circuit, which serves both as a capacitance meter and a position indicator. The primary design issues involve the patterns of electrodes on the two different elements; therefore, this chapter focuses on these elements and not on the electrical circuitry.

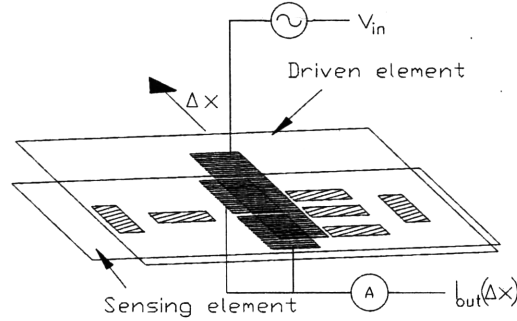


Figure 3-1: Diagram showing motion of the driven electrode element traveling over the sensing electrode element

3.2.1 Selecting the operating gap

Although smaller operating gaps are beneficial in several ways, they can also cause some significant problems. Dielectric breakdown is one such problem that threatens to short circuit the capacitance sensor as the gap decreases. Table 2.3 in Section 2.4.6 listed the breakdown strengths of many different kinds of dielectrics. An air filled capacitor, like the HCLPM, has a minimum gap of,

$$g_{min} = (3.3 \times 10^{-6} \frac{m}{V}) \cdot V = 3.3 \mu m \quad (3.1)$$

below which a current begins to flow. Therefore, the operating gap can be no lower than $16.5 \mu m$ for a $5V$ difference in potential between the two electrodes. $5V$ was selected in this research as the driving voltage because it is a convenient value for most analog-to-digital systems.

Although $16.5 \mu m$ falls within the breakdown limit, particulate matter can cause problems for gaps this small. With this in mind, the gap was increased slightly to $22 \mu m$ to avoid particles that are typically $20 \mu m$ in diameter or less. In the fabrication process (Chapter 4), the gap was made relatively close to the $22 \mu m$ target value.

3.2.2 Design sensitivity

After selecting the operating gap, the sensitivity parameters were chosen to satisfy the resolution requirement. In Equation (2.27), the sensitivity of two parallel plates to a lateral change in relative position was shown to be $S_l = \frac{\epsilon_o w}{g}$. Since the resolution requirement for the HCLPM is $10nm$, the sensitivity was chosen to give a small but detectable change in capacitance for this small change in position. Based on a review of the literature on capacitance detection, $1fF$ was selected as the capacitance change corresponding to the $10nm$ lateral motion. Upon substitution of these values, the width of approach becomes,

$$w_{app} = \frac{1fF}{10nm} \frac{g_{min}}{\epsilon_o} \quad (3.2)$$

The term "width of approach" is a measure of the change in overlapping area for changes in lateral position. Figure 3-2 illustrates the idea; the width dimension of the lateral sensor dictates the sensitivity of the configuration to lateral changes in position. The lightly shaded upper electrodes move relative to the lower electrode. The overlapping area on the bottom electrode is shown for each of the electrode positions. In the first position, there is no overlap; in the second, there is an overlap of $A1$; and in the third position, the overlapping area is $A2$. For the present design, the width of approach must be $25cm$ or more to achieve a sensing resolution of $10nm$. The design meaning of the width of approach is discussed in Section 3.2.3.

3.2.3 Electrode configuration - periodicity

The sensitivity considerations called for an electrode configuration with width of approach, $w = 25cm$, and operating gap, $g = 22\mu m$. Figure 3-3 shows the simplest possible design of this form: a single electrode traveling relative to a second stationary electrode. The upper electrode is wide enough, by itself, to provide the requisite sensitivity to lateral motions. Although this configuration works, it is not well suited to high resolution, high accuracy, long range sensing. The alternative is shown in Figure 3-4. Because multiple electrodes share the sensitivity burden, no one electrode

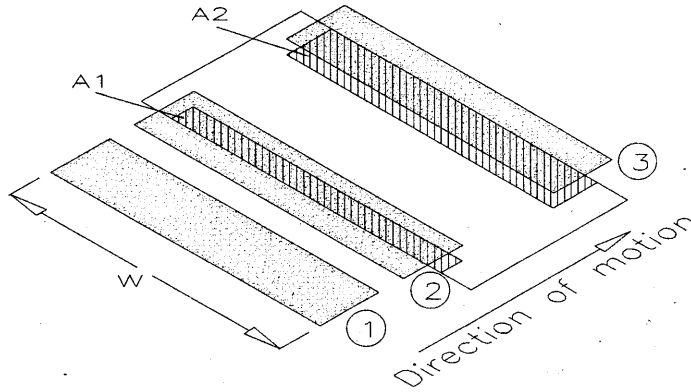


Figure 3-2: Diagram showing motion of the upper electrode relative to the lower electrode with width of approach w

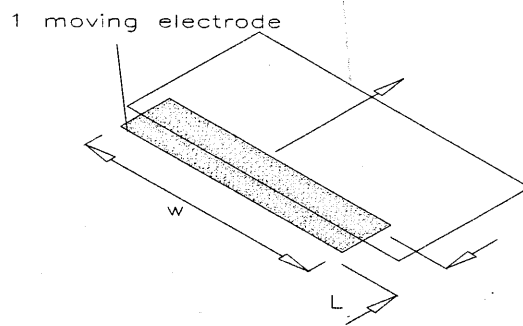


Figure 3-3: Single electrode with width of approach w

is as important as the parallel combination of all the electrodes. The distributed measurement offers several advantages over the single electrode measurement: higher spatial frequency with the attending higher sensitivity and measurement resolution, improved accuracy with a reduction in cross sensitivity to non-lateral modes of displacement, and extended measurement range.

Advantages of distributed measurements

The normalized measurement profiles for the systems in Figures 3-3 and 3-4 are shown in Figure 3-5. For the single electrode configuration, the capacitance grows from zero to a maximum, C_{max} , as the relative lateral position changes from zero to $x_{max} = L$. The sensitivity, or slope, of this profile is $\frac{C_{max}}{L}$. Next, consider the profile for the

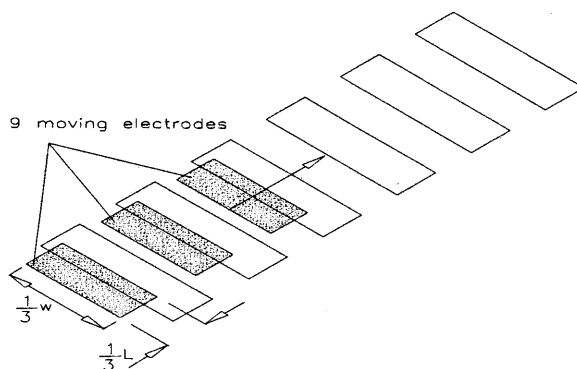


Figure 3-4: Multiple electrodes which distribute the total width of approach w

multiple electrode configuration. Since the capacitance changes from zero to C_{max} every $\frac{1}{3}L$, the sensitivity is larger by a factor of three, thus the achievable measurement resolution is also higher. The distributed measurement requires more fabrication and processing effort than the single electrode measurement, but the advantages are well worth the effort.

In addition to the increase in sensitivity, the accuracy of the distributed measurement is also enhanced. The reason for this improvement is that the cross sensitivities to the other modes of displacement drop substantially when the length and width of the individual electrodes decrease. For example, Section 2.4.3 showed what is intuitively obvious: the sensitivity to tilting motions is smaller for shorter electrodes. This is also true for the vertical mode of displacement (see Table 2.2). As the cross sensitivities decrease, the measurement begins to better reflect the lateral change in position.

Distributed measurements can also be used to extend the measurement range. Section 2.3.3 discussed the solution procedure and benefits of a periodically replicated, or extended, electrode configuration. Pattern replication is the same as increasing the length of the ruler. As shown in Figure 3-4, the distributed measurement is accomplished by adding more electrodes. Each additional electrode in the stationary array increases the linear range of the sensor.

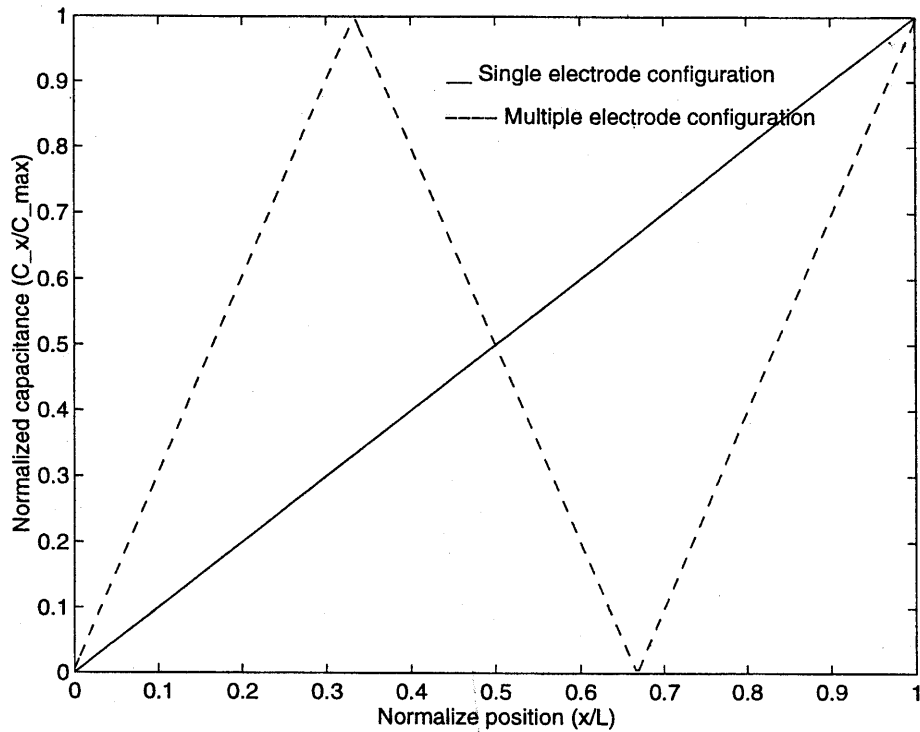


Figure 3-5: Capacitance profile for the single and multiple electrode configurations

3.2.4 Electrode configuration - structure

There are three possible electrode structures from which to choose the HCLPM structure. The first type to consider is the three plane structure in Figure 3-6. For one

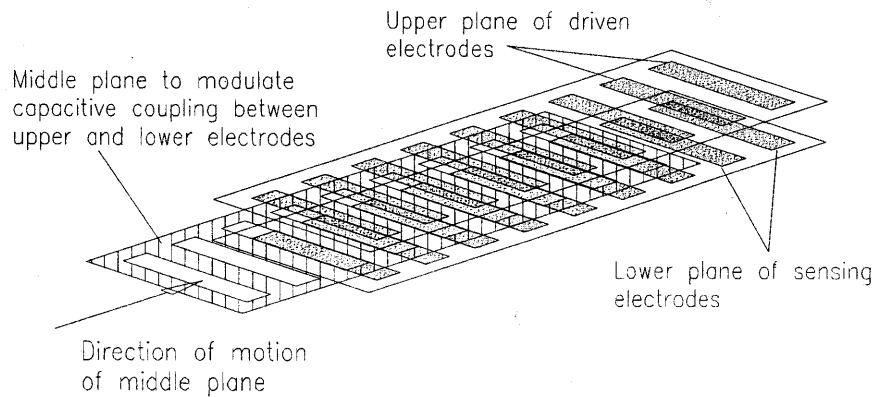


Figure 3-6: Three plane sensor electrode structure

particular choice of sensing circuitry, the center plane is grounded and patterned with slots, which modulate the electrostatic coupling coefficient between the two arrays of electrodes on either side of the center plane. The capacitance between the upper and

lower planes changes as the center plane moves linearly between them. In effect, the slotted center plane acts like a moving shield: in one position, the center plane allows the two outer planes to communicate electrostatically with one another; in a second position, the center plane does not permit communication between the other two electrodes. The primary disadvantage of this design is the difficulty in implementing the three plane configuration. Not only is alignment more of a challenge, but the signal processing issues are more complex as well.

The second type of electrode structure is shown in Figure 3-7. Similar to the Miller design in Figure 1-4, the platten design senses a change in gap as the upper

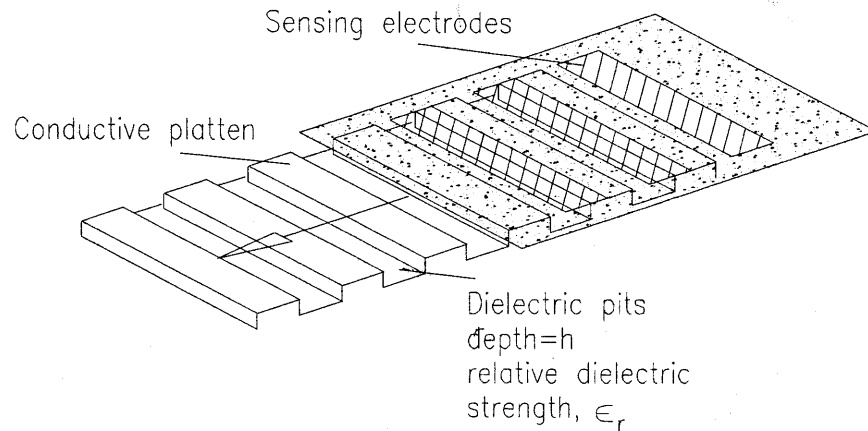


Figure 3-7: Platten sensor electrode structure (Miller)

array moves relative to the platten. Note that although the overlapping area between the platten and the electrode array is constant, the total area is distributed over the hills and valleys of the platten.

The important qualitative characteristic of the capacitance profile is the modulation ratio, the maximum capacitance divided by the minimum capacitance. The maximum capacitance occurs when the upper electrodes are directly above the platten ridges, whereas the minimum capacitance occurs when the electrodes are above the valleys of dielectric filler. After applying Equation (2.29), the modulation ratio

is found to be,

$$\frac{C_{max}}{C_{min}} = 1 + \frac{h}{\epsilon_r g} \quad (3.3)$$

where g is the operating gap, ϵ_r is the dielectric filler relative permittivity, and h is the dielectric filler depth (see Figure 1-4). The first disadvantage of this electrode structure is nonlinear rounding of the characteristic capacitance profile. The rounding effect is brought about because the electric field conforms to the side walls of the platten strips, diffusing into the linear part of the profile, as discussed in Figure 2-10. In other words, the field lines are not straight and do not exhibit parallel-plate behavior. The second disadvantage is the small modulation ratio. The preferred electrode structure has a larger ratio, which is limited only by the stray capacitances in the system.

The preferred electrode structure is shown in Figure 3-8. This design is similar

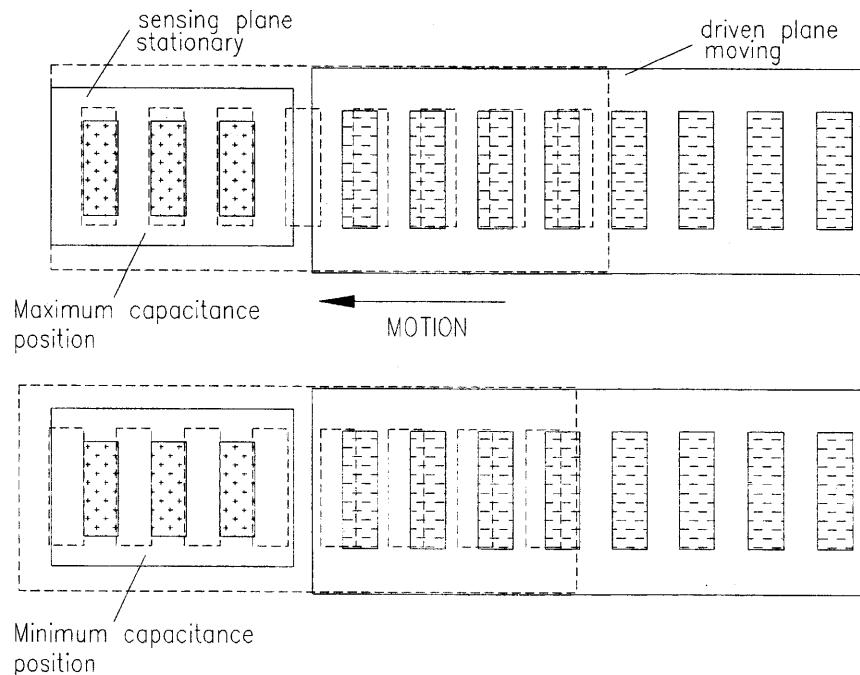


Figure 3-8: Preferred sensor electrode structure

to that of Heerens (Figure 1-3) in that there are two planes of electrodes, the driven and the sensing elements. As the driven element moves laterally above the sensing element, the two arrays of electrodes couple electrostatically to one another. The differences between this structure and the others are its relatively large modulation ratio, high degree of linearity, and simpler construction. The modulation ratio is larger than in the previous two designs because the minimum capacitance is approximately zero in this case. The linearity is also better since there are no side walls to which the electric field must conform by bending. Lastly, the structure is easier to build because there are only two planes of electrodes, which can be created in thin-film processing facilities without needing to micromachine the platten or slotted center plane.

3.2.5 Electrode configuration - phasing

Section 2.4.7 discussed a way to compensate for environmental drift by making measurements in different spatial locations. Differential compensation was achieved by adding and subtracting the measurements at the 0° and 180° spatially phased electrodes. Section 2.4.8 described the same technique as it applies to the attenuation of modal noise. In the HCLPM each phased grouping of electrodes contains many small electrodes with a total width of approach w_{app} . Four different spatial phases were needed to attenuate the drift and measure the velocity (direction): 0° , 180° , 90° , and 270° . An additional benefit of taking multiple phase measurements is a doubling of the sensitivity to lateral motions.

The positioning of each phased grouping is shown in Figure 3-9. There are several features to notice in the figure. First, the 0° and 180° electrode groupings are interdigitated; therefore, the environmental drift, noise, and non-lateral displacements are approximately equal for the two groupings. This equality is critical to the application of Equations (2.44) and (2.36), which aim to eliminate the common sources of "noise" in the problem. Variations in the operating gap are the most detrimental sources of contamination because the capacitance is most sensitive to changes in the gap. All sources of noise can be minimized by carrying out the differential compensation technique. The second feature to notice is that the 0° and 180° phased groupings

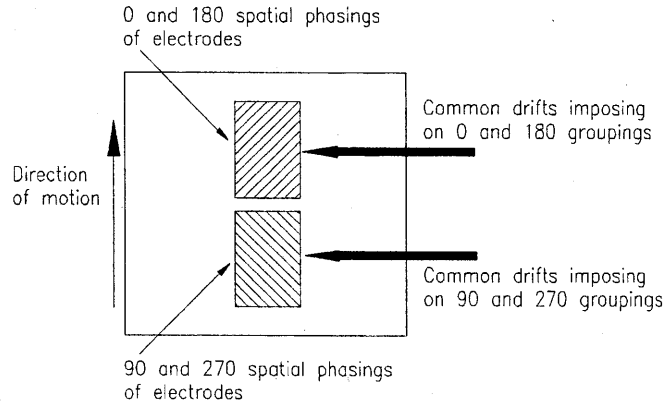


Figure 3-9: Positioning of the spatially phased groupings of electrodes in the HCLPM

are positioned along the line of motion, instead of side by side. This reduces the sensitivity to in-plane rotation of the driven or sensing arrays of electrodes.

3.2.6 Electrode and interconnect spacing

The individual electrodes in the top and bottom arrays in Figure 3-8 must each work individually. The charge on one electrode, or interconnect, in the sensing or driven arrays should be invisible to all of the other electrodes except for the one or two electrodes that are opposite to it in the other plane (see Figure 3-10). In order to isolate the electrodes and interconnects, a planar guard is introduced to block the transfer of signals from one electrode to another. The guard is used to isolate electrodes on the same plane and electrodes on opposite planes from one another. For instance, electrode 2 in the figure should be invisible to electrode 1. The guard layer is most effective when the space between the electrodes, or interconnects, and the guard is small. The HCLPM fabrication process was fine tuned to provide the smallest gaps possible between the guard and the sensing structure ($7\mu m$).

The spacing between the individual electrodes was set in accordance with the exponential rule for the decaying electric field at the edges of the electrodes (refer to Section 2.3.2). Figure 3-11 illustrates the general principle. As the field between the two electrodes ventures outside the center region between the two electrodes,

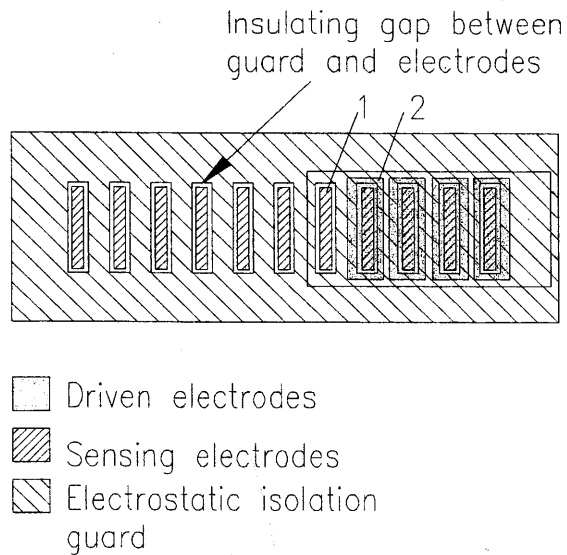


Figure 3-10: Spacing for isolation between electrodes and interconnects in the preferred sensor electrode structure

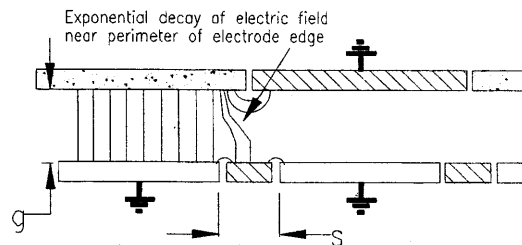


Figure 3-11: Illustration of the exponential decay in electric field around the perimeter of electrode edges in the preferred electrode structure

the intensity of the field drops exponentially with the distance from the edge of the center region. The decay in the evanescent field is more rapid when the operating gap is small. Figure 3-12 shows an example of the design calculation. The amount of exponential decay is chosen to fall below the resolution tolerance of the sensor. For example, two independent electrodes in a sensor with 1 ppm resolution should be placed far enough apart laterally so that $\exp(\frac{-s}{g})$ is less than 1×10^{-6} . The exact spacing for the HCLPM electrode and interconnect structure is given in Section 3.2.7 after having better defined the overall structure.

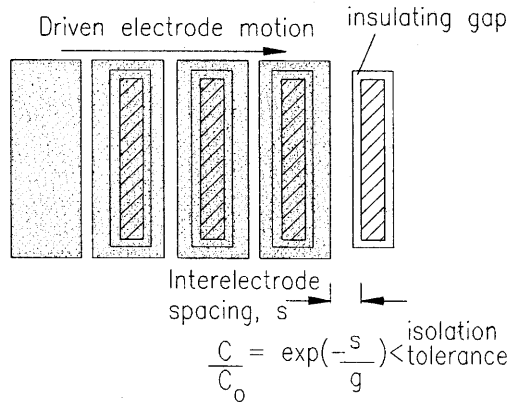


Figure 3-12: Example of the exponential spacing calculation for a small region of the preferred sensor electrode structure

3.2.7 Electrode pattern

The HCLPM electrode pattern was designed to be sensitive to small lateral changes in position, but insensitive to stray fields, environmental drift, and non-lateral modes of displacement. Although there are two different layouts for the sensing and driven planes of electrodes, the design of each plane is similar.

Sensing electrodes

The sensing electrode pattern is shown in Figure 3-13. Each region of the pattern has a different purpose in the overall function: the center region of the pattern is used to sense lateral changes in position; the perimeter electrodes are used to monitor the other modes of displacement, as is explained below; and the remaining regions in the pattern form the interwinding guard electrode. Magnified views of these regions are given in Figures 3-14 and 3-16.

Figure 3-14 shows a small portion of the electrode array in the sensing element. Note that the clear regions in the design indicate electrodes whereas the lines indicate gaps and thin interconnects. In both the driven and sensing electrode patterns, signals are carried to and from the individual electrodes via $4\mu m$ interconnects. A $200\mu m \times 200\mu m$ wire bonding pad is found at the end of every interconnect. The largest of the clear areas in the design indicate guard electrodes, which are electrically grounded

Dimension	Value	Description
w_E	$3.0mm$	Width of electrodes in the lateral position sensing pattern (5 pF total)
	$3.6mm$	Width of electrodes in the lateral position driven pattern (5 pF total)
L_E	$0.2mm$	Length of electrode in the lateral position sensing pattern
	$0.21mm$	Length of electrode in the lateral position driven pattern
w_I	$4\mu m$	Width of interconnects and insulating gaps
w_g	$10\mu m$	Width of intervening guard electrode between sensing electrodes
A_m	$0.11cm^2$	Area of monitor electrodes for $5pF$ capacitance

Table 3.1: Key dimensions in the electrode and interconnect structures in the driven and sensing arrays of the HCLPM

and serve to isolate interconnects and electrodes. The dimensions of the individual electrodes were chosen to satisfy the $10nm$ measurement resolution requirement of the HCLPM. Section 3.2.2 discussed the width of approach and how it relates to measurement resolution and sensor design. Since the width of approach was calculated there ($25cm$), all that remains is to distribute the total width across an entire electrode pattern (recall Section 3.2.3). If the number of electrodes is designated by N , and w_E is the width per electrode, then the following equation must be true:

$$w_{app} = Nw_E \quad (3.4)$$

Before calculating the individual widths, the length of each electrode was chosen to conform with modern standards of signal processing and interpolation. Since the goal was to sense $10nm$ changes in position, and 400 ppm is a reasonable degree of resolution per period [6, 7], the period length was calculated to be $10nm \times 400 = 400\mu m$. Thus the electrodes each have a length of $200\mu m$ and a width of w_E . Note

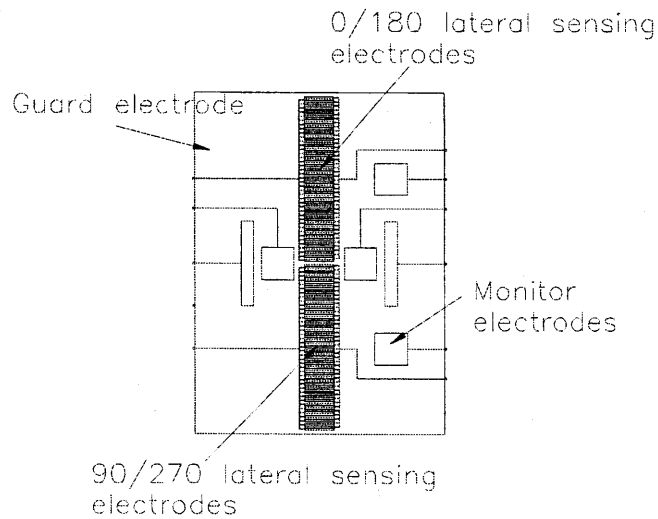


Figure 3-13: Layout of electrodes on the sensing element

that the period of the pattern ($436\mu m$) is actually larger than twice the length of the electrodes ($400\mu m$), due to the intervening gaps and guard electrodes. Figure 3-15 shows a magnified view of these intervening regions. The purpose of the guard electrode between the two sensing electrodes is to isolate them from one another.

N and w_E were found with Equation (3.4) after choosing a maximum capacitance value of $5pF$. This capacitance is the typical value in most high resolution capacitance detection systems. N and w_E were found to be 40 and $3mm$, respectively. Table 3.1 contains a list and description of the design dimensions.

In order to gauge the performance of the sensor during experimental testing, electrodes were added to the design to provide additional measurement degrees of freedom. These "monitor" electrodes are configured to sense rotations about the x, y, and z axes, and translations along the x and z axes. As an example of the operation of the monitor electrodes, consider the *Rot x* monitor electrode pair indicated in Figure 3-16. Note that the arrow with the *Rot x* label points to only one of the monitor electrodes; the second electrode in the pair is symmetrically located about the x axis. As the sensing element of electrodes rotates about the x axis relative to

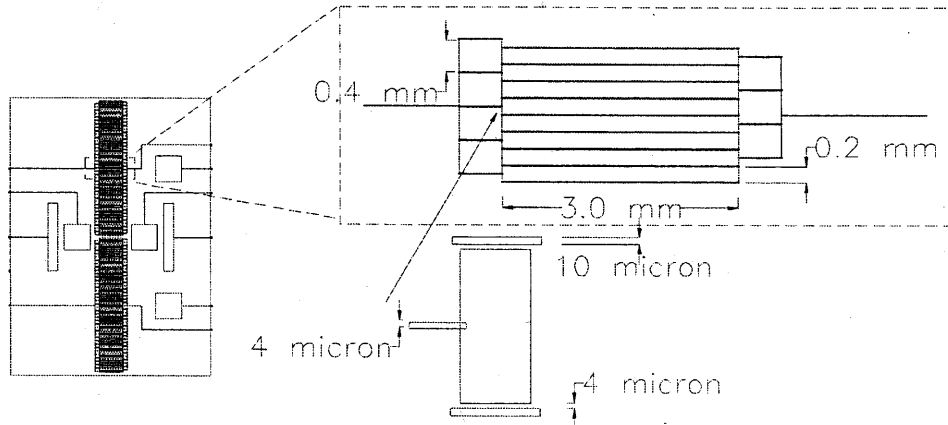


Figure 3-14: Magnified view of the lateral sensing array and interconnect structure

the driven element of electrodes, the differential capacitance change between the two *Rot x* monitor electrodes serves as a measure of the magnitude and direction of the rotation. The other symmetrically located pairs of monitor electrodes operate in a similar way to indicate the other four modes of displacement, which can contaminate the pure *y* translation lateral position measurement.

A magnified view of two monitor electrodes and their dimensions is shown in Figure 3-16. Each monitor electrode is designed with a $5pF$ mean capacitance, a $4\mu m$ insulating gap that separates the electrode from the guard, and a $4\mu m$ interconnect that carries the electrical signals to and from the electrode. Although the areas are the same, the sizes of each monitor electrode pair vary according to the mode of displacement that they sense. It should be noted here that the minimum line width had to be increased to $8\mu m$ in the fabrication process because of processing difficulties (see Section 4.1.5).

As an example of the monitor design, consider the electrodes that sense rotation about the *y* axis. The distance between the two electrodes was chosen large enough to prevent cross-talk between the lateral sensing electrodes in the middle of the pattern and the monitor electrodes. The exponential decay of the electric field was set to 1 ppm in these regions (refer to Figure 3-12). In addition, the sensitivities of the monitor electrode pairs were made large enough to verify that high resolution lateral

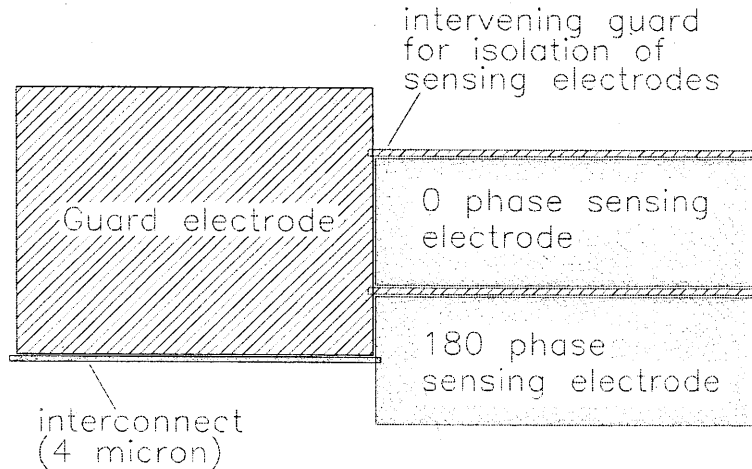


Figure 3-15: Magnified view of the insulating gaps and guard electrode between the sensing electrodes

position measurements were due solely to lateral motions and not to any relatively small non-lateral motions.

Driven electrodes

The driven electrodes were fabricated on a different surface than the one on which the sensing and monitor electrodes were fabricated. The configuration of the driven electrodes was designed to be compatible with the sensing structure. Figure 3-17 shows an overlay of the driven pattern on the sensing pattern from Figure 3-14. The driven electrodes are longer and slightly wider than the sensing electrodes, but they still maintain the same periodicity ($436\mu m$). The larger width was chosen to provide room for exponential decay outside of the sensing region. The longer driven electrodes were designed to sustain parallel plate behavior throughout the sensing cavity between the sensing and driven electrode carriers. Also note that the monitor electrodes in the sensing pattern were positioned opposite to special electrode geometries in the driven pattern.

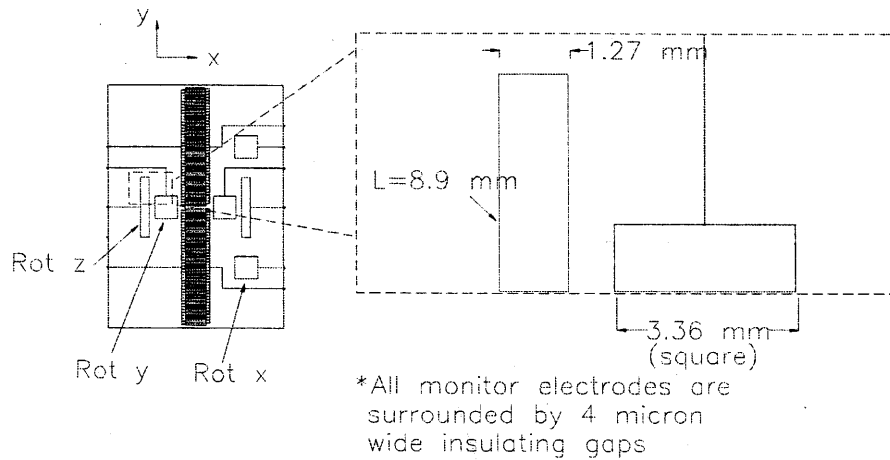


Figure 3-16: Magnified view of the monitor sensing electrodes

3.3 Hybrid sensor design

The driven and sensing elements as described above are the primary elements in the HCLPM design. However, signal processing circuitry must be used to extract the coupled charge information from these elements, which in turn indicates the change in position. The literature on this subject is vast, covering techniques as diverse as capacitance-bridges [20, 17, 19], resonance circuits [32], charge transfer devices [30], and switched-capacitor filters [32, 13, 12]. The difficulty in designing a sensor is not in choosing the circuitry, but instead is concerned with the interface between the macro-world and the microsensor. The most troublesome implementation issues involve the many types of stray capacitance.

3.3.1 Minimizing stray and parasitic capacitances

Section 2.2.4 described stray capacitance in terms of unwanted external electrodes, or surfaces of charge, which contaminate the sensing capacitance measurement. When the external surfaces couple capacitively to either the sensing or driven electrodes, a certain amount of stray charge escapes from the sensing region (Figure 3-18). Note that the back sides of the electrodes are also considered external surfaces of charge. Although the loss of charge can be small, it is large enough to overshadow a small change in capacitance. Shielding is used to isolate the sensor from external con-

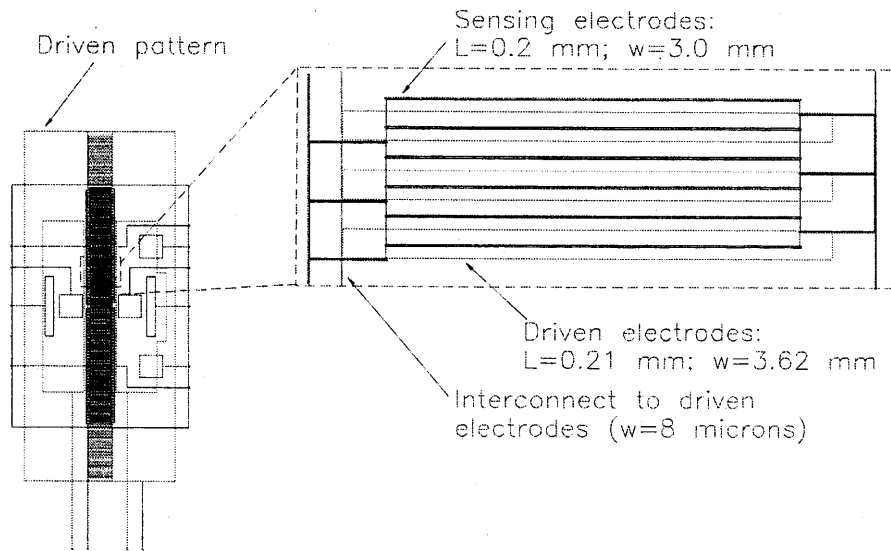


Figure 3-17: Overlay of the driven pattern on top of the sensing pattern - magnified view

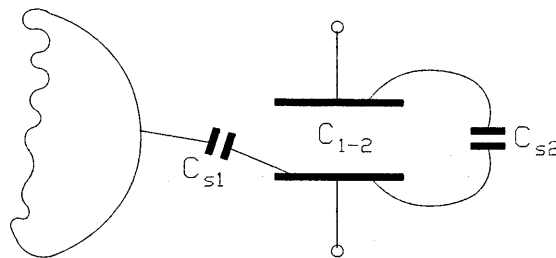


Figure 3-18: Illustration of common stray capacitances to external surfaces

ductors by preventing the loss of charge. Circuitry is then designed to exploit the shielding. The most destructive stray capacitances are parallel to the sensing capacitance; consequently, the strays are additive and they contaminate the measurement. The preferred HCLPM design utilizes an encapsulating shield to isolate the back electrodes from external fields. Although this is easily done using microfabrication (refer to Chapter 4), the additional layer is costly; therefore, the rear shielding arrangement could not be implemented in the prototype sensor.

In addition to external stray capacitances, internal strays are also a potential problem. Interdigitated structures, like the HCLPM, have a tendency towards crosstalk, or capacitive coupling, between interconnects and electrodes. The intertwining

guard electrode in the sensing and driven elements of the HCLPM isolates each electrode and interconnect from all the others. Figure 3-19 shows a side view of the electrode structure in the HCLPM. The guard electrodes, both between and above the sensing electrodes, 3 and 4, isolate electrode 2. In effect, the guards make C_{1-2} a function of only the lateral position of electrodes 1 and 2 and the operating gap.

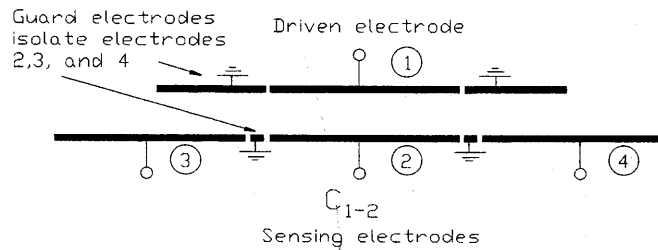


Figure 3-19: Guard used to isolate the individual electrodes and interconnects in the high resolution position sensor design

Parasitic capacitance is a particular type of stray capacitance between the interconnects, electrodes, or leads and the substrate. This can be thought of as a distributed capacitance along the entire length of a conductor. By choosing an insulating substrate, the parasitics are eliminated. Chapter 4 discusses the choice of glass as the substrate for the HCLPM. The capacitance between the leads that attach to the electrical pads is also commonly referred to as parasitic. The capacitance from one lead to the other can often reach $100pF$ or more to obscure the relatively small changes in capacitance of the sensor. By mounting operational amplifiers (op-amps)

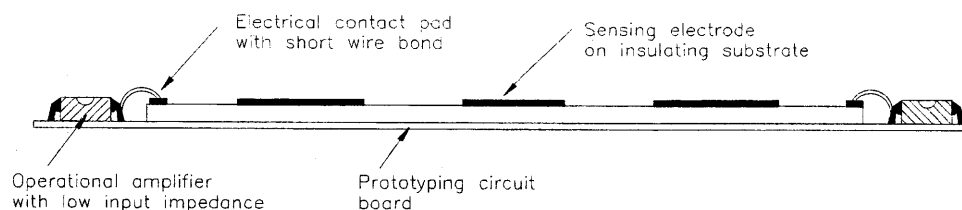


Figure 3-20: Buffering of input and output signals to avoid large parasitic capacitances at the leads

next to the two sensing elements, a thin wire ($50\mu m$) can be bonded between the

contacts on the sensor and the contacts on the op-amps without introducing much parasitic capacitance. The idea is to buffer the signal as close to the point of extraction from the sensor (contact pads) as possible. This configuration is known as a hybrid circuit design. There are two parts to this design: the hybrid interface and the measurement circuit. These topics are discussed in Sections 3.3.2 and 3.3.4.

The best way to achieve high resolution capacitance detection is to use either an integrated circuit for signal processing or an analog-to-digital converter prior to transporting the signal away from the sensor. Both of these techniques practically eliminate parasitic capacitance across the leads. The HCLPM design is well suited to the use of integrated circuitry because the microcircuit fabrication process is similar to the one that was carried out to build the electrode and interconnect structure. However, because of time constraints, the topic of integrated circuit design was beyond the scope of this project.

3.3.2 The hybrid interface

Figure 3-20 illustrated the general idea behind the hybrid interface: buffer the output signal with a low input impedance amplifier next to the contact pad on the sensor. The interface routes the output signals to the proper places for signal processing and recording. Figure 3-21 shows the hybrid interface network for the sensing element. A

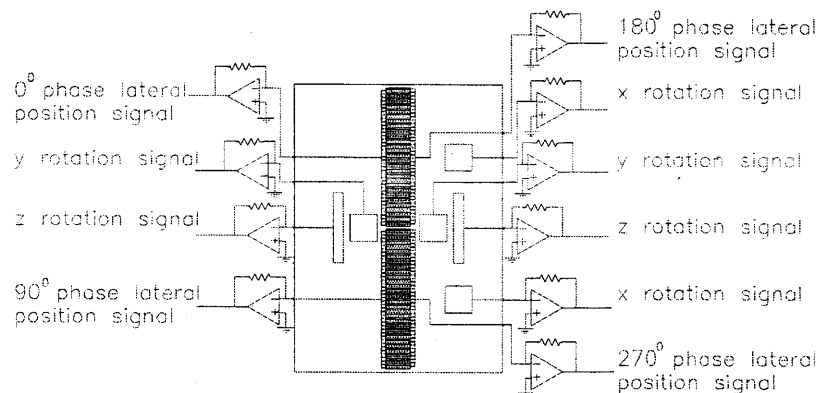


Figure 3-21: Hybrid interface op-amp network for the sensing array of electrodes

plan to implement this network with the actual sensor and hardware is discussed in

3.3.3 Stray immune measurements

Stray immune measurements can be either inherently immune or actively immune. In inherently immune measurements, the presence or absence of stray capacitances does not affect the capacitance measurement; no special circuitry is needed. Actively immune methods use coercive techniques to enable the system to reject strays. The terminal structure determines which type of measurement is most compatible with the system. If both of the terminals in the measured capacitors are electrically floating, then an inherently immune measurement technique is used and strays are eliminated. This method relies on a low input impedance current detector, which shunts the stray capacitances to ground (Figure 3-22). Typically the input is at virtual ground and the external surface is grounded; therefore, there is no induced charge across the stray capacitance S_1 .

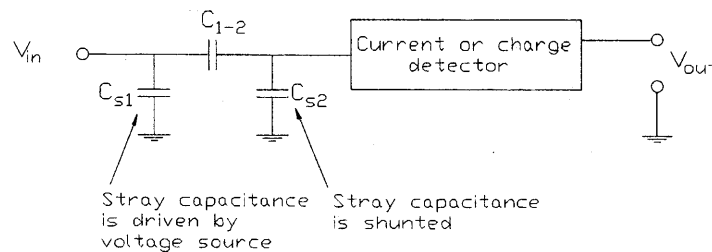


Figure 3-22: Inherently immune measurement of capacitance C_{1-2} with low input impedance current detector

The most common measurement circuit for capacitance is the capacitance bridge network. These systems compare the response of the measurement capacitance to the response of a reference capacitor to achieve the highest detection sensitivities. Since the value of the reference capacitor can change with either drifts in the environment or varying operating conditions, a technique called auto-balancing is used to optimize the response of the bridge detector to changes in the measurement capacitance. In effect, the response of the reference capacitor tracks the response of the measurement

capacitor; thus the two are always equal.

3.3.4 Circuit for capacitance measurement

The block diagram for the proposed capacitance measurement circuit is shown in Figure 3-23. Since the circuit was designed and fully analyzed by Leip [25], only the

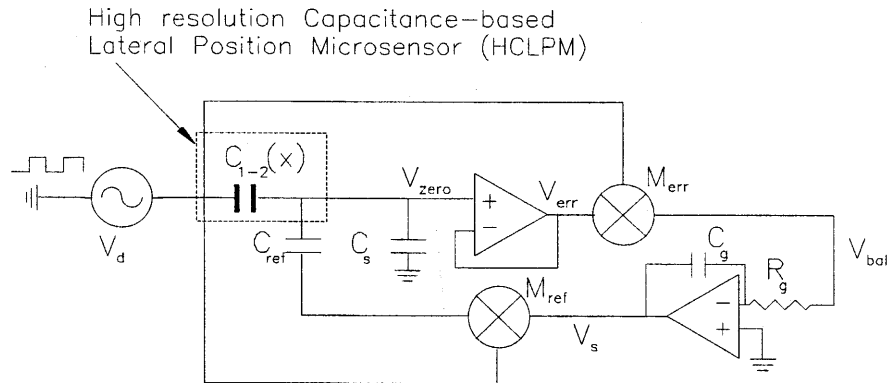


Figure 3-23: Stray immune measurement of capacitance C_{1-2} with auto-balancing circuit design from Leip

qualitative operation of the circuit is described here. The interesting feature of the design is auto-balancing. During a measurement, the value of the reference capacitor, C_{ref} , tracks the measurement capacitance, C_{1-2} ; consequently, the capacitance bridge is always balanced, and is always operating at the point of highest detector resolution and sensitivity. Also note from the discussion in Section 3.3.3 that the circuit in Figure 3-22 is stray immune because it is always balanced (i.e. V_{zero} reaches zero at the balance point); therefore, the stray capacitance from the sensing electrode to ground has no affect on the measurement accuracy.

The figure shows the location in which the HCLPM will be inserted after the sensing and driven elements have been fabricated. The measurement scheme works in the following way: the driven array of electrodes is driven with a voltage V_d , which generates an induced charge on the array of sensing electrodes. Note that V_d is chosen to be a square wave in order to produce a *constant* error instead of a time-varying error signal. The induced voltage on the sensing electrodes combines with the reference

voltage, $V_s \frac{V_d}{M_{ref}}$, to produce the square wave, V_{zero} . The greater the difference between C_{1-2} and C_{ref} , the higher the magnitude of V_{zero} . At the first multiplier the driving voltage square wave is multiplied by V_{zero} . Since both of these signals are square waves, the product of the two, V_{bal} , is a positive constant. Next, V_{bal} is integrated to produce the output voltage, V_s . This output voltage is directly proportional to the measurement capacitance,

$$V_s = -M_{ref} \frac{C_{1-2}}{C_{ref}} \quad (3.5)$$

Since V_s indicates the ratio of the measurement and reference capacitances, the second multiplier causes the applied voltage to C_{ref} to change until the balance point, $V_{zero} = 0$, is reached. This is precisely the condition required for a stray immune measurement: no voltage across the stray capacitance, C_s . A picture of the actual testing circuitry is shown in Figure 3-24. The various components in the circuit are given in the figure.

The choice of integrator parameters determines the speed of response to changes in capacitance, while the product of the parameters determines the open loop gain. The specific values will be chosen during the experimental phase of this project. Typical values of R_g and C_g are 0.1 to $5k\Omega$ and $1nF$, respectively; these values yield response times of $100ns$ to $5\mu s$. This rapid response to changes in capacitance translate into a high slew rate for the HCLPM.

To illustrate the function of the circuit, a simulation of the HCLPM output is shown in Figure 3-25 for an M_{ref} multiplier gain of 10 and a $5pF$ reference capacitor. Note that a $10nm$ change in position produces a $1fF$ change in capacitance, which generates a $1mV$ change in voltage, V_s . Only the lateral position signals are shown for the four different spatial sets of electrodes.

3.4 Summary of the design

The design procedure of the HCLPM has been summarized in this chapter. The theory of Chapter 2 helped to choose the size, location, and configuration of the sensing and driven electrode arrays in the two elements of the sensor. A brief review

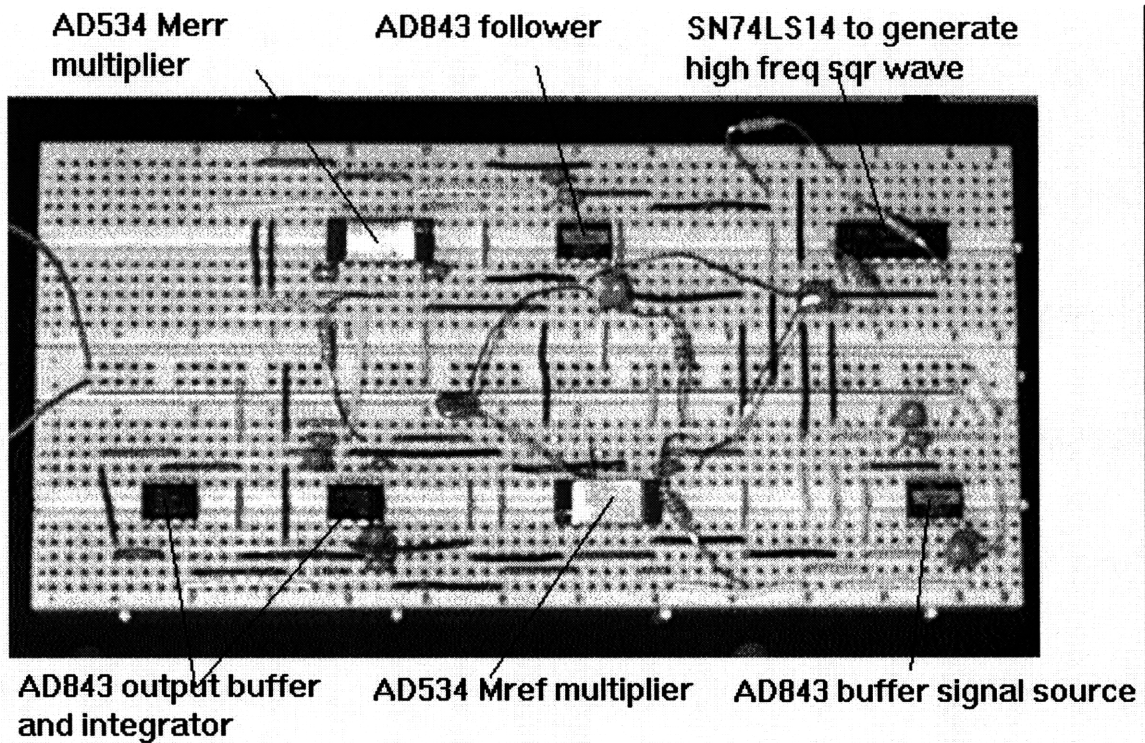


Figure 3-24: Auto-balancing, stray immune capacitance detection circuit by Leip
of the auto-balancing, stray immune capacitance detection method was also given. In the next chapter, the fabrication procedure is discussed and the results of the process flow are given.

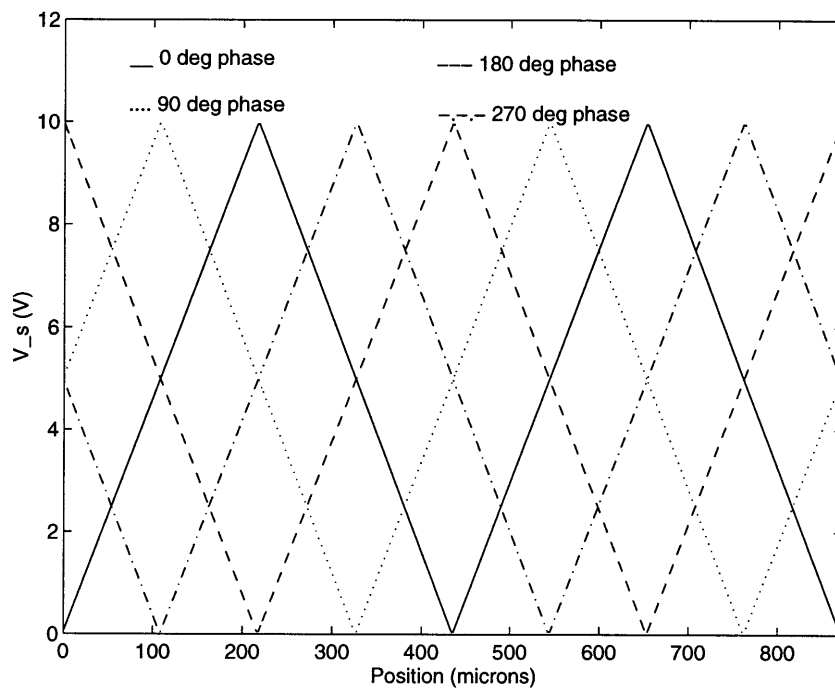


Figure 3-25: Simulation of the four phase lateral position sensing output for $M_{ref} = 10$ and $C_{ref} = 5pF$

Chapter 4

Fabrication

The fabrication process for the HCLPM was carried out in the facilities at the Microsystems Technology Laboratory (MTL). Since the Integrated Circuit Laboratory (ICL) does not allow the use of glass or gold, most of the processing took place in the Technology Research Laboratory (TRL). In fact, the facilities at TRL were ideal for refining the process to meet the stringent design requirements. However, a few minor adjustments were made to the design to avoid needless heroics during the fabrication process. The overall objective of the microfabrication process was to balance the demands on resolution and accuracy in the preferred HCLPM design with the constraints on the available process tools. This chapter describes the procedures, intricacies, and results of the fabrication process.

4.1 Selecting a fabrication method

The HCLPM's construction, unlike that of the other high resolution sensing arrays, relies entirely on high resolution fabrication methods. The ruler, or reference scale, is the most critical element in this sensor because it determines the highest measurable resolution in position. Too dense to be built with conventional machining processes, the electrode arrays were made instead in microfabrication facilities. In effect, microfabrication leverages the technology and experience of the integrated circuit industry by combining lithography with high resolution chemical or physical etching to create

high resolution, high precision structures.

The fabrication process was formed by studying the possible ways in which the HCLPM design could be realized in TRL. In addition to a semester of academic and laboratory work at MIT¹, a short course in microfabrication at the Microfabrication Center of North Carolina (MCNC) was also taken to help better define the research. The goal of the study was to adapt the process tools to meet the demands of the HCLPM design. The complete process consisted of a littany of "opsets"² involving wet and dry cleaning, optical lithography, electron beam deposition, baking, wet and dry etching, and inspection. These operations are discussed in Sections 4.1.1 through 4.1.9.

4.1.1 Cleaning operations

Several cleaning operations were used to remove particulate matter, insoluable organics, and ionic and other heavy metal contaminants. These cleanings dramatically improved the adhesion and interfacial bonding of the thin-film layers. Some examples of wet and dry cleaning agents include detergent solution, acetone, methanol, ozone, and piranha solution (sulfuric acid-hydrogen peroxide mix). Extreme care was taken to prevent the attack and corrosion of the patterned layers that were being cleaned. The most relevant concern in this research was the susceptibility of aluminum to all types of acids and bases. The electrode patterns were constructed with aluminum because of it's very low resisitivity. Unfortunately, the aluminum is also very soft, a serious drawback that was encountered throughout the fabrication process.

Even though TRL is seated in a class 100 cleanroom, where full body clean garments were worn, cleaning operations were nevertheless manditory for high resolution lithography. In addition to standard cleaning procedures, special precautions were also taken to limit the moisture in the storage environment during the down-time between process steps. Dry boxes in TRL provided an extremely low humidity space

¹MIT course 6.152J, *Microelectronics Processing Technology*, was taken and TRL technicians were consulted to obtain the necessary training.

²*Opset* is a term used in MTL to describe a list of operations that defines an entire process or subprocess.

in which to store process wafers.

4.1.2 Lithographic technique

Lithography is the patterning process in microfabrication, and chemical or particle etching is the machining process. First, a material layer is coated with photoresist, a viscous mixture of an inhibitor, or photoactive compound, a solvent, and a resin. Next, the resist is baked and then exposed to a particular pattern of illumination, which alters the solubility of the resist in the developing agent. After the resist is exposed and developed, the remaining pattern serves as an etch mask during the chemical machining process. The unprotected regions without resist are then stripped from the surface, leaving only the desired pattern.

The following sections summarize the primary elements of lithography as it pertains to this research. Photomask generation, photoresist technology, the illumination sources for exposure, and the practical limits on pattern resolution are all discussed.

4.1.3 Photomask generation and pattern yield

The most challenging aspect of the fabrication process was to maintain pattern integrity. In the photomask generation process, the HCLPM design was modified several times before actually printing the final photomask. Each iteration added to the width of the smallest dimension in the pattern until there was no evidence of any material shorting across the narrow gaps. Figure 4-1 illustrates the iterative process for a magnified area of a process photomask. The photosteps were also plagued with the same kind of pattern deterioration problems as the photomasks. These issues are further discussed in Section 4.1.5.

The difficulty of fabricating the photomasks and the lithographic patterns of the HCLPM can be expressed in terms of yield. In the terminology of microfabrication, the yield is the percentage of working devices across the entire wafer at the end of the process. Most integrated circuit processes focus on only a small portion of the wafer (see Figure 4-2). This makes it relatively easy to create many operational

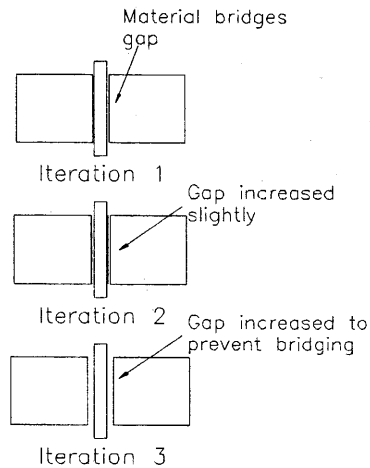


Figure 4-1: Example of iterative process needed to resolve photomask patterns

devices, thus high yields are commonly achieved. In contrast, the yield across the entire center portion of the wafer in the HCLPM microfabrication process had to be one-hundred percent. Anything less than perfect would have ruined the single device on the wafer. Since this area is much larger than the device area for integrated circuits, the HCLPM process was more yield dependent. Not only was the original mask more difficult to create, the ensuing patterns in each lithographic transfer were also distinctly challenging. The difficulty is also related to the serial interconnect structure of the HCLPM (refer to Section 4.1.5).

4.1.4 Photoresist technology and the illumination source

There are two types of photoresist: positive and negative. The difference between the two technologies is that bonds break in exposed positive resist, whereas bonds form in exposed negative resist. Therefore, in the proper developing agent, positive resists dissolve before exposure and negative resists dissolve after exposure. Figure 4-3 illustrates the positive resist process. Both types of resist are commonly used in

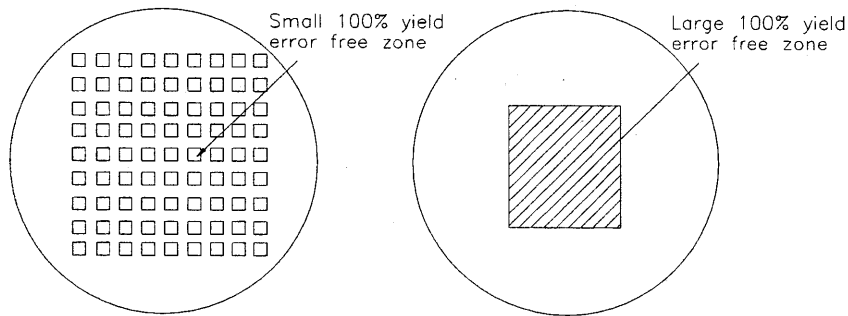


Figure 4-2: Illustration of dissimilar yields in the HCLPM process and an integrated circuit process

microfabrication, but positive resists can provide higher pattern resolutions because they exhibit higher contrast and less swelling. The term contrast describes the region of separation between the exposed and unexposed regions of resist. A sharper contrast is preferred because the sudden change in resist solubility leads to sharper, more accurately defined patterns. Swelling is also an important characteristic of the photoresist material. In positive resists, the undissolved regions of resist do not absorb much of the developer solution; consequently, positive resists swell less than negative resists.

Contrast and swelling combine to limit lithographic resolution. The Minimum Feature Size (MFS) is the smallest resolvable dimension in a particular resist pattern. For optical lithography and positive resist processes, the MFS is typically in the range $0.8\mu m$ to $1.5\mu m$. [37] Of course, higher resolutions can be obtained by choosing different sources of illumination for exposure and different resist chemistries or thicknesses. Recall that the HCLPM design has a MFS of $4\mu m$; this is the width of the interconnects throughout the structure. Therefore, optical lithography was chosen for this research. Optical lithography was selected for this work instead of ultraviolet or electron beam lithography because the latter techniques were unnecessarily complex and were not readily accessible to individual student users in MTL, and because optical lithography was the most familiar process.

Etch resistance is also an important property of the resist material. The etchant

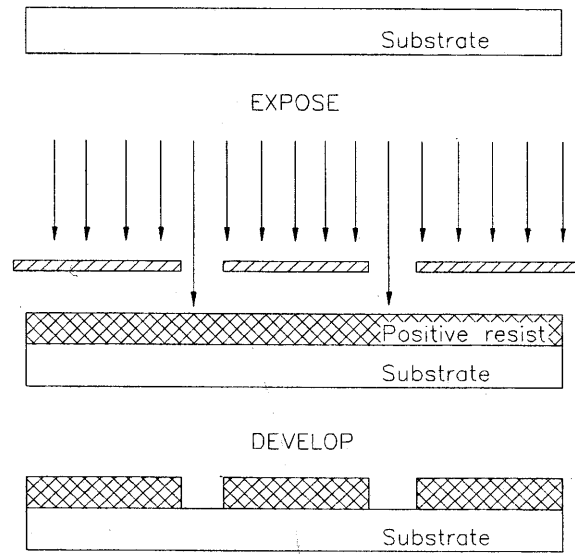


Figure 4-3: Photo step in a positive resist lithographic process

is selected so as to attack the substrate but ignore the resist. Although the selectivity ratio between the etched material and the resist is usually much greater than one, the thickness of the resist must also be varied to control the resistance to etch. Positive resists again have the advantage in this respect, since they exhibit less swelling than negative resists when the resist layers are made thicker, and so do not sacrifice higher pattern resolution. Positive resists were used throughout the HCLPM fabrication process.

4.1.5 Practical resolution limits

Although the theoretical optical MFS was clearly small enough to suit the design in Chapter 3, the MFS was limited to $7\mu m$ because of the difficulty in making long, high resolution features. For example, a short, thin feature with a small length-to-width aspect ratio has a smaller MFS than a long, thin feature. Figure 4-4 illustrates the idea. The line with length $L1$ is long and thin, spans a greater area on the surface layer than the line of length $L2$, and so endures larger gradients in temperature and stress across the surface. The higher gradients tend to strip the long line from the

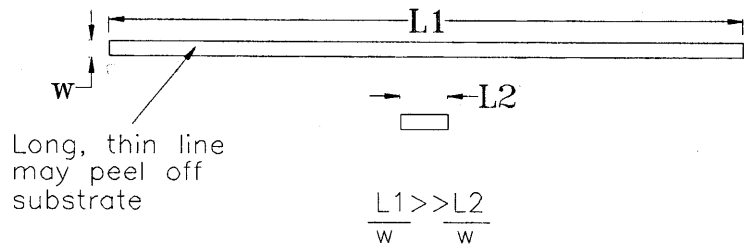


Figure 4-4: Two different interconnect aspect ratios to illustrate the difference in minimum feature size

surface, whereas the short line remains securely fastened. There are two reasons for this behavior: static force imbalance and poor layer adhesion. As the line length increases, the bending stiffness (elastic strength) decreases and the residual stress increases. This force imbalance can grow large enough to strip the line. An alternative way to view this phenomenon uses the surface-to-volume ratio. Since microfabrication works by creating thin-film patterns, high surface-to-volume ratios are an inherent part of the process. The large ratio is indicative of the relatively strong surface forces, which tend to strip the pattern away from the substrate. Poor adhesion can also cause stripping.

The best way to prevent large residual stresses is to use only low temperature process steps. By reducing the thermal gradients in the fabrication process, the adhesion and stiffness of the line are large enough to prevent peeling. Adhesion can be improved by strengthening the bond between the substrate and the thin-film layer. For example, aluminum layers with a thin oxide cover-layer bond better to many surfaces than do pure aluminum layers. Low temperature processing and adhesion strengthening are both implemented in the HCLPM fabrication process to prevent the delicate patterns from lifting.

There is an additional resolution limit that is related to the idea of yield and the type of interconnect design structure. Consider the two interconnect layouts in Figure 4-5. The structure on the left in the figure is serial in nature; a single open circuit along the serial path disables many of the electrodes. In other words, the interconnect

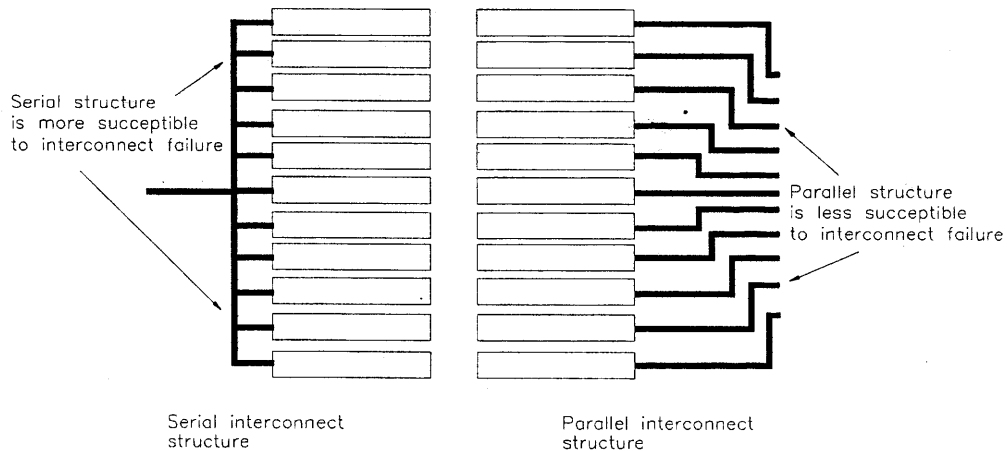


Figure 4-5: Two different types of interconnect structures, serial and parallel, with different yield requirements

yield requirement is near 100% for the serial structure. The parallel structure on the right in the figure is more robust to defects in individual interconnects; one open circuit disables only one electrode. Therefore, the required interconnect yield for the parallel structure is much lower than for the serial structure.

The HCLPM interconnect design is similar to the serial structure in Figure 4-5. Although the parallel structure is in some ways easier to build, implementing a multiple input parallel structure has its problems as well. For example, the signal from each electrode will experience a different resistivity, and thus a different loss in signal energy. The added parasitic capacitance at each one of the input pads is also a problem in the parallel structure. The decision to use the serial structure was based primarily on these two critical issues.

4.1.6 Electron beam deposition

Electron beam (e-beam) deposition can be used to create polysilicon, metallization, and dielectric thin-film layers. During the process, an electron gun is directed towards a crucible of the desired deposition material. As the material is locally evaporated in a low pressure chamber (8×10^{-7} torr), it travels from the crucible to an elliptical train of wafer carriers, where it uniformly coats the surface of the wafers. The

beam is typically operated at a voltage greater than 10 kV. The advantage of e-beam deposition over other forms of deposition (e.g. sputtering) is the high purity of the films. Since the vacuum is high, the contamination in the chamber is very low; low contamination translates into high film purity. [11]

In addition to being pure, e-beam deposited films are also uniform across the surface of the wafer. This is critical for the HCLPM, which makes a differential measurement that is most effective when the gap is uniform across the entire surface of the sensor. The composition of the film is also uniform across the wafer surface; however, compositional changes may occur from run to run.

A strong bond is another important characteristic of e-beam deposited layers. The electrodes in this research were created in an aluminum layer. In this case, the bond was achieved locally, between the aluminum and the PYREX substrate oxide layer. This reaction was extremely stable and created a strong bond. There were materials in this research that did not bond well to the PYREX substrate. For example, since gold is a noble metal, it did not bond well to the substrate. This type of bond required a thin layer of reactive material between the PYREX and the gold layer to form a strong bond. Chromium was an excellent material for this purpose.

4.1.7 Baking operations

Photoresist baking and dehydration baking operations were essential elements of the HCLPM microfabrication process. In each photo step, the wafers were coated with resist and then pre-baked prior to exposure. This was to promote high integrity pattern retention during and after the development step. The pre-bake simply evaporated excess solvents in the resist, leaving only the matrix and the photoactive compound. Ultrasonic agitation, stirring, rinsing, and drying operations were all potential sources of pattern destruction in the development process.

A post-bake process was also done prior to etching the material layer in order to densify the resist. Without this baking operation, the pattern would have been in danger of being destroyed during the etch due to such influences as high energy bombardment and agitated rinsing. Dehydration baking was yet another variation

of baking in the HCLPM fabrication process. This was particularly useful before the photoresist spin-coat process. By performing the bake in an oxidizing environment, the adhesion of the polymeric resist was strengthened. Adhesion was also improved after all remnants of moisture were removed from the substrate surface during the bake.

The temperature and time for each baking process were chosen to satisfy the specifications of the photoresist manufacturers. High temperatures were needed to cure the mixture, whereas low temperatures were sufficient to densify the mixture. The proper oven settings were chosen to create a stable resist matrix for pattern transfer.

4.1.8 Wet and dry etching operations

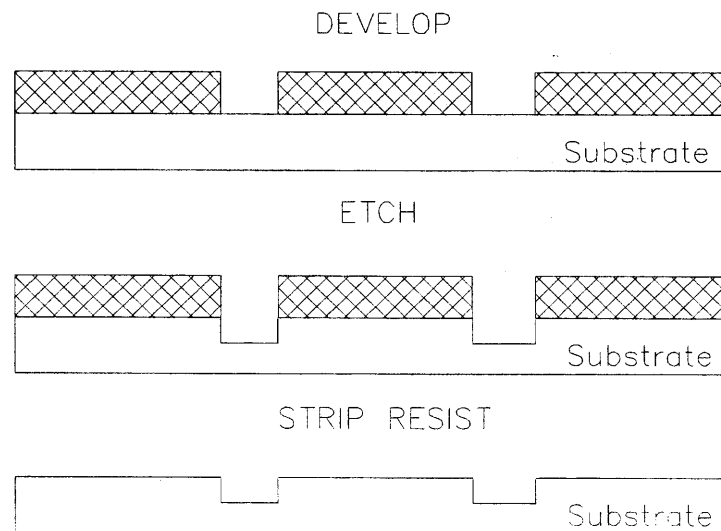


Figure 4-6: Continuation of pattern transfer with chemical etching operation

The actual pattern transfer was completed once the etching operation was performed. Recall that Figure 4-3 ended with the development process. Figure 4-6 illustrates the remaining steps needed to create the patterned material layer. After the etchant removed material to form the pattern, the photoresist was stripped away with any

one of a number of processes: plasma ashing, hot chlorinated hydrocarbon soak, or mechanical scrubbing.

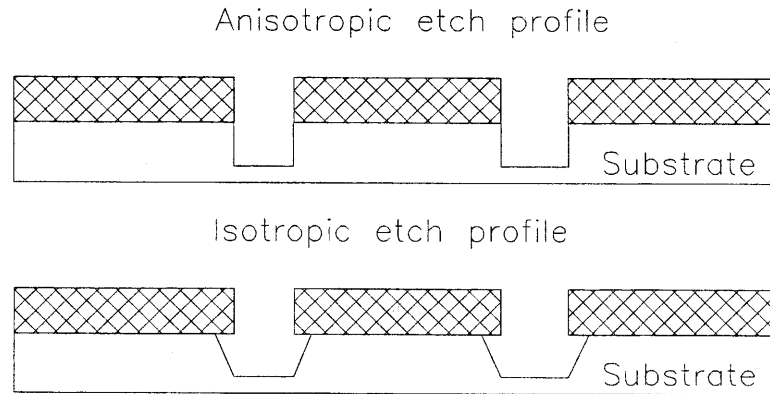


Figure 4-7: Isotropic and anisotropic post-etch profiles for wet chemical etching processes

Etching can involve either wet chemical processes or dry plasma processes. The key control parameters in this research for wet chemical etching were the vertical and lateral etch rates. During a wet etch process, the etchant attacks all of the material in which it comes into contact. The ideal and the actual post-etch profiles are shown in Figure 4-7. The anisotropic (vertical sidewall) profile is the ideal case; only the material in the vertical direction is removed to create the pattern. The isotropic profile is what actually occurs. Note that there is a substantial lateral etch rate in addition to the high vertical etch rate. Since the etch rates depend on both temperature and pattern geometry, the profile can be fine-tuned to provide the best results.

Reactive Ion Etching (RIE) is one type of dry etch process. The RIE hardware in TRL consisted of an r.f. sputtering chamber, which was filled with a combination of chemical species. As the molecules collided with one another, neutral and ionized energetic species etched the substrate material. This etching process was highly anisotropic in nature because the wafers were placed perpendicular to the r.f. field.[11] The chemical species for etching silicon and silicate glasses (e.g. SiO_2) were a combination of fluocarbons (CF_4) and ozone or hydrogen gas.

The time to etch a given profile can be measured either manually with visual inspection or automatically by the processing equipment. The manual method is often referred to as visual end-point detection. In this procedure, the etch is continued until the pattern visually clears. Although on-line inspection may be adequate enough to determine the etch time for course patterns, more sophisticated off-line high magnification inspections are needed to determine the end-point of a high resolution etching process. The automatic etch time is measured by using end-point detection features in the RIE process hardware itself. *In situ* optical interference patterns help the machine to gauge the film thickness as the etch progresses.

4.1.9 Inspection procedures

A variety of inspection techniques were used to characterize the process results at the end of each step. Inside of the cleanroom facility, optical microscopes with 20X – 60X magnification were used to monitor the process. Unfortunately, the cameras in TRL were not functioning properly at the time of this research; therefore, photographs of the results could not be taken after each step. All photographs were taken with a Scanning Electron Microscope (SEM) once the electrode pattern had been generated. These photographs were sufficient to characterize the process results.

The Zeiss DSM 982 Gemini SEM was operated at 5 kV and 154 μA . In order to avoid charging in the sample, a thin layer of gold was sputter deposited onto the aluminum pattern. Although aluminum is conducting, it nevertheless charges significantly more than gold at the image point of the electron beam. The gold layer helped to carry the charge away from the point of impact of the beam. A piece of conducting tape was used as well to electrically ground the gold covered pyrex wafer. The highest magnification photographs taken with this setup were at 2000X magnification, even though magnifications as high as 200,000X were possible with the SEM. The pixel resolution of each photo was 512X512.

4.1.10 Cost limitations on the process

Cost was a self-imposed limitation on the microfabrication process. Although it would be inexpensive to batch fabricate many HCLPMs, the cost of building and assembling a prototype was relatively costly. In order to cut fabrication costs, the two shielding layers underneath the driven and sensing electrode arrays in the preferred design were omitted to reduce the number of process masks by two and to eliminate two additional deposition processes. This design modification was only made after having concluded that it would not significantly alter the performance of the microsensor.

4.2 Overview of the fabrication process

The driven HCLPM element is used as a means to discuss the fabrication sequence. The cross-sectional diagram for this element is shown in Figure 4-8. There are three patterned layers in the diagram: the bushings on the glass wafer, the aluminum electrodes and interconnects, and the silicon dioxide passivation layer. Each of the patterns were created using optical lithography, with five photomasks in all. The first step in the fabrication sequence was to generate the Process Flow Representation (PFR) for administrative, scheduling, and billing purposes at MTL. During this first step, the photomasks were also designed and fabricated. The last three steps used these masks to pattern the three different material layers. Sections 4.2.1 through 4.2.4 describe each of the four primary process steps:

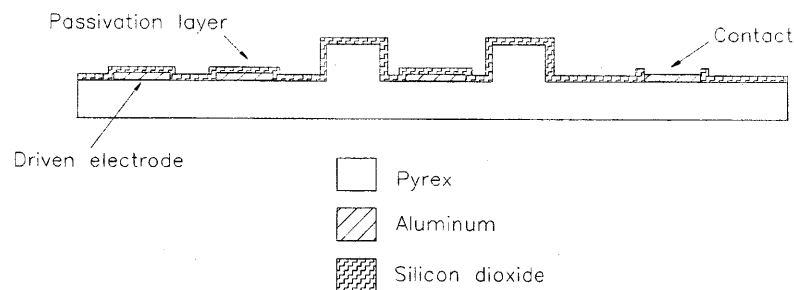


Figure 4-8: Cross-sectional diagram of the finished driven element

1. Mask generation and PFR preparation
2. Glass pattern formation
3. Aluminum pattern formation
4. Silicon dioxide pattern formation

4.2.1 Step 1: Mask generation and PFR preparation

Mask generation

The process photomasks were generated within the standard IC mask production facility at MTL. According to procedure, the individual patterns were first constructed inside of KIC, a simple graphics editor for integrated circuit design. [10] The patterns were specifically designed to function in a positive resist lithographic process. In other words, the mask material was removed from the surface of the mask plate wherever there were gaps in the particular pattern. Within the software, each pattern was assigned a unique layer name, which would later serve as the mask name for that layer in the PFR. For example, **RE** and **RP** indicate the electrode and passivation patterns on the driven element. The other layer names, associations, and characteristics are listed in Table 4.1. Note that there were two different wafersets in the fabrication process: the driven element set and the sensing element set. In various photo steps, the driven element was exposed to the **GD**, **RE**, and **RP** patterns, while the sensing element was exposed to the **SE** and **SP** patterns. All of these different layers were placed into a single KIC coordinate file.

After completing the coordinate file, it was converted to CIF format with a local translator, *kictocif*, and then submitted to the job queue at MTL using *cgsuubmit*. The characteristics in the table were the parameters needed to submit the patterns. The **Boxes** column in Table 4.1 contains the number of rectangles with which the Gyrex mask processor could assemble the associated photomask pattern. For example, the processor needed 1387 rectangles, placed either parallel or perpendicular to one another, to assemble the **SE** emulsion pattern. The field type simply indicates whether

Name	Association	Polarity	Boxes
GD	Pattern in pyrex layer for contact bushings	Clear	3
SE	Pattern in aluminum layer for sensing element electrode	Clear	1387
RE	Pattern in aluminum layer for driven element electrode	Clear	887
SP	Pattern in silicon dioxide layer for sensing element contact holes	Dark	71
RP	Pattern in silicon dioxide layer for driven element contact holes	Dark	64

Table 4.1: Photomask layer names, associations, and specifications

the mask background is filled in (dark) or empty (clear). In manual development and etching processes, clear field patterns are preferable to dark field patterns for two reasons: first, alignment is easier with a clear field mask, and second, the time to develop and etch the pattern is more easily measured with the strong visual end-point in the field as it clears.

Next, a Gyrex technician at MTL processed the photomask work request and produced an emulsion contact mask. The Gyrex system at TRL uses a two stage process. First, a 1X emulsion mask was generated and inspected. Once the mask was determined to be accurate, the 1X chrome contact mask was printed from the emulsion mask. To minimize the amount of thermal expansion of the pattern, a five inch borosilicate glass substrate was used; both borosilicate glass and quartz have low coefficients of thermal expansion ($5 \times 10^{-7} \frac{cm}{cm^{\circ}C}$). [37] The reason a chrome mask was produced in addition to the emulsion mask was that the chrome pattern was more durable. The emulsion mask was only used once and then discarded because the pattern was easily smeared while creating the chrome mask.

The first several attempts to print an acceptable emulsion mask failed because the vacuum seal in the process was non-uniform across the surface of the plate. This is usually not a problem for MEMS devices that cover only a small portion of the

surface; however, the HCLPM was large enough to have been affected by the loss in vacuum from one edge of the sensor to the other (see Figure 4-2 in Section 4.1.3). The problem was exacerbated by other malfunctions in the processing equipment at the time of this research.

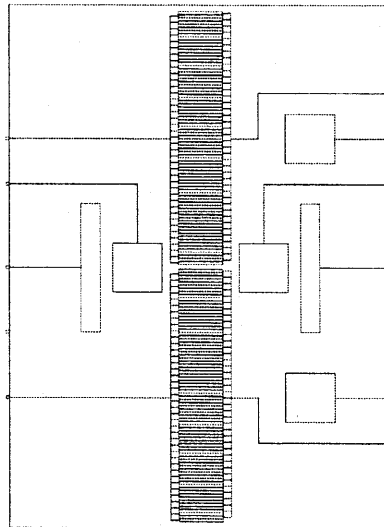


Figure 4-9: Mask layout for the **SE** (sensing electrode) photomask pattern

It took several iterations with modified designs to satisfy the process variations and create clear patterns. Figures 4-9 and 4-10 show the final **SE** and **SP** mask layouts, respectively. Note that the **SE** mask is a clear field pattern; therefore, the features in the mask pattern are digitized in the layout software. The individual sensing electrodes along the center of the mask are too thin to be seen in the full field view of Figure 4-9. There are also alignment marks at the perimeter of the pattern field. The process of alignment is discussed in Section 4.2.4.

The **SP** mask in Figure 4-10 is a dark field pattern; consequently, the holes in the mask pattern are digitized instead of the features. Since there are only nine contact pads in the sensing element of the HCLPM, the **SP** mask has only nine square features. Each square is $200\mu m \times 200\mu m$; a broken box has been drawn around each of the squares to highlight their location. Although the illustration appears somewhat

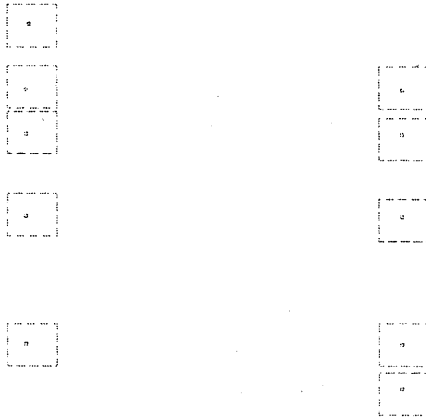


Figure 4-10: Mask layout for the **SP** (sensing passivation holes) photomask

unclear, this is simply a result of the small feature size of the individual squares. Figure 4-11 is an illustration of the overlaid combination of all the patterns. Each pattern was transferred to a chrome layer on a single glass plate. The **SE** and **RE** masks were photographed to illustrate the finished product; the photos are shown in Figures 4-12 and 4-13. Only the center portion of the glass plate is shown since the perimeter area is transparent glass with no pattern.

PFR preparation

The PFR for the fabrication sequence was written during the photomask generation process. PFR is essentially a high-level programming language for microfabrication. Standard operations, or *opsets*, were modified to suit the HCLPM design, and then were combined into a complete PFR. The usefulness of PFR is primarily the organization it brings to TRL, the administrative staff, students, and technicians. The basic PFR structure is well documented elsewhere [8]. Because of the length and complexity of the PFR for the HCLPM, it is only summarized here. A full listing of the code is given for reference in Appendix B.

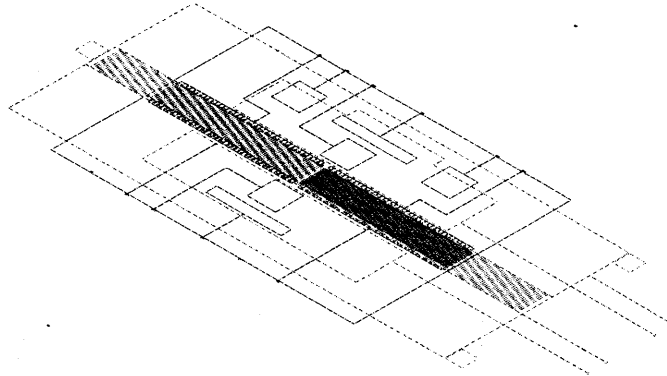


Figure 4-11: Overlaid mask layout for five photomask patterns

The fundamental structure of the PFR for the HCLPM process is shown in Figure 4-14. Each opset within the process is called by the main file, *cap-sense.fl*, and is defined in the root directory (see Section B.1). As an example of PFR syntax, consider the glass etch step in the process. The operation is called by *cap-sense.fl* midway through the file. The name of the etch operation is *pyrex-wet-etch.fl*. This is a sub-process flow, which details the glass etch; it lists the time, thickness, instructions, and acid type involved in the etching process. The opset *pyrex-wet-etch.fl* was linked to the file *pyretch.fl* (see Section B.1.2) through a binding in *more-bindings.fl* (see Section B.1.1). Since *pyretch.fl* in turn called the library entry *etchgls* in *more-utils.fl* (see Section B.1.3), it was the *etchgls* utility that was ultimately executed. The other opsets in *cap-sense.fl* were also linked to different opsets and utilities. Each referencing sequence was carried out upon execution of the PFR.

4.2.2 Step 2: Glass pattern

The objective of this step was to create the HCLPM bushing pattern (Figure 4-15) in the 100mm diameter glass wafer that will eventually hold the driven electrode

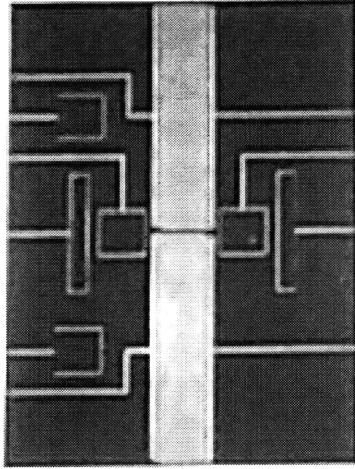


Figure 4-12: Completed SE chrome photomask pattern and plate

elements. A glass substrate was chosen instead of silicon because glass has a lower coefficient of thermal expansion than silicon ($\alpha_{glass} = 30 \times 10^{-7} \frac{cmC^{\circ}}{cm}$; $\alpha_{Si} = 6 \times 10^{-6} \frac{cmC^{\circ}}{cm}$), and because silicon has a large lossy capacitance (refer to Section 2.2.3). The glass wafers are made of PYREX, a trademark material with Glass Code 7740. The glass manufacturer maintained a thickness tolerance across the wafer to within 4 waves per inch ($0.1\mu m$ per inch).

The procedure for creating the bushings is shown in Figure 4-16, along with the step-by-step cross sectional wafer diagrams. The first step in the procedure included a thorough commercial detergent clean outside the clean room facility. The solution was agitated ultrasonically per the manufacturers specifications. The purpose of this general cleaning was to desorb particulate matter from the surface of the wafer before entering the clean room. Next, a Piranha clean was done on the wafers to remove organic contaminants from the surface of the wafers. The chemical formula of the Piranha solution is $H_2SO_4:H_2O_2$ with three parts sulfuric acid and one part hydrogen peroxide. The mixture was extremely aggressive as it attacked the contaminants on

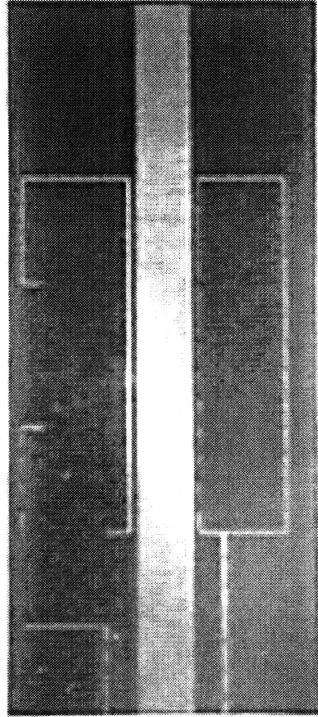


Figure 4-13: Completed RE chrome photomask pattern and plate

the surface in the midst of an exothermic reaction. Full-body chemical gear and face shield were worn at all times throughout this research while working at the acid-hood in TRL, a Laminaire wet etch processing station. The final cleaning step was a 30 minute immersion in UV ozone.

After cleaning the wafers, two consecutive e-beam depositions were performed with the Temescal VES2550 in TRL. These two metal layers served as the etch mask during the PYREX bulk micromachining process. First, an adhesion layer of Cr was deposited at a rate of $1.5 \frac{\text{Å}}{\text{s}}$; second, a 1000Å layer of gold was deposited at $3.0 \frac{\text{Å}}{\text{s}}$. The Cr layer was deposited slower to ensure uniformity of the thin-film thickness. Since Au is a noble metal, and does not bond well to most substrates, Cr was used to form a strong bond between the metal etching mask and the glass. The wafers were placed in a rotating planetary holder, which helped to produce uniform layers of material across the wafers. After pumping the system down to 9×10^{-7} torr, the

PFR Structure for the HCLPM
Microfabrication Process

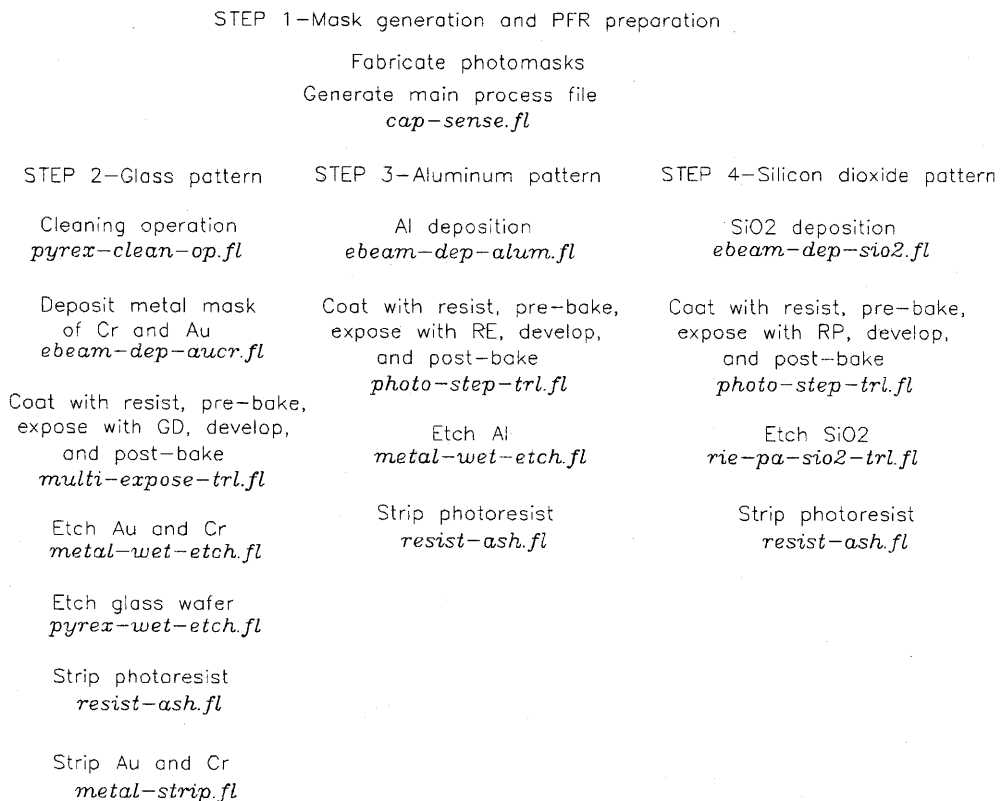


Figure 4-14: Process Flow Representation (PFR) fundamental structure for the HCLPM microfabrication process

deposition process was initiated automatically. Manual positioning of the e-beam in the crucible of aluminum was required to prevent the beam from striking the sides of the crucible. After the deposition was complete, the wafers were inspected. The quality of the layers were excellent.

Next, OCG 825 safe resist was spin-coated onto the Au layer using the Solitec coating system in TRL. The three spinning speeds were 50, 85, and 400 RPM for the deposition, coating, and spreading stages, respectively. This combination of speeds was chosen to produce a 1 μ m layer of photoresist. The first attempt at this process failed because the resist did not adhere well enough to the glass wafers during devel-

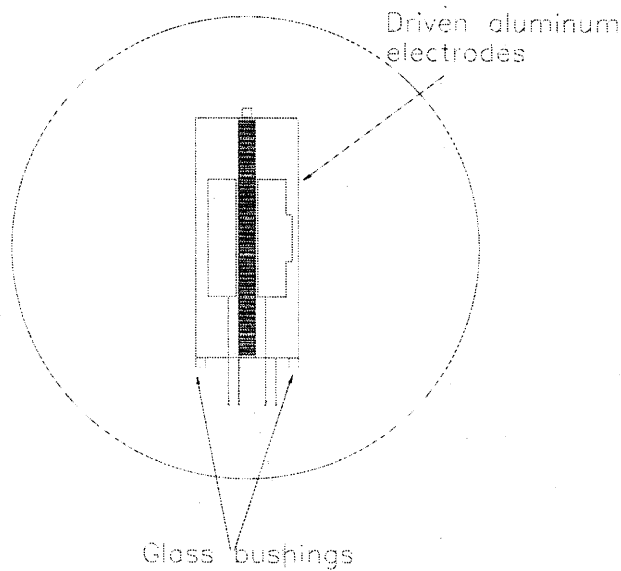


Figure 4-15: Glass bushing pattern after the completion of Step 2 in the process

opement. In the ensuing attempts, a post-bake step in the oven for 30 minutes at 120°C was used to dehydrate the surface for better adhesion. A pre-bake (softbake) step for 30 minutes at 90°C was also done prior to exposure to cure the resist mixture by removing the solvents. This step promoted pattern retention before and after development.

After the pre-bake, the Karl Suss MA-3 alignment and exposure workstation was used to expose the resist to the **GD** pattern. Recall that this pattern contained the three squares which define the contact bushings (see Figure 4-11). The mask was loaded, the vacuum was activated, and the mask was brought into soft contact with the wafer. The final multiple exposure sequence consisted of 16 cycles of 2.2 second exposures with a 4 second wait between consecutive cycles. This sequence was obtained after several sets of wafers were unsuccessfully exposed, developed, inspected, stripped, and re-coated only to attempt the process again.

The exposed resist was developed in 934 OCG 3 : 2 solution for 120 seconds, rinsed thoroughly, and then developed for a further 90 seconds to clear away the open field regions. Since the field was clear for this pattern, a visual end-point was used to detect when the development was completed. Careful microscopic inspections were done to

PROCEDURE TO PATTERN GLASS

1. Ultrasonic detergent clean, Piranha clean, and UV ozone clean.
2. E-beam deposition of 200Å Cr at 1.5 A/s and 1000Å Au at 3.0 A/s.
3. Spin-on OCG 825 positive resist for patterning metal mask layers
4. Pre-bake at 90C for 30 min, expose to GD mask, develop in 934 OCG 3:2 solution and rinse.
5. Post-bake at 120C for 30 min, etch Au with Aqua Regia for 30 sec, etch Cr with CR7 10 sec and rinse.
6. Etch glass with 500 ml H₂O : 140 ml HF : 200 ml HNO₃ with stir bar at 0.7 micron/min.
7. Strip photoresist with Piranha.
8. Strip Au and Cr with Aqua Regia and CR7 etchants.

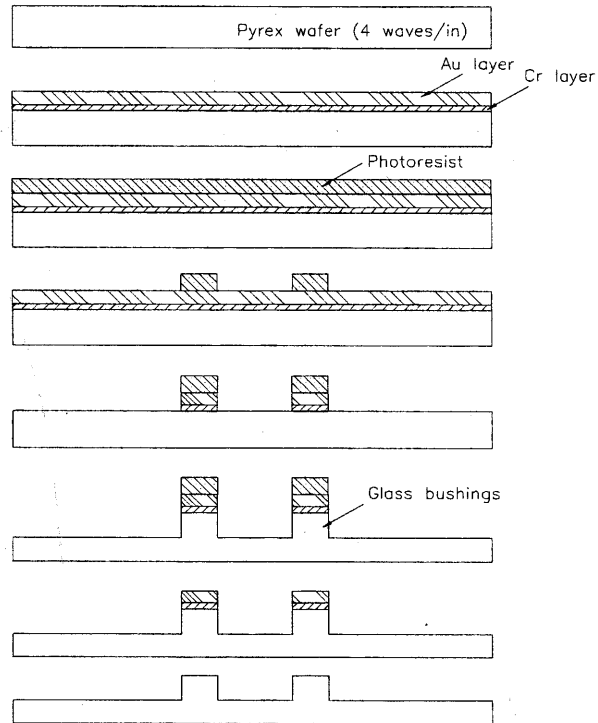


Figure 4-16: Procedure for patterning the glass layer

ensure the integrity of the intricate electrode and interconnect structure. During the first few development attempts, the interconnect pattern ($7\mu\text{m}$ width) was lifting off the wafer. The reason for the lifting effect was excessive air pressure in the hand drying procedure. Once the pressure was lowered, the square posts of resist remained attached to the wafer.

During the photo step, the individual operations were carefully timed and scheduled to produce high quality patterns. The spin-coat, pre-bake, expose, and develop steps were done consecutively on one day, and the post-bake and etching steps were done on the next day. This agenda was necessary because the life of the resist was limited to two or three days at best.

A post-bake step for 30 minutes at 120°C was done following the development step. The temperature and time of the post-bake were chosen to vaporize all of the developing solution that was absorbed by the unexposed resist. After baking

the patterned resist, the metal mask was etched, one layer at a time. Aqua Regia (3 : 1 HCl : HNO_3) was used to etch the Au layer for 30 seconds. After mixing the two acids, the solution was permitted to sit until it became a deep pink color. The wafers were etched one at a time once the the solution had stabilized. Next, CR7 Chromium Etchant was used to etch the Cr layer for 10 seconds. Both of these etches were monitored until the visual end-point was reached. Thorough rinsing and drying procedures were carried out after each of these etching steps.

Next, the glass etch was performed in an HF solution: 500 ml H_2O : 140 ml HF : 200 ml HNO_3 . The vertical etch rate was approximately $0.7 \frac{\mu m}{min}$, and was carried out for 28 minutes. This produced bushings that were $20 \mu m$ tall. After a thorough rinse, the photoresist was stripped with Piranha, an exothermic solution of 3 : 1 H_2SO_4 : H_2O_2 . Since the oxidizing effect of the hydrogen dioxide is short lived, the mixture was used immediately after the sulfuric acid was added. Finally, the two metal masking layers were stripped with Aqua Regia and CR7.

The results of the PYREX patterning process were acceptable; however, it was not possible to visually document this in the thesis because there were no working cameras in TRL at the time of this research. Instead, microscopic inspections of the bushings were done before proceeding to the next step in the process to ensure the quality of the bushings.

4.2.3 Step 3: Aluminum pattern

Step 2 was carried out on the first waferset that was received from the wafer manufacturer; four wafers in all. Because there was a significant delay in the delivery time, these wafers were the only ones patterned as driven elements, whereas seven wafers were patterned as sensing elements once the other wafers were received. The glass pattern was created on the driven elements first, and then the aluminum pattern (**RE**) was created. After carrying out the same cleaning procedure as in Step 2, the wafers for the sensing elements were introduced into the process at the beginning of the aluminum step (Step 3). The process results from this step are presented only for the **SE** patterned wafers (sensing elements).

The procedure to pattern the aluminum electrodes is shown in Figure 4-17. The first step was an e-beam deposition of $1\mu\text{m}$ of Al. The layer was deposited at $1000\frac{\text{A}}{\text{s}}$ for 17 minutes. Section 4.2.2 discusses the full e-beam deposition procedure. The results varied between good quality layers for the sensing element wafers to only moderate quality layers for the driven element wafers. The lower quality results were obtained because the bushings on the driven wafers obstructed the uniform deposition process.

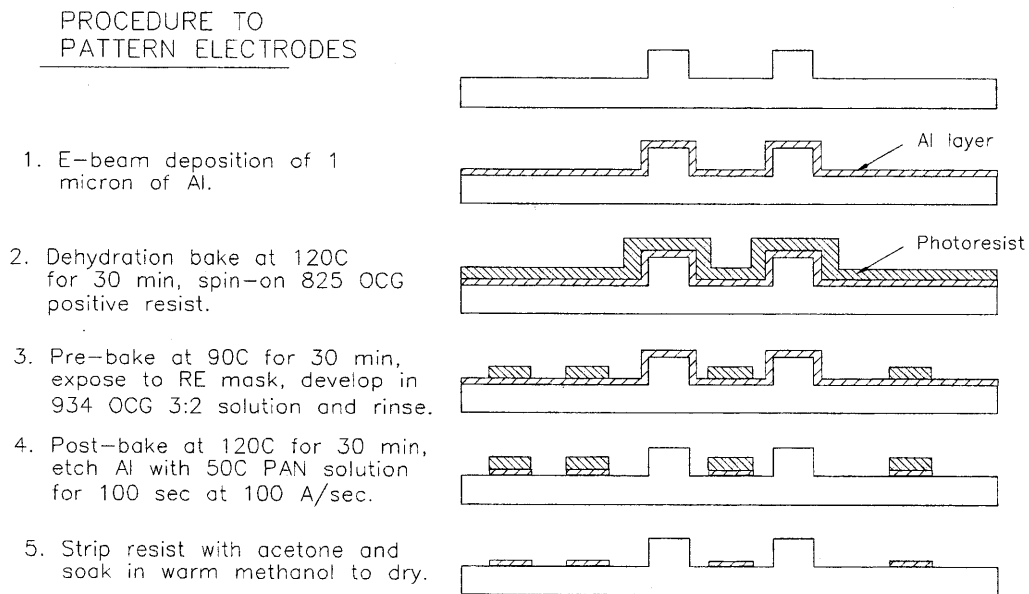


Figure 4-17: Procedure for patterning the aluminum layer

After a dehydration bake for 30 minutes at 120°C , 825 OCG positive resist was spun onto the aluminum layer. The results were identical to the e-beam deposition results: the resist layer quality was excellent for the sensing element wafers, but the bushings on the driven element wafers blocked the uniform spread of resist. This blockage caused streaking on the driven wafers; however, since the electrodes in the RE pattern were in the center of the three bushings, the streaking did not seem to affect the remaining steps in the aluminum patterning procedure.

Next, the pre-bake, expose, develop, and rinse photo step was performed for the SE and RE patterns. The intricacy of the interconnect structure made this process

challenging. Section 4.2.2 gives a detailed account of the procedural techniques in the process. Microscopic inspections were key to creating high quality patterns in the resist, since the interconnects and electrodes were impossible to see without magnification. Modulated sidewalls were the only non-ideal characteristic of the patterned resist. Figure 4-18 illustrates the phenomena. When the resist layer was exposed to

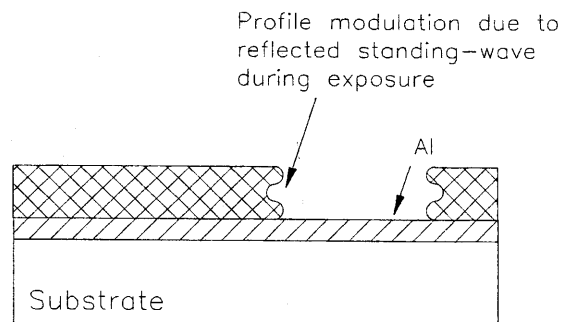


Figure 4-18: Modulated resist sidewalls due to the high reflectivity of an aluminum layer

the mask pattern, the light was reflected off the aluminum layer, back towards the approaching wave. The two waves interfered with one another to create a standing wave, which modulated the resist solubility along the side walls. This did not significantly alter the accuracy of the patterns in this research because the patterns were relatively coarse. The profile modulation would only distort patterns with resolutions on the order of 0.5 to $1.0\mu m$.

The post-bake and aluminum etch were carried out after the photo step. A pre-mixed PAN etchant (phosphoric, acetic, nitric acids) was heated to $50^{\circ}C$ for an etch rate of $100\frac{A}{s}$. Since the aluminum layer was $1\mu m$ thick, the approximate time to etch was 100 seconds. When operated at the manufacturer's suggested temperature of $50^{\circ}C$, the etch lasted anywhere from 98 to 102 seconds. A three minute rinse process was conducted after the etch was completed.

The SE aluminum pattern on the PYREX wafer is shown in Figure 4-19. Note

that this is the same as the pattern on the chrome photomask in Figure 4-12.

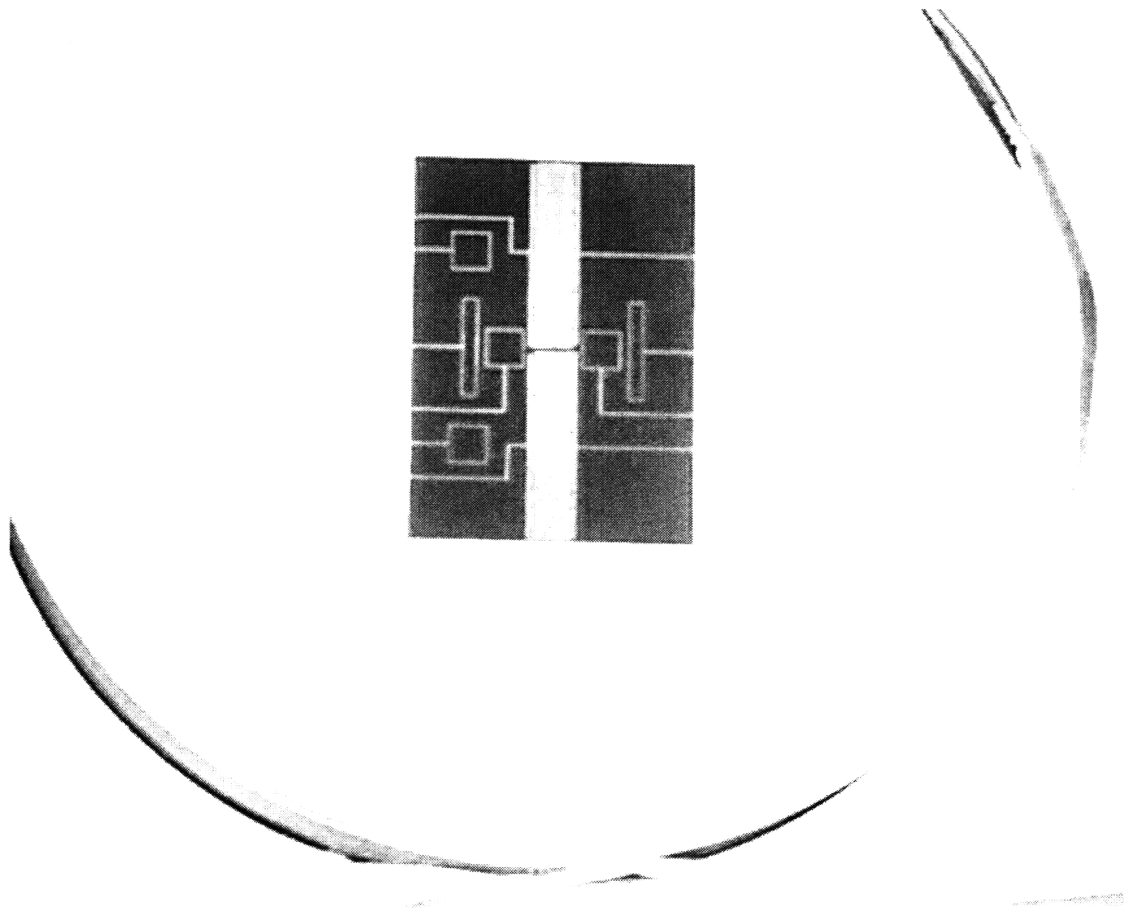


Figure 4-19: PYREX wafer with SE aluminum electrode pattern

SEM characterization

Several SEM images are shown in Figures 4-20 through 4-23. Figure 4-20 shows the electrode and interconnect structure in the center of the SE pattern at 23X magnification. The electrodes are $200\mu m$ wide; the interconnects are $8\mu m$ wide. The patterns are clearly visible at this magnification. Figure 4-21 shows a split-screen image of the same pattern at a higher magnification.

The image of the SE aluminum pattern in Figure 4-22 is shown at 200X magnification. A piece of human hair, $45\mu m$ in diameter, was placed on top of the sensing structure to illustrate the relative size of the HCLPM. Note that the interconnects are much thinner than the hair. A 1000X image in Figure 4-23 shows the relative

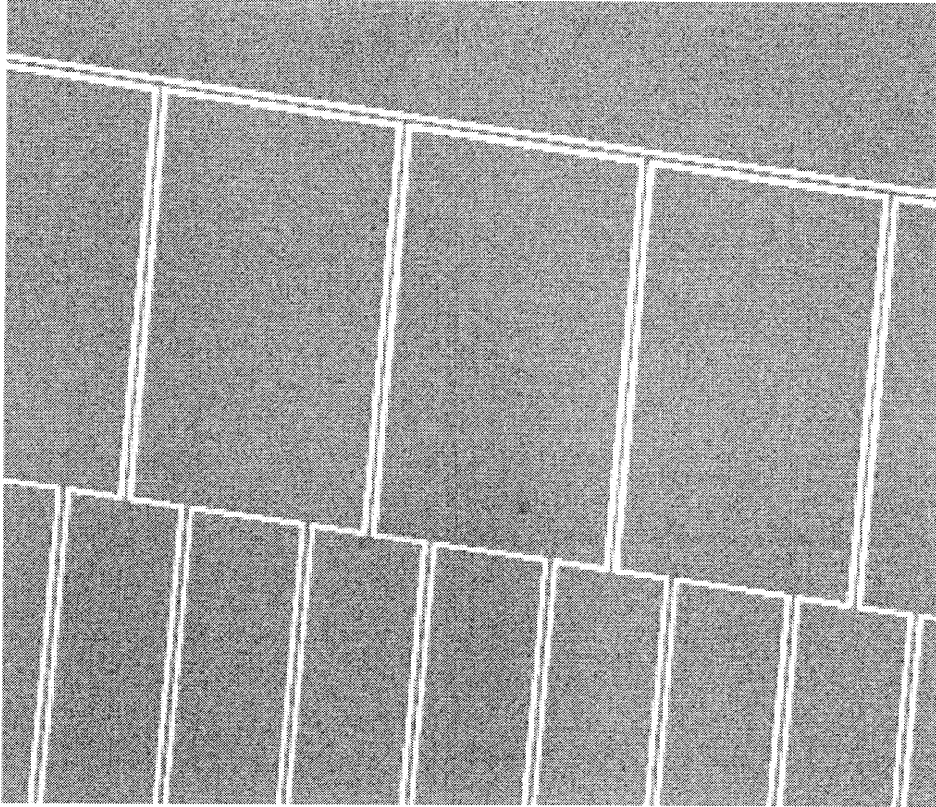


Figure 4-20: SEM image of consecutive electrodes in the sensing electrode pattern

size of an interconnect "T" and a piece of hair. Although this area of the structure was difficult to produce repeatedly, it was not the most difficult. In accordance with Section 4.1.5, Figure 4-24 shows the most intricate areas in the pattern, the long, thin interconnects.

Finally, Figure 4-25 shows one of the aluminum electrical pads; it is $200\mu m \times 200\mu m$ in size. Wire bonding from the contact pad to a buffer operational amplifier is scheduled to be performed prior to testing the sensor.

4.2.4 Step 4: Silicon dioxide pattern

The SiO_2 patterning process is almost identical to the aluminum patterning process (see Figure 4-27). The only differences are in the layer material, layer thickness, and etching process. First, 400A of silicon dioxide was deposited with an e-beam process. After the wafers were immersed in HMDS prime to promote adhesion, the resist was

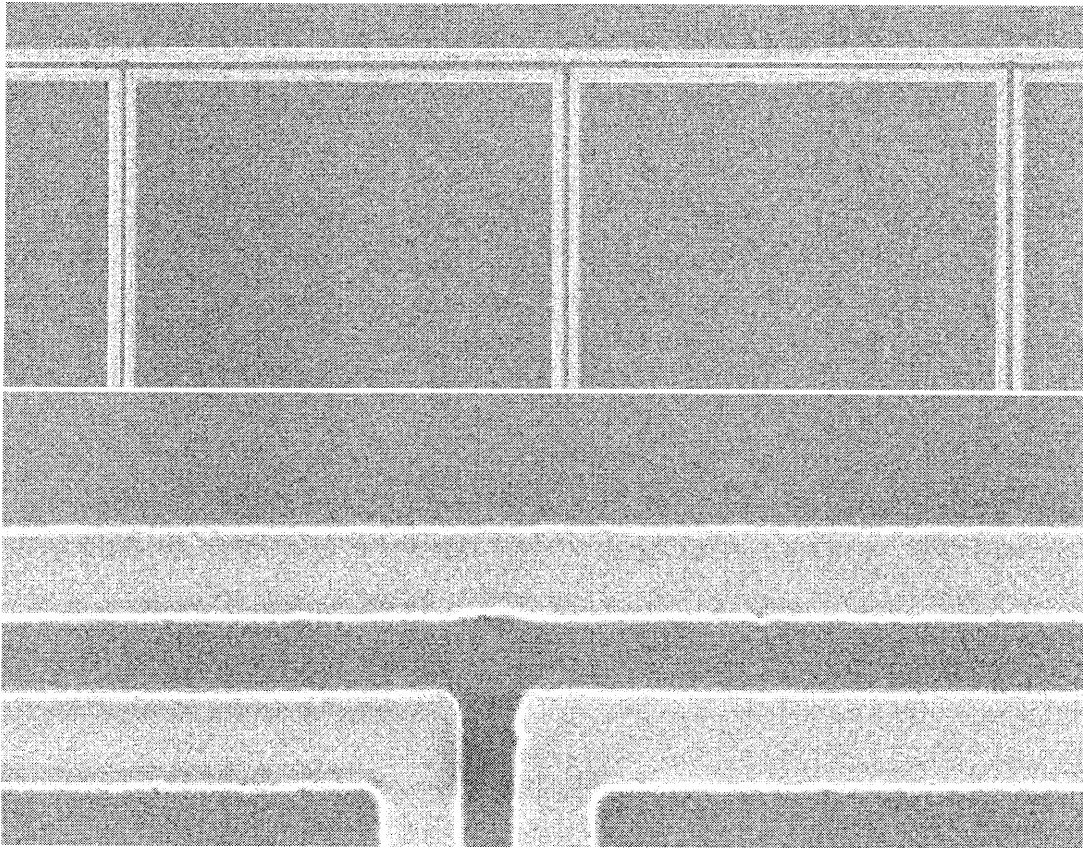


Figure 4-21: Split-screen SEM showing low and high magnification image of the electrode structure

spin-coated, pre-baked, exposed and developed. The exposure was slightly different from the **GD**, **SE**, and **RE** exposures because the passivation patterns had to be aligned to the preceding patterns. The basic alignment structure is shown in Figure 4-26. After the center "+" was patterned into the aluminum layer, the hatched region on the **SP** mask was used to position the contact pattern.

After post-baking the resist, a dry etch RIE process was used to cut through the SiO_2 layer to form the contacts. The Plasmaquest RIE etcher used a CF_4 chemistry to initiate a highly volatile reaction to produce SiF_4 . The incoming electrons liberated a fluorine radical from the CF_4 , which etched the silicon dioxide.

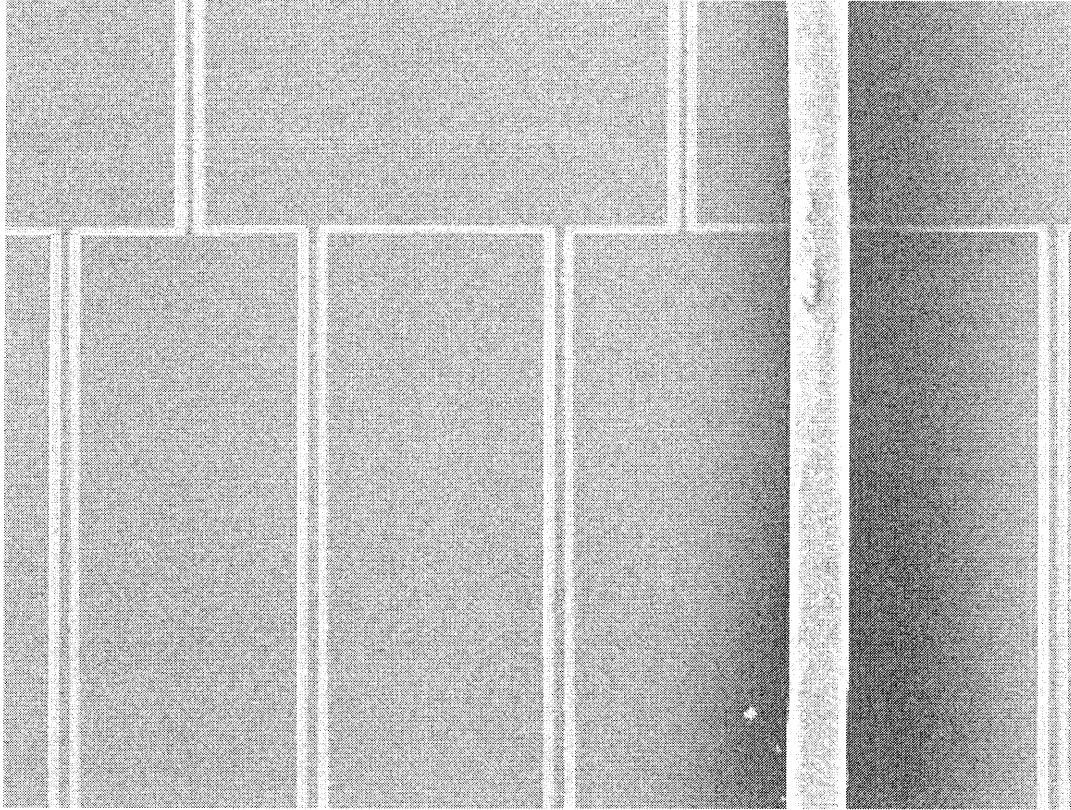


Figure 4-22: SEM image showing relative size of human hair diameter ($50\mu m$), interconnect width ($7\mu m$), and electrode width ($200\mu m$)

4.3 Summary of fabrication

The fabrication process for this research project was extremely involved. The sensing element and the driven element, two electrode and interconnect metallization patterns, were both fabricated in the microfabrication facilities at TRL. This chapter has summarized the HCLPM process, which began with a comprehensive study of the available processes at MTL; it went on to discuss the pattern design layouts and contact photomasks, and then finally reviewed the patterning of the sensing and driven elements. The various iterative sub-processes including e-beam deposition, optical lithography, and wet and dry chemical etching were also discussed. Through visual inspection with a SEM, the results of the process were shown to be of high quality.

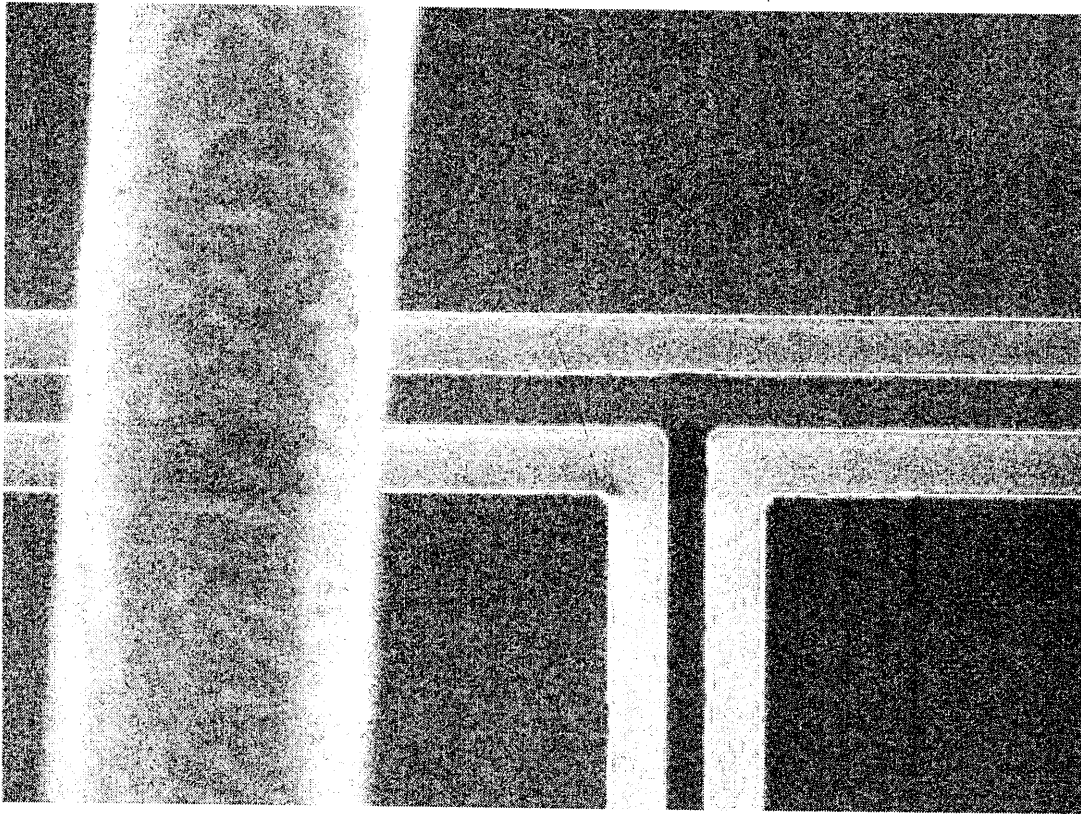


Figure 4-23: SEM image of interconnect "T" and human hair

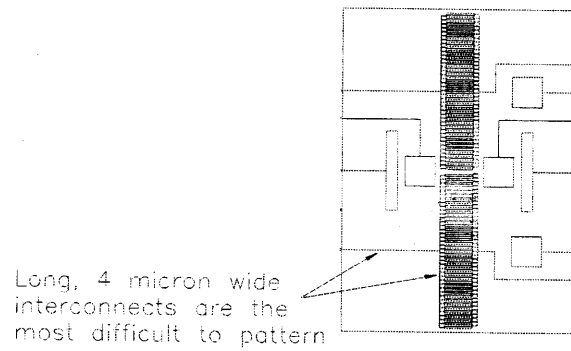


Figure 4-24: Diagram showing long, thin interconnect pathways

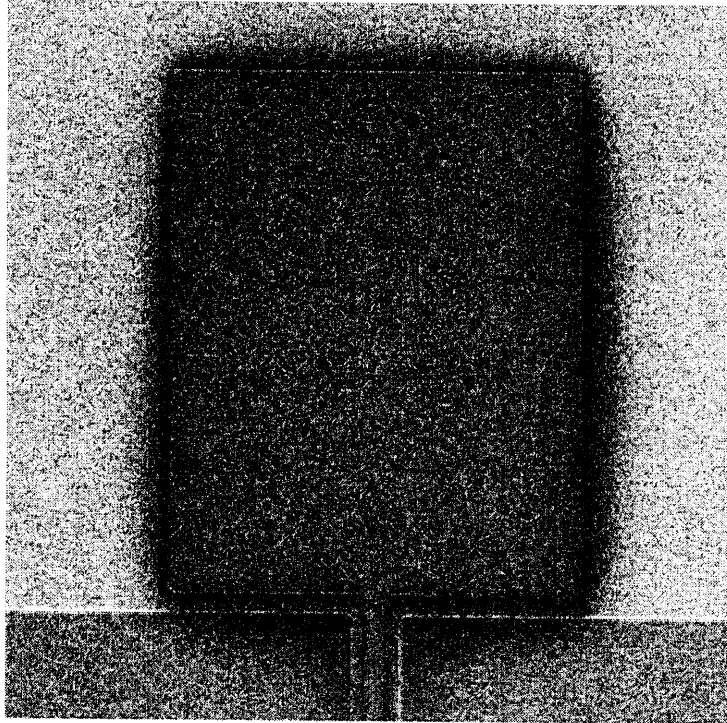


Figure 4-25: SEM image of contact pad in SE pattern

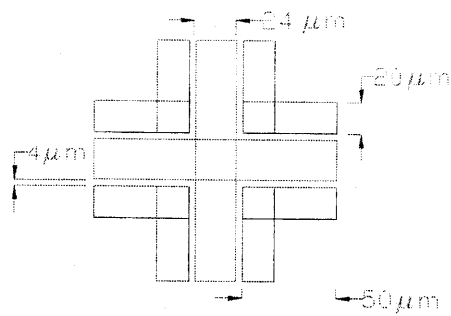


Figure 4-26: Alignment marks for SP layer relative to SE layer

PROCEDURE TO
PATTERN CONTACTS

1. E-beam deposition of 800Å SiO₂

2. HMDS vapor prime at 150C for 25 min, spin-on 825 OCG positive resist.

3. Pre-bake at 90C for 30 min, expose to RP mask, develop in 934 OCG 3:2 solution and rinse.

4. Post-bake at 120C for 30 min, RIE SiO₂ contact with CH₄.

5. Strip resist with ozone asher.

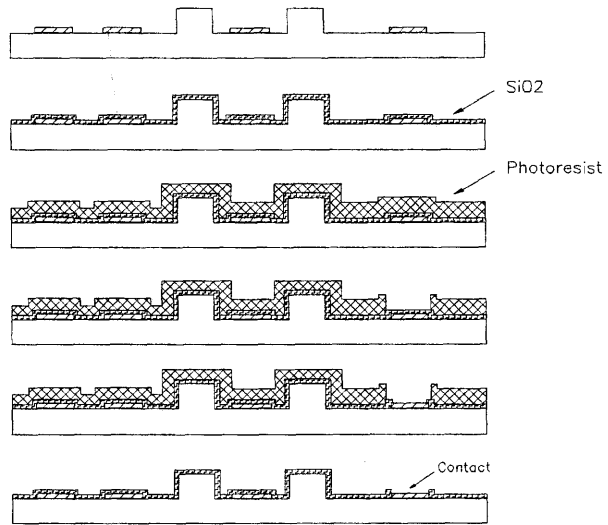


Figure 4-27: Procedure for patterning silicon dioxide layer

Chapter 5

Conclusions and Recommendations

The conception, theory, design, and fabrication of a high resolution capacitance-based lateral position microsensors (HCLPM) were discussed in this thesis. The existing designs were summarized, and an improved sensor was designed to compensate for the performance disadvantages of those existing sensors. The general theory of electrostatics helped to identify both the key performance issues and ways to boost performance. After completing the HCLPM design layouts, a microfabrication process was developed and carried out to build the prototype sensor.

The next phase of the research should focus on readying the sensor for experimentation by assembling a hybrid circuit which communicates with the driven and sensing elements. The general concept is shown in Figure 5-1. The system in the figure corresponds to the hybrid network, which was discussed in Section 3.3.2 (see Figure 3-21). Al-Al ultrasonic bonding is used to connect the sensing pads to the operational buffer amplifiers on the perforated circuit board. Conducting copper strips are attached to the board to carry the input and output signals from one place to another. This setup aims to minimize parasitic capacitances across the leads, while simultaneously avoiding the high cost and time it would take to design and build a printed circuit board.

Once the experimental setup has been established, testing of the sensor can begin.

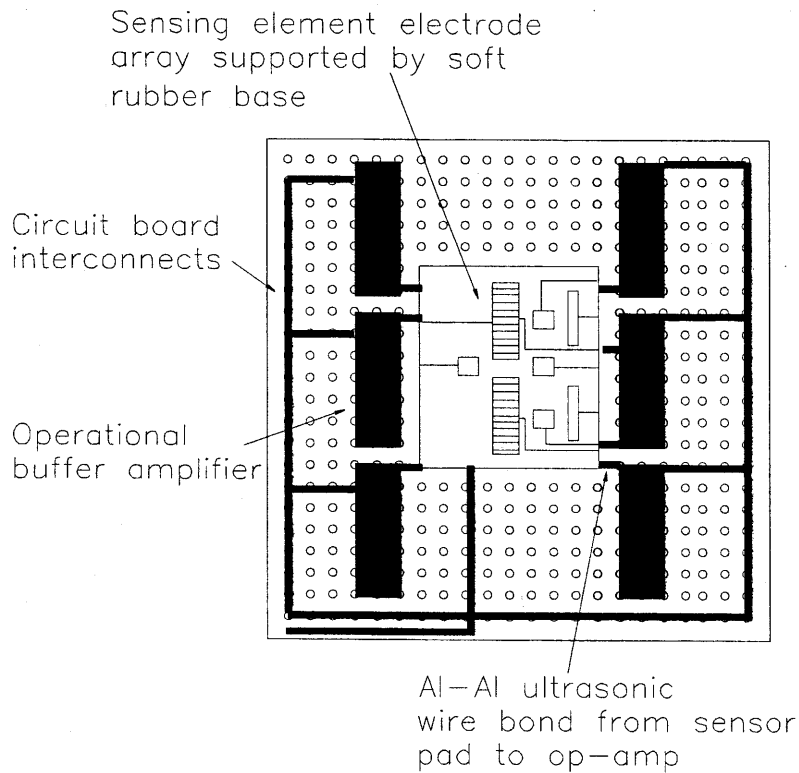


Figure 5-1: Hybrid experimental sensing configuration on circuit board with copper interconnects

The differential signals from the monitor electrodes will allow a complete characterization of the lateral sensing abilities of the HCLPM. Although the results of these tests will prove that the HCLPM works as it was designed to work, the highest resolutions (approaching $10nm$) will require integrated buffer amplifiers in the form of CMOS transistors. This will enable the HCLPM to out-perform all of the existing high resolution position sensors.

Appendix A

Matlab scripts

A.1 rectube.m

```
% First iteration on potential distribution  
% inside rectangular tube  
Ni=20;  
Nc=20;  
%  
a1=20;  
b1=2;  
V_in=5;  
coll=linspace(0.5,0.8,63)';  
c=[coll coll coll];  
%  
x1=linspace(0,a1,Nc);  
y1=linspace(0,b1,Nc);  
n=1:2:Ni*2;  
%  
for i=1:Nc;  
  for j=1:Nc;  
    phix_yv1= (sin(n*pi*x1(j)/a1).*sinh(n*pi*y1(i)/a1)  
              ./ (n.*sinh(n*pi*b1/a1)));  
    phix_y1(j,i) = (4*V_in/pi)*sum(phix_yv1);  
  end
```

10

20

```

end
[gx1,gy1]=gradient(phix_y1',x1(2)-x1(1),y1(2)-y1(1));
%
figure(1);
surf(x1,y1,phix_y1');
colormap(c);
axis([0 a1 0 b1 0 5]);
colorbar;
xlabel('Normalized x');
ylabel('Normalized y');
zlabel('Potential (V)');
figure(2);
quiver(x1,y1,gx1,gy1);
% Second set of a/b values
a1=20;
b1=12;
x2=linspace(0,a1,Nc);
y2=linspace(0,b1,Nc);
for i=1:Nc;
for j=1:Nc;
    phix_yv2= (sin(n*pi*x2(j)/a1).*sinh(n*pi*y2(i)/a1))
                ./ (n.*sinh(n*pi*b1/a1));
    phix_y2(j,i) = (4*V_in/pi)*sum(phix_yv2);
end
end
[gx2,gy2]=gradient(phix_y2',x2(2)-x2(1),y2(2)-y2(1));
%
figure(3);
surf(x2,y2,phix_y2');
colormap(c);
axis([0 a1 0 b1 0 5]);
colorbar;
xlabel('Normalized x');
ylabel('Normalized y');
zlabel('Potential (V)');
figure(4);

```

```
quiver(x2,y2,gx2,gy2,3);
```

A.2 numlap.m

```
% Numerical solution for Laplace's equation
```

```
%
```

```
% Define resolution
```

```
clear;
```

```
% No. of rows
```

```
n=100; % No. of columns
```

```
m=(2/20)*n; % No. of columns
```

```
% Set up basis matrices
```

```
B=(-4)*eye(n);
```

```
B(1,2)=1;
```

10

```
B(n,n-1)=1;
```

```
for i = 2:(n-1),
```

```
    B(i,i-1)=1;
```

```
    B(i,i+1)=1;
```

```
end
```

```
I=eye(n);
```

```
A=zeros(m*n);
```

```
% Generate equation matrices
```

```
A(1:n,1:n)=B;
```

```
A(1:n,n+1:2*n)=I;
```

20

```
A(m*n-(n-1):m*n,m*n-(2*n-1):m*n-n)=I;
```

```
A(m*n-(n-1):m*n,m*n-(n-1):m*n)=B;
```

```
for i = 2:m-1;
```

```
    A((i-1)*n+1:(i-1)*n+n,(i-1)*n+1-n:(i-1)*n)=I;
```

```
    A((i-1)*n+1:(i-1)*n+n,(i-1)*n+1:(i-1)*n+n)=B;
```

```
    A((i-1)*n+1:(i-1)*n+n,(i-1)*n+1+n:(i-1)*n+2*n)=I;
```

```
end
```

```
% Set boundary conditions (right-hand side b vector)
```

```
% Bottom electrode BC's
```

```
left=0;
```

30

```
bottom=0;
```

```

topv=5;
top0=0;
right=0;
%
b(1)=left+bottom;
for j = 2:(n-1),
    b(j)=bottom;
end
b(n)=bottom+right;
%
for j = m*n-(n-1):m*n-4*(n/5),
    b(j)=topv;
end
for j = m*n-4*(n/5)+1:m*n-3*(n/5),
    b(j)=top0;
end
for j = m*n-3*(n/5)+1:m*n-2*(n/5),
    b(j)=topv;
end
for j = m*n-2*(n/5)+1:m*n-1*(n/5),
    b(j)=top0;
end
for j = m*n-1*(n/5)+1:m*n,
    b(j)=topv;
end
%
for i = n+1:m*n-n,
    b(i)=left; % or right in this particular set of BC's
end
b=(-1)*b';
% Solve the set of equations
u=inv(A)*b;
% Sort solution vector
for i = 1:m,
    for j = 1:n,
        phi(i,j)=u((i-1)*n+j);
    end
end

```

```

    end
end
% Plot results
x=linspace(0,20,n);
y=linspace(0,2,(2/20)*n);
figure(1);
meshc(x,y,phi);
colormap(c);

```

70

A.3 tiltsol.m

```

% Tilt equations for capacitance
e_o=8.85e-12;
w=7*0.2e-3;
L=0.2e-3;
g_mean=(0.2)*(1e-4);
g_mean2=(0.1)*(1e-4);
N=50;
phio=linspace(-5*pi/180,5*pi/180,N);
Cmean=diag(eye(50))*e_o*w*L/g_mean;
% Calculate capacitance
% C_nobend=
C_nobend=(e_o*w./(tan(phio))).*log((g_mean+(L/2).*sin(phio))
    ./(g_mean-(L/2).*sin(phio)));
C_nobend2=(e_o*w./(phio)).*log((g_mean2+(L/2).*sin(phio))
    ./(g_mean2-(L/2).*sin(phio)));
C_bend=(e_o*w./phio)*log(L/(0.01*L));
M1=L*g_mean*tan(phio).*cos(phio);
M2=g_mean^2-((L^2)/4)*((sin(phio)).^2);
M3=((sec(phio)).^2).*log((g_mean+(L/2).*sin(phio))
    ./(g_mean-(L/2).*sin(phio)));
M4=(tan(phio)).^2;
S_t=e_o*w*((M1./M2)-M3)./M4;
% Plot results
figure(1);

```

10

20

```

plot(phia*180/pi,C_nobend/(e_o*w*L/g_mean),phia*180/pi,
     C_nobend2/(e_o*w*L/g_mean2),'--')
xlabel('Tilting Angle (deg)');
ylabel('Normalized Capacitance C_tilt/C_mean')
text(-2.5,1.5,'_ For aspect ratio a/b=10');
text(-2.5,1.45,'---- For aspect ratio a/b=20');
fit=polyfit(phia((N/2)-(N/10):(N/2)+(N/10)),S_t((N/2)-(N/10):
          (N/2)+(N/10)),1);
p=fit(1)*phia+fit(2);
figure(2);
plot(phia*180/pi,S_t/(e_o*w*L/g_mean),phia*180/pi,p/
     (e_o*w*L/g_mean),'--')
xlabel('Tilting Angle (deg)');
ylabel('Norm. Sens. S_t/C_mean (fraction of C_mean/deg)');
text(-4.5,1.5,'_ S_t/C_mean full solution');
text(-4.5,1.2,'---- S_t/C_mean small angle L.S. approx.');
```

30

40

A.4 allsens.m

```

% Sensitivity ratios for the various
% modes of displacement
e_o=8.85e-12;
w=5e-3;
L=5e-3;
L1=5e-3;
L2=1e-3;
L3=0.2e-3;
g_mean=1e-4;
phia=linspace(0.01*pi/180,5*pi/180,50);
Cmean=diag(eye(50))*e_o*w*L/g_mean;
% Calculate capacitance
C_nobend=(e_o*w./(phia)).*log((g_mean+(L/2).*sin(phia))
    ./(g_mean-(L/2).*sin(phia)));
C_bend=(e_o*w./phia)*log(L/(0.01*L));
M1=L*g_mean*phia.*cos(phia);
```

10


```

M2=g_mean^2-((L^2)/4)*((sin(phio).^2));
M3=log((g_mean+(L/2).*sin(phio))./(g_mean-(L/2).*sin(phio)));
M4=phio.^2;
% Plot results
plot(phio*180/pi,C_nobend/(e_o*w*L/g_mean),phio*180/pi,
      Cmean/(e_o*w*L/g_mean))
un=ones(size(phio));
g_mean=linspace(1e-5,1e-4,40);
S_t1=zeros(50,40);
for i=1:50,
    for j=1:40,
        S_t1(i,j)=phio(i)*(e_o*w*L^2)./(6*(g_mean(j)^2));
    end
end
end
S_l1=(e_o*w./g_mean);
S_l2=S_l1;
S_l3=e_o*w./g_mean;
surf(g_mean*1000,phio*180/pi,log(S_t1));
colormap(cool);
view([-17 32]);
xlabel('g_mean (mm)');
ylabel('Tilt (deg)');
zlabel('Sensitivity Ratio S_t/L*S_l');

```

20

30

Appendix B

PFR code

B.1 cap-sense.fl

```
(fl-load "/usr/cafepfr/lib/lib-loc.fl")
(fl-load "/homes/deadams/pfr/loc_lib/lib/more-bindings.fl")
(fl-load "/homes/deadams/pfr/loc_lib/lib/more-utils.fl")
(fl-library "/homes/deadams/pfr/loc_lib")
(fl-library :database)
(fl-load "/usr/cafepfr/lib/utils.fl")
(fl-load "/usr/cafepfr/lib/constants.fl")
(fl-load "/homes/deadams/pfr/loc_lib/dea_masks.fl")
```

10

```
(define cap-sense
  (flow
    (:doc "Pyrex etch and metal deps")
    (:version
      (:modified :number 1.0 :by "Douglas E. Adams" :date "Oct. 1, 1996"
        :what "Create PFR"))
    (:body
      (operation
        (:wafers ("10a"))
        (pyrex-clean-op)
```

20

```

(ebeam-dep-aucr)
(multi-expose-mask :mask-a GD :mask-id-a "GD")
(metal-wet-etch :metal "Au" :solution "Aqua Regia (3:1 HCl:HNO3)"
  :thick-A 1000
  :instruction "Let sit 1 min before using; etch 30s (15s to clear)")
(metal-wet-etch :metal "Cr" :solution "CR7 Chrome etchant"
  :thick-A 200
  :instruction "Takes approx 10s")
(pyrex-wet-etch)
resist-ash 30
(metal-strip :metal "Au" :solution "Aqua Regia (3:1 HCl:HNO3)"
  :thick-A 1000
  :instruction "Strip-Let sit 1 min before using; etch 30s (15s to clear)")
(metal-strip :metal "Cr" :solution "CR7 Chrome etchant"
  :thick-A 200
  :instruction "Strip completely: takes approximately 10s"))
(operation
  (:wafers ("10a,10b"))
  (pyrex-clean-op)
  (ebeam-dep-alum) 40
  (photo-step-trl :mask-a RE :mask-id-a "RE"
    :mask-b SE :mask-id-b "SE")
  (metal-wet-etch :metal "Al"
    :solution "PAN--16:1:1:2 Phos-Acet-Nitr acid + DI"
    :thick-A 10000
    :instruction "Test will determine etch-rate control")
  resist-ash
  (ebeam-dep-sio2)
  (photo-step-trl :mask-a RP :mask-id-a "RP"
    :mask-b SP :mask-id-b "SP") 50
  (rie-pa-sio2-trl)
  resist-ash)
)))

```

B.1.1 more-bindings.fl

```
;;; Bindings for cap-sens.fl, lateral capacitance-based position sensor
```

```
;;; Author:      Douglas E. Adams, Mech Eng
```

```
;;; Date:       October 1996
```

```
;;;
```

```
(define StandardResistTRL "OCG 825-20 cSt. safe resist")
```

```
(define pyrex-clean-op      trl-piranha)
```

```
(define rie-pa-sio2-trl    rie-sio2)
```

```
(define spin-on-stand-resist  spin-on-res)
```

```
(define multi-expose-mask   trl-mexp-ph)
```

```
(define photo-step-trl      trl-photo)
```

10

```
(define ebeam-dep-alum      ebeamal)
```

```
(define ebeam-dep-aucr      ebmcrau)
```

```
(define ebeam-dep-sio2      ebmsio2)
```

```
(define metal-wet-etch      etch-metal)
```

```
(define metal-strip         metstr)
```

```
(define pyrex-wet-etch      pyretch)
```

B.1.2 pyretch.fl

```
(define (pyretch)
```

```
  (flow
```

```
    (:doc "Etch Pyrex glass wafer patterns.")
```

```
    (:version
```

```
      (:modified :number 1.0 :by "Duane Boning" :date "February 28, 1989"
```

```
        :what "Write operation in flow language")
```

```
      (:modified :number 1.1 :by "Duane Boning" :date "March 25, 1989"
```

```
        :what "Made time-required the sum of the body times"))
```

```
    (:advice (:opset "pyretch" :name "PYREX-WET-ETCH"))
```

```
    (:time-required (:hours 4))
```

10

```
    (:body
```

```
      (etchgls :glass "Pyrex"
```

```
        :solution "660ml H2O:140ml HF:200ml HNO3 = 1L"
```

```
        :thick-m 30
```

```
        :instruction "Use a stir bar (NO ultrasonic); 0.7-0.8mic/min"))))
```

B.1.3 more-utils.fl

```
;;; Bindings for cap-sens.fl, lateral capacitance-based position sensor
;;; Author: Douglas E. Adams, Mech Eng
;;; Date: October 1996
;;;

;;;
;;; Piranha operation
;;;
(define (tpiranha)
  (operation
    (:advice (:name "TPIRANHA"))
    (:time-required (:hours 1))
    (:machine "acid-hood")
    (:instructions . (|"piranha strip (3:1 H2SO4:H2O2) \\nl Step 1a
: pour 200ml peroxide first, then 600ml sulfuric acid. \\nl Step 1b: strip for 2 min, rinse, transfer to prime boat and spin dry.
\\nl Step 2a: 20 s Boe dip. \\nl Step 2b: measure on prometrix."))))
    10

;;;
;;; RIE etch operation for SiO2
    20
;;;
(define (riesio2)
  (operation
    (:advice (:name "RIESIO2"))
    (:change-wafer-state
    (:etch :material "SiO2"
      :thickness (:angstroms (:mean 3000 :range 100))))
    (:machine "pecvd-rie")
    (:instructions "Joe will help with settings; **Add PI cure test wafer**")
    (:time-required (:hours 2 :minutes 30))))
    30
```

```

;;;
;;; Spin-on resist operation
;;;
(define (spintrl (resist :type string :default StandardResistTRL))
(operation
  (:advice (:name "SPINTRL"))
  (:change-wafer-state (:deposit :material resist))
  (:machine "coater")
  (:settings :material resist)
  (:time-required (:minutes 50))))
40

;;;
;;; E-beam deposition operation for 1 material
;;;
(define (depebm1 (material1 :type string)
  (layer1 :type integer)
  (instruction :type string))
50

  (generic-ebeam-dep1 :material1 material1
    :mean1-A layer1
    :range1-A 10
    :machine "e-beam"
    :instruction instruction
    :readings (:exposure "Pressure")
    :opset "depebm1"
    :name "DEPEBM1"))
60

;;;
;;; E-beam deposition operation of 2 materials
;;;
(define (depebm2 (material1 :type string)
  (layer1 :type integer)
  (material2 :type string)
  (layer2 :type integer)
  (instruction :type string))

```

```

(generic-ebeam-dep2 :material1 material1                                70
    :mean1-A layer1
    :range1-A 10
    :material2 material2
    :mean2-A layer2
    :range2-A 10
    :machine "e-beam"
    :instruction instruction
    :readings (:exposure "Pressure")
    :opset "depebm2"
    :name "DEPEBM2"))                                            80

;;;
;;;
;;;
(define (generic-ebeam-dep2 (material1 :type string)
    (mean1-A :type integer)
    (range1-A :type integer)
    (material2 :type string)
    (mean2-A :type integer)
    (range2-A :type integer)
    (machine :type string)
    (instruction :type string)
    (readings :type integer)
    (opset :type string)
    (name :type string :default "GENERIC-EBEAM-DEP2")))
                                                                    90

(flow
  (:doc "Generic E-Beam Deposition Opset: 2 materials.")
  (:version
    (:modified :number 1.0 :by "Greg Fischer" :date "December 9, 1992"
      :what "Provided for generic and specific opsets"))
    100
  (:advice (:opset opset :name name))
  (:permissible-delay :minimal)
  (:body
    (operation
      (:advice (:name "DEPOSIT-MATERIAL2"))

```

```

(:change-wafer-state
  (:deposit :material material1
    :thickness (:angstroms (:mean mean1-A :range range1-A)))
  (if material2
    (:deposit :material material2
      :thickness (:angstroms (:mean mean2-A :range range2-A))))
  (:machine machine)
  (:instructions instruction)
  (:readings (if readings readings))))))

;;;
;;; Metal etch operation
;;;
(define (etchmet (metal :type string)
  (solution :type string)
  (thick-A :type integer)
  (instruction :type string))
  (operation
    (:advice (:opset "etchmet" :name "ETCHMET"))
    (:change-wafer-state (:etch :material metal
      :thickness (:angstroms thick-A)))
    (:machine "acid-hood")
    (:instructions instruction)
    (:settings :acid solution
      :temperature-C 40 :time (:seconds 120))))))

;;;
;;; Glass etch operation
;;;
(define (etchgls (glass :type string)
  (solution :type string)
  (thick-m :type integer)
  (instruction :type string :default " "))
  (operation
    (:advice (:opset "etchgls" :name "ETCHGLS"))

```



```
(:time-required (:hours 4))
(:change-wafer-state (:etch :material glass
                      :thickness (:microns thick-m)))
(:machine "acid-hood")
(:instructions instruction)
(:settings :acid solution
           :temperature-C 20 :time (:seconds 14400))))
```

```
;;;
;;;
;;;
```

150

B.1.4 dea_masks.fl

```
(define GD (:mask ("GD")      :mask-name "GD"))
(define RE (:mask ("RE")      :mask-name "RE"))
(define RP (:mask ("RP")      :mask-name "RP"))
(define SE (:mask ("SE")      :mask-name "SE"))
(define SP (:mask ("SP")      :mask-name "SP"))
```

B.1.5 ebeamal.fl

```
(define (ebeamal)
  (flow
   (:doc "Deposit 1 micron Al layer with E-beam in TRL.")
   (:version
    (:modified :number 1.0 :by "Duane Boning" :date "February 28, 1989"
              :what "Write operation in flow language")
    (:modified :number 1.1 :by "Duane Boning" :date "March 25, 1989"
              :what "Made time-required the sum of the body times")))
   (:advice (:opset "ebeamal" :name "EBEAM-DEP-ALUM"))
   (:time-required (:hours 1 :minutes 45))
   (:body
    (depebm1 :material1 "Al"
             :layer1 10000
             :instruction "Must perform ozone clean before"))))
```

10

B.1.6 ebmcrau.fl

```
(define (ebmcrau)
  (flow
    (:doc "Deposit Au and Cr layers with E-beam in TRL.")
    (:version
      (:modified :number 1.0 :by "Duane Boning" :date "February 28, 1989"
        :what "Write operation in flow language")
      (:modified :number 1.1 :by "Duane Boning" :date "March 25, 1989"
        :what "Made time-required the sum of the body times"))
    (:advice (:opset "ebmcrau" :name "EBEAM-DEP-AUCR"))
    (:time-required (:hours 1 :minutes 45))
    (:body
      (depebm2 :material1 "Cr"
        :layer1 200
        :material2 "Au"
        :layer2 1000
        :instruction
        "Perform 1hr oz after piranha; P at 5e-7 torr; Cr--1.5A/s,Au--3.0A/s")
      )))
```

B.1.7 ebmsio2.fl

```
(define (ebmsio2)
  (flow
    (:doc "Deposit 3000A SiO2 layer with E-beam in TRL.")
    (:version
      (:modified :number 1.0 :by "Duane Boning" :date "February 28, 1989"
        :what "Write operation in flow language")
      (:modified :number 1.1 :by "Duane Boning" :date "March 25, 1989"
        :what "Made time-required the sum of the body times"))
    (:advice (:opset "ebmsio2" :name "EBEAM-DEP-SIO2"))
    (:time-required (:hours 1 :minutes 45))
    (:body
      (depebm1 :material1 "SiO2"
        :layer1 3000
```

```
:instruction "Ozone clean prior to deposition; use dehy-bake"))))
```

B.1.8 etch-metal.fl

```
(define (etch-metal (metal :type string)
  (solution :type string)
  (thick-A :type integer)
  (instruction :type string :default " "))
  (flow
  (:doc "Wet etch of metal layer in TRL.")
  (:version
  (:modified :number 1.0 :by "Duane Boning" :date "February 28, 1989"
    :what "Write operation in flow language")
  (:modified :number 1.1 :by "Duane Boning" :date "March 25, 1989"
    :what "Made time-required the sum of the body times"))
  (:advice (:opset "etch-metal" :name "METAL-WET-ETCH"))
  (:time-required (:hours 2))
  (:body
  (etchmet :metal metal :solution solution :thick-A thick-A
    :instruction instruction))))
```

10

B.1.9 gen-trl-photo.fl

```
(define (gen-trl-photo (mask-a :type symbol)
  (mask-b :type symbol)
  (mask-id-a :type string)
  (mask-id-b :type string)
  (prime? :type symbol :default :t)
  (coat? :type symbol :default :t)
  (prebake? :type symbol :default :t)
  (expose? :type symbol :default :t)
  (develop? :type symbol :default :t)
  (inspect1? :type symbol :default :f)
  (postbake? :type symbol :default :t))
```

10

```

        (inspect? :type symbol :default :t)
        (opset :type string)
        (name :type string)
        (time-required-sec :type integer))
(flow
 (:doc "Generic TRL Photo Opset.")
 (:version
  (:modified :number 1.1 :by "Ralph Nevins" :date "February 12, 1996"
   :what "Provide for generic opsets where possible"))
 (:advice (:opset opset :name name))
 (:time-required time-required-sec)
 (:permissible-delay :minimal)
 (:body
  (if (=? prime? :t)
    (HMDS-prime-TRL))
  (if (=? coat? :t)
    (spin-on-res))
  (if (=? prebake? :t)
    (operation
      (:advice (:name "PREBAKE-TRL"))
      (:machine "prebakeovn")
      (:instructions
       "Use Au contaminated boat for 10a wafers.")
      (:settings :temp-C 90 :time "30 minutes")
      (:time-required (:minutes 30))))
  (if (=? expose? :t)
    (flow
      (:advice (:name "RESIST-EXP-TRLAB"))
      (:body
       (operation
        (:advice (:name "RESIST-EXPOSE-TRLB"))
        (:wafers "10b")
        (:change-wafer-state (:expose :mask mask-b))
        (:machine "ksaligner2")
        (:settings :mask-id mask-id-b)
        (:readings :exposure-time "Exposure Time"))
       ))
      ))
  ))

```

```

    (:time-required (:hours 1)))
  (operation
    (:advice (:name "RESIST-EXPOSE-TRLA")) 50
    (:wafers "10a")
    (:change-wafer-state (:expose :mask mask-a))
    (:machine "ksaligner2")
    (:settings :mask-id mask-id-a)
    (:readings :exposure-time "Exposure Time")
    (:time-required (:hours 1))))))
(if (=? develop? :t)
  (operation
    (:advice (:name "RESIST-DEVELOP-TRL"))
    (:change-wafer-state (:develop)) 60
    (:machine "photo-wet")
    (:readings :develop-time "Develop Time")
    (:time-required (:minutes 50))))
(if (=? inspect1? :t)
  (resist-inspect :where "Center Wafer"))
(if (=? postbake? :t)
  (operation
    (:advice (:name "POSTBAKE-TRL"))
    (:machine "postbake")
    (:instructions "Use Au contaminated boat for 10a wafers.") 70
    (:settings :temp-C 120 :time "30 minutes")
    (:time-required (:minutes 30))))
(if (=? inspect? :t)
  (resist-inspect :where "Center Wafer"))))

```

B.1.10 gen-trl-photo10a.fl

```

(define (gen-trl-photo10a (mask-a :type symbol)
  (mask-id-a :type string)
  (prime? :type symbol :default :t)
  (coat? :type symbol :default :t)
  (prebake? :type symbol :default :t)
  (expose? :type symbol :default :t)

```

```

        (develop? :type symbol :default :t)
        (inspect1? :type symbol :default :f)
        (postbake? :type symbol :default :t)
        (inspect? :type symbol :default :t)
        (opset :type string)
        (name :type string)
        (time--required--sec :type integer))
(flow
(:doc "Generic TRL Photo Opset.")
(:version
 (:modified :number 1.1 :by "Ralph Nevins" :date "February 12, 1996"
  :what "Provide for generic opsets where possible"))
(:advice (:opset opset :name name))
(:time--required time--required--sec)
(:permissible--delay :minimal)
(:body
 (if (=? prime? :t)
  (HMDS--prime--TRL))
 (if (=? coat? :t)
  (spin--on--res))
 (if (=? prebake? :t)
  (operation
   (:advice (:name "PREBAKE--TRL"))
   (:machine "prebakeovn")
   (:instructions
    "Use Au contaminated boat for 10a wafers.")
   (:settings :temp--C 90 :time "30 minutes")
   (:time--required (:minutes 30))))
 (if (=? expose? :t)
  (operation
   (:advice (:name "RESIST--MUL--EXPOSE--TRL"))
   (:change--wafer--state (:expose :mask mask--a))
   (:machine "ksaligner2")
   (:instructions "Expose 2sec, wait 4sec, repeat 16 times")
   (:settings :mask--id mask--id--a)
   (:readings :exposure--time "Exposure Time"))

```

```

    (:time-required (:hours 1))))
(if (= ? develop? :t)
  (operation
    (:advice (:name "RESIST-DEVELOP-TRL"))
    (:change-wafer-state (:develop))
    (:machine "photo-wet")
    (:readings :develop-time "Develop Time")
    (:time-required (:minutes 50)))) 50
(if (= ? inspect1? :t)
  (resist-inspect :where "Center Wafer"))
(if (= ? postbake? :t)
  (operation
    (:advice (:name "POSTBAKE-TRL"))
    (:machine "postbake")
    (:instructions "Use Au contaminated boat for 10a wafers.")
    (:settings :temp-C 120 :time "30 minutes")
    (:time-required (:minutes 30))))
(if (= ? inspect? :t) 60
  (resist-inspect :where "Center Wafer"))))

```

B.1.11 generic-ebeam-dep1.fl

```

;;; -*- Mode: Lisp -*-
(define (generic-ebeam-dep1 (material1 :type string)
                            (mean1-A :type integer)
                            (range1-A :type integer)
                            (machine :type string)
                            (instruction :type string)
                            (readings :type integer)
                            (opset :type string)
                            (name :type string :default "GENERIC-EBEAM-DEP1"))
  (flow 10
    (:doc "Generic E-Beam Deposition Opset: 1 material.")
    (:version
     (:modified :number 1.0 :by "Greg Fischer" :date "December 9, 1992"
      :what "Provided for generic and specific opsets"))

```

```

(:advice (:opset opset :name name))
(:permissible-delay :minimal)
(:body
  (operation
    (:advice (:name "DEPOSIT-MATERIAL1"))
    (:change-wafer-state
      (:deposit :material material1
        :thickness (:angstroms (:mean mean1-A :range range1-A))))
    (:machine machine)
    (:instructions instruction)
    (:readings (if readings readings))))))

```

20

B.1.12 generic-ebeam-dep2.fl

```

;;; -*- Mode: Lisp -*-
(define (generic-ebeam-dep2 (material1 :type string)
  (mean1-A :type integer)
  (range1-A :type integer)
  (material2 :type string)
  (mean2-A :type integer)
  (range2-A :type integer)
  (machine :type string)
  (instruction :type string)
  (readings :type integer)
  (opset :type string)
  (name :type string :default "GENERIC-EBEAM-DEP2"))
  (flow
    (:doc "Generic E-Beam Deposition Opset: 2 materials.")
    (:version
      (:modified :number 1.0 :by "Greg Fischer" :date "December 9, 1992"
        :what "Provided for generic and specific opsets"))
    (:advice (:opset opset :name name))
    (:permissible-delay :minimal)
    (:body
      (operation
        (:advice (:name "DEPOSIT-MATERIAL2"))

```

10

20


```

(:change-wafer-state
  (:deposit :material material1
    :thickness (:angstroms (:mean mean1-A :range range1-A)))
  (if material2
    (:deposit :material material2
      :thickness (:angstroms (:mean mean2-A :range range2-A))))))
(:machine machine)
(:instructions instruction)
(:readings (if readings readings))))))

```

30

B.1.13 metstr.fl

```

(define (metstr (metal :type string)
  (solution :type string)
  (thick-A :type integer)
  (instruction :type string :default " "))
  (flow
    (:doc "Strip metal mask in TRL.")
    (:version
      (:modified :number 1.0 :by "Duane Boning" :date "February 28, 1989"
        :what "Write operation in flow language")
      (:modified :number 1.1 :by "Duane Boning" :date "March 25, 1989"
        :what "Made time-required the sum of the body times")))
    (:advice (:opset "metstr" :name "METAL-STRIP"))
    (:time-required (:hours 2))
    (:body
      (etchmet :metal metal :solution solution :thick-A thick-A
        :instruction instruction))))))

```

10

B.1.14 rie-sio2.fl

```

(define (rie-sio2)
  (flow

```

```

(:doc "RIE etch of passivation.")
(:version
  (:modified :number 1.0 :by "Duane Boning" :date "February 28, 1989"
    :what "Write operation in flow language"))
(:advice (:opset "rie-sio2" :name "RIE-PA-SIO2-TRL"))
(:time-required (:hours 2 :minutes 30))
(:body
  (riesio2))))

```

10

B.1.15 spin-on-res.fl

```

(define (spin-on-res)
  (flow
    (:doc "Spin-on resist in TRL.")
    (:version
      (:modified :number 1.0 :by "Duane Boning" :date "February 28, 1989"
        :what "Write operation in flow language"))
    (:advice (:opset "spin-on-res" :name "SPIN-ON-STAND-RESIST"))
    (:time-required (:hours 2 :minutes 30))
    (:body
      (spintrl :resist StandardResistTRL))))

```

10

B.1.16 trl-mexp-ph.fl

```

(define (trl-mexp-ph (mask-a :type symbol)
  (mask-id-a :type string))
  (flow
    (:doc "Multi-exposure for Au-Cr mask patterning")
    (:version
      (:modified :number 1.0 :by "Duane Boning" :date "February 28, 1989"
        :what "Write operation in flow language"))
    (:advice (:opset "trl-mexp-ph" :name "MUTLI-EXPOSE-MASK"))

```

```

(:time-required (:hours 1 :minutes 40))
(:body
  (gen-trl-photo10a :mask-a mask-a
    :mask-id-a mask-id-a
    :prime? :t
    :coat? :t
    :prebake? :t
    :expose? :t
    :develop? :t
    :inspect1? :f
    :postbake? :t
    :inspect? :t
    :opset "trl-mexp-ph"
    :name "MULTI-EXPOSE-MASK"
    :time-required-sec 6000))))

```

B.1.17 trl-photo.fl

```

(define (trl-photo (mask-a      :type symbol)
  (mask-id-a      :type string :default "mask-id-a")
  (mask-b         :type symbol)
  (mask-id-b      :type string :default "mask-id-b")))

(flow
  (:doc "Standard KS2 photo-step with spin-on of STD resist")
  (:version
    (:modified :number 1.0 :by "Duane Boning" :date "February 28, 1989"
      :what "Write operation in flow language")))
  (:advice (:opset "trl-photo" :name "PHOTO-STEP-TRL"))
  (:time-required (:hours 1 :minutes 40))
  (:body
    (gen-trl-photo :mask-a mask-a
      :mask-id-a mask-id-a
      :mask-b mask-b
      :mask-id-b mask-id-b
      :prime? :t

```

```
:coat? :t
:prebake? :t
:expose? :t
:develop? :t
:inspect1? :f
      :postbake? :t
      :inspect? :t
:opset "trl-photo"
:name "PHOTO-STEP-TRL"
:time-required-sec 6000))))
```

B.1.18 trl-piranha.fl

```
(define (trl-piranha)
  (flow
    (:doc "Piranha clean of wafers.")
    (:version
      (:modified :number 1.0 :by "Duane Boning" :date "February 28, 1989"
        :what "Write operation in flow language"))
      (:advice (:opset "trl-piranha" :name "PYREX-CLEAN-OP"))
      (:time-required (:hours 1 :minutes 45))
      (:body
        (tpiranha))))
```

Bibliography

- [1] J. H. Boyden A. P. Neukermans and G. A. Garrettson. Capacitive mask aligner. United States Patent 4,654,581, March 1987.
- [2] T. Arai and Ichijo B. Moisture in material. *IEEE Transactions on Instrumentation and Measurement*, 26:148–152, 1977.
- [3] J. Bae. Modeling, control, and experimentation of a scanning tunneling microscope. Master's thesis, Massachusetts Institute of Technology, May 1994.
- [4] A. Burstein and W. J. Kaiser. The microelectromechanical gyroscope - analysis and simulation using spice electronic simulator. In *Technical Digest*, Micromachined Devices and Components, pages 225–232, Austin, TX, October 1995. The International Society for Optical Engineering.
- [5] Henry O. Choi. A lineary ultrasonic motor for nano-technology. Master's thesis, Massachusetts Institute of Technology, May 1996.
- [6] A. Taroni D. Marioli, E. Sardini. Measurement of small capacitance variations. *IEEE Transactions on Instrumentation and Measurement*, 40(2):426–428, April 1991.
- [7] A. Taroni D. Marioli, E. Sardini. High-accuracy measurement techniques for capacitance transducers. *Measurement Science Technology*, 4:337–343, 1993.
- [8] *Guide to the Process Flow Representation, Version 3.1.*
- [9] E. O. Doebelin. *Measurement Systems Application and Design*. New York: McGraw-Hill, 1983.

- [10] *KIC: A Graphics Editor for Integrated Circuit Design*.
- [11] S. K. Ghanshi. *VLSI Fabrication Principles*, chapter 8. John Wiley and Sons, Inc., 1994.
- [12] R. Gregorian and G. Temes. *Analog MOS Integrated Circuits For Signal Processing*, chapter 5. John Wiley and Sons, 1986.
- [13] K. Watanabe H. Matsumoto, H. Shimizu. A switched-capacitor charge-balancing analog-to-digital converter and its application to capacitance measurement. *IEEE Transactions on Instrumentation and Measurement*, 36(4):873–878, December 1987.
- [14] W. C. Heerens and G. H. Peerbolte. Capacitive gauge. United States Patent 4,347,478, August 1982.
- [15] W. Chr. Heerens. The solution of laplace’s equation in cylindrical and toroidal configurations with rectangular sectional shapes and rotation-symmetrical boundary condtions. *Journal of Applied Physics*, 47(8):3740–3744, August 1976.
- [16] W. Chr. Heerens. Basic principles in designing highly reliable multi-terminal capcitor sensors and performance of some laboratory test models. *Sensors and Actuators*, 3:137–148, 1983.
- [17] W. Chr. Heerens. Application of capacitance techniques in sensor design. *Journal of Physics E: Scientific Instruments*, 19:897–906, 1986.
- [18] S. M. Huang. *Capacitance Transducers for Concentration Measurement in Multi-Component Flow Processes*. PhD thesis, Manchester University, 1986.
- [19] A. L. Hugill. Displacement transducers based on reactive sensors in transformer ratio bridge circuits. *Instrument Science and Technology*, pages 597–606, 1982.
- [20] R. V. Jones and J. C. S. Richards. The design and some applications of sensitive capacitance micrometers. *Journal of Physics E: Scientific Instruments*, 6:589–600, 1973.

- [21] J.M. Jongeling and W. Chr. Heerens. The comparison of two absolute layer thickness gauges. *Journal of Physics E: Scientific Instruments*, 17:664–668, 1984.
- [22] T. Juneau and A. P. Pisano. Micromachined dual input axis angular rate sensor. In *Technical Digest, Solid-State Sensor and Actuator Workshop*, pages 299–302, Hilton Head, SC, June 1996. Transducers Research Foundation.
- [23] E. Kreyszig. *Advanced Engineering Mathematics*, chapter 20.4. John Wiley and Sons, 1988.
- [24] J. T. Kung and H. Lee. An integrated air-gap-capacitor pressure sensor and digital readout with sub-100 attofarad resolution. *Journal of Microelectromechanical Systems*, 1(3):121–128, 1992.
- [25] David G. Leip. Design and implementation of a capacitive measurement circuit with application to integrated micromotor position sensing. Master’s thesis, Massachusetts Institute of Technology, February 1994.
- [26] J. C. Maxwell. *A Treatise on Electricity and Magnetism*. Oxford: Clarendon, 1873.
- [27] G. L. Miller. Capacitive incremental position measurement and motion control. United States Patent 4,893,071, January 1990.
- [28] V. T. Morgan and D. E. Brown. A differential-capacitance transducer for measuring small displacements. Technical report, The Institute of Physics, 1969.
- [29] R. Morrison. *Grounding and Shielding Techniques in Instrumentation*. Wiley-Interscience, 1986.
- [30] H. Philipp. The charge transfer sensor. *Sensors*, 13(11):36–41, November 1996.
- [31] F. Rudolf. A micromechanical capacitive accelerometer with a two-point inertial-mass suspension. *Sensors and Actuators*, 4:191–198, 1983.

- [32] R. G. Green S. M. Huang, A. L. Stott and M. S. Beck. Electronic transducers for industrial measurement of low value capacitances. *Journal of Physics E: Scientific Instruments*, 21:242–252, 1988.
- [33] L. C. Shen and J. A. Kong. *Applied Electromagnetism*. PWS Publishers, 1987.
- [34] F. D. Stacey. Displacement and tilt transducers of 140 db range. Technical report, The Institute of Physics, 1969.
- [35] R. T. Howe W. A. Clark and R. Horowitz. Surface micromachined z-axis vibratory rate gyroscope. In *Technical Digest, Solid-State Sensor and Actuator Workshop*, pages 283–287, Hilton Head, SC, June 1996. Transducers Research Foundation.
- [36] H. Walcher. *Position Sensing: Angle and Distance Measurement for Engineers*, chapter 3.12. Butterworth Heinemann, 1994.
- [37] S. Wolf and R. N. Tauber. *Silicon Processing for the VLSI Era: Volume 1-Process Technology*, chapter 12-13. Lattice Press, 1986.